# A study of Kaon-Deuteron interactions at low energy.

by David Pearce.

A thesis submitted for the degree of Doctor of Philosophy of the University of London.

Department of Physics.
Imperial College,
London S.W. 7.

March 1970.

Abstract

The Saclay 82 cm bubble chamber filled with deuterium, was exposed to a beam of $K^-$ particles having momenta of 1.45 and 1.65 GeV/c, and 670,000 pictures were taken. $K^-$ neutron collisions were studied, and because of the Fermi motion of the target neutron, a wide centre of mass energy range was covered, of about 1850 to 2150 MeV.

The event processing chain is described, and problems concerned with the impulse approximation are discussed. These problems include the correct selection of the "spectator particle", the reliability of kinematic fitting methods used when a "spectator" proton is unseen, the extent of validity of the impulse approximation, and the assignment of events resulting from multiple collisions.

Cross-sections are calculated for all fittable final states, produced from $K^-$ neutron interactions, except for $K^-n$ and $\Xi K(n\pi)$.

The results are consistent with charge independence, and with accepted values of branching ratios.

The variation of cross-section with centre of mass energy, in the range 1850 to 2150 MeV is presented for the $\Sigma\pi$ channel, five three-body channels, and six quasi two-body channels. The results are in good agreement with all available data from other experiments. Evidence is found for decay of the $\Sigma(2030)$ to $\Lambda\rho$ and $\Sigma(1385)\pi$, and for a $\Sigma(2080)$ resonance decaying to $N^*(1236)\,\overline{K}$, $\Lambda(1405)\pi$ and $\Lambda(1520)\pi$. Evidence is found also for the decay of the $F_{5/2}$ $\Sigma(1905)$ to $K^*(890)N$, $\Lambda(1520)\pi$ and $\Sigma(1385)\pi$, although a more likely explanation of these effects is the decay of a $P_{3/2}$ $\Sigma(1950)$ resonance.

D. Pearce. PhD Thesis University of London, 1970.

ERRATA

| Page | | |
|---|---|---|
| 4 | Contents: | For "Contents ..... 3" read "..... 4".<br>For "List of tables ..... 7" read ".... 8".<br>For "Introduction .....8" read ".....9". |
| 9 | Introduction: | 6 lines from bottom; insert ref. nos. 74 and 80, after "(1850-2150 MeV)". |
| 12 | Table 1.2: | Line 5; for "+" read "$\pm$". Line 13; for "secs" read "$\mu$secs". |
| 67 | 4.2: | Insert "p" on r.h.s. of equations 4.5, 4.6 and 4.7. |
| 105 | 6.1.2: | 4 lines from bottom; for ref. 85 read ref. 69, and for ref. 84 read ref. 68. |
| 120 | 6.2.7: | Last line; for "1.45 GeV/c" read "1.65 GeV/c". |
| 136 | Table 6.5: | $\Sigma(1385)\pi$, calc. ratio at 1.45 GeV/c; for "$0.85^{+}$ .04" read "$0.85^{+}$ .08". |
| 137 | 6.8: | Second line; insert "$\pi$" after "$\Lambda(1520)$" and after "$\Lambda(1405)$". |
| 147 | 7.2.1: | Second paragraph; for "$F_{5/2}$ (1905)" read "$F_{5/2}\Sigma(1905)$". |
| 161 | 7.3.3: | 4 lines from bottom; delete "K*(890)n". |

Contents


| | | Page |
|---|---|---|
| Abstract. | | 2 |
| Contents. | | 3 |
| List of tables. | | 7 |
| Introduction. | | 8 |
| CHAPTER 1 | The Beam-line and Bubble Chamber. | 11 |
| 1.1. | The Beam-line | 11 |
| 1.1.1. | Description. | 11 |
| 1.1.2. | Tuning the Beam-line. | 13 |
| 1.1.3. | $\pi^-$ contamination of the second run at 1.65 GeV/c. | 14 |
| 1.2 | The Bubble Chamber. | 14 |
| Figures 1.1 - 1.4. | | 16-19 |
| CHAPTER 2 | Scanning and Measuring. | 20 |
| 2.1. | General notes. | 20 |
| 2.2. | Scanning. | 20 |
| 2.2.1. | Organisation | 20 |
| 2.2.2. | Selection of required event types. | 21 |
| 2.2.3. | Other Criteria | 22 |
| 2.3. | Measuring the collisions | 24 |
| 2.4. | The book-keeping system. | 24 |
| Figures 2.1 - 2.3 | | 27-28 |
| CHAPTER 3 | Computer processing of events. | 29 |
| 3.1. | Introduction | 29 |
| 3.2 | Paper tape conversion and event checking | 29 |
| 3.3 | The Geometry program | 30 |
| 3.3.1. | General description. | 30 |
| 3.3.2. | Special features. | 31 |
| 3.3.3. | Criteria for remeasurement or rejection of events. | 32 |
| 3.3.4. | Lens distortion corrections | 32 |
| 3.3.5. | Magnetic field calculations | 34 |
| 3.3.6. | Choice of error constants | 35 |
| 3.3.7. | Beam track parameters | 37 |

CHAPTER 3 (Continued) Page

3.4. The Kinematic fitting program. . . . . 37

3.4.1. General description . . . . . 37

3.4.2. $P_x, P_y, P_z$ fitting . . . . . 38

3.4.3. Selection criteria. . . . . 39

3.4.4. Checks on results . . . . . 40

3.5. Preparation of Data Summary Tape. . . . 42

3.6. The Statistics program . . . . . 45

3.6.1. General description . . . . . 45

3.6.2. Special facilities for deuterium collisions . . . . . 47

Figures 3.1 - 3.11 . . . . . 48-58

CHAPTER 4 Selection of events satisfying the impulse approximation. 59

4.1. Introduction . . . . . 59

4.2. Choice of spectator particle . . . . . 60

4.3. Choice of maximum spectator momentum to ensure agreement with the impulse approximation . . . . . 62

4.4. Agreement with the impulse approximation for events with proton spectator slower than 280 MeV/C. . . . . 64

4.5. Reliability of $P_x, P_y, P_z$ fits. . . . . 67

Figures 4.1. - 4.7 . . . . . 71-80

CHAPTER 5 Contamination and decay weighting . . . 81

5.1. Estimation of the fraction of $\pi^-$ particles in the beam . . . . . 81

5.2. Contamination of all three-body channels. 82

5.2.1. Introduction . . . . . 82

5.2.2. Quantities plotted . . . . . 83

5.2.3. $K\bar{n} \rightarrow \Lambda\pi^- \pi^o$ . . . . . 84

5.2.4. $K\bar{n} \rightarrow n\bar{K}^o\pi^-$ . . . . . 87

5.2.5. $K\bar{n} \rightarrow pK^-\pi^-$ . . . . . 88

5.2.6. $K\bar{n} \rightarrow \Sigma^{\mp}\pi^{\pm}\pi^-$ . . . . . 89

5.3. Weighting for unseen weak decays . . . . 90

CHAPTER 5 (Continued) Page

5.3.1. Introduction . . . . . 90

5.3.2. Small angle decay losses for $\Sigma^{\mp}$ decays. 92

Figures 5.1. - 5.11 . . . . . 94-103

CHAPTER 6 Calculation of cross-sections for all channels . . . . . 104

6.1. Introduction. . . . . 104

6.1.1. Calculation method . . . . . 104

6.1.2. Explanation of cross-section tables. 105

6.2. Correction factors . . . . . 115

6.2.1. Introduction . . . . . 115

6.2.2. Ambiguous fits . . . . . 115

6.2.3. Unseen decay modes, and decay losses 117

6.2.4. Scanning losses . . . . . 117

6.2.5. Processing losses . . . . . 118

6.2.6. Contamination . . . . . 120

6.2.7. Fit probability . . . . . 120

6.2.8. Unseen spectators. . . . . 122

6.3. The Glauber correction . . . . . 123

6.4. Assignment of fast spectator events . . . 125

6.5. Error calculations . . . . . 128

6.6. Checks on reliability of the results . . 129

6.7. Cross-sections for three-body reactions using all available collaboration data . 131

6.8. Cross-sections for resonance production in three -body reactions. . . . . 131

Figures 6.1. - 6.3. . . . . 138-143

CHAPTER 7 Variation of cross-section with centre of mass energy. . . . . 144

7.1. Calculation method. . . . . 144

7.2. Results for the $\Sigma\pi$ channel, and for three-body and quasi two-body channels. . . . . 147

7.2.1. Introduction . . . . . 147

7.2.2. $\Sigma\ \pi$ 148

CHAPTER 7 (Continued) Page

7.2.3. $nK^{o}\pi^{-}$ . . . . . 150

7.2.4. $K^{*}(890)^{-}$ n . . . . . 150

7.2.5. $N^{*}(1236)$ $\bar{K}$ . . . . . 150

7.2.6. $pK^{-}\pi^{-}$ . . . . . 151

7.2.7. $\Lambda\pi^{-}\pi^{o}$ . . . . . 152

7.2.8. $\Sigma(1385)\pi$ . . . . . 153

7.2.9. $\Lambda\rho^{-}$ . . . . . 153

7.2.10. $\Sigma^{-}\pi^{+}\pi^{-}$ . . . . . 155

7.2.11. $\Sigma^{+}\pi^{-}\pi^{-}$ . . . . . 155

7.2.12. $\Lambda(1405)\pi^{-}$ . . . . . 157

7.2.13. $\Lambda(1520)\pi^{-}$ . . . . . 157

7.3. Possible $\Sigma$ resonances produced in the s channel. . . . . 159

7.3.1. Introductions. . . . . 159

7.3.2. $\Sigma(1905)$. . . . . 159

7.3.3. $\Sigma(2030)$ . . . . . 161

7.3.4. Other possible resonances. . . . . 162

7.4. Conclusions. . . . . 163

Figures 7.1. - 7.12. . . . . 164-174

References . . . . . 175

Acknowledgements . . . . . 180

List of Tables.


| Table | Page |
|---|---|
| 1.1 | 10 |
| 1.2 | 12 |
| 1.3 | 15 |
| 2.1 | 23 |
| 3.1 | 36 |
| 3.2 | 41 |
| 3.3 | 43 |
| 4.1 | 64 |
| 5.1 | 82 |
| 5.2 | 85 |
| 5.3 | 87 |
| 5.4 | 87 |
| 5.5 | 89 |
| 5.6 | 91 |
| 5.7 | 92 |
| 5.8 | 92 |
| 5.9 | 93 |
| 6.1 | 106-109 |
| 6.2 | 110-113 |
| 6.3 | 116 |
| 6.4 | 119 |
| 6.5 | 121 |
| 6.6 | 121 |
| 6.7 | 123 |
| 6.8 | 124 |
| 6.9 | 127 |
| 6.10 | 128 |
| 6.11 | 130 |
| 6.12 | 131 |
| 6.13 | 132 |
| 6.14 | 134 |
| 6.15 | 136 |
| 7.1 | 149 |
| 7.2 | 160 |

Introduction

The author joined the Imperial College bubble Chamber group in October 1964, and after eight months of course-work, passed a PhD qualifying examination. His first work was concerned with $K\bar{p}$ interactions in a bubble chamber at 10 GeV/c momentum; this involved mainly scanning and data-processing.

The principal work, on which this thesis is based, was started in February 1966. This was a large scale, low energy $K^-d$ bubble chamber experiment, carried out at the Rutherford Laboratory by a collaboration of groups from the Imperial College and the Universities of Birmingham, Edinburgh and Glasgow. Photographs were taken using the Saclay 82cm bubble chamber filled with deuterium, at momenta of 1.45 and 1.65 GeV/c (see table1.1). The experiment was planned to investigate the formation of $\Sigma(2030)$ and other $\Sigma$ resonances, in the direct channel.

The author helped in all picture-taking runs, and in the scanning and processing of all the 1.65 and part of the 1.45 GeV/c data. He had particular responsibility for maintaining the Rutherford Laboratory geometry program, and for several aspects of the analysis of the collected events , including the use of the impulse approximations to isolate $K^-$ neutron collisions. The author was responsible for nearly all of the analysis of three-body channels at Imperial College, and for nearly all of the cross-section results presented in this thesis.

There have been only two previous $K^-n$ experiments in the energy region covered by this experiment (1850 - 2150 MeV), and therefore the extensive cross-section data presented here constitutes a considerable advance in knowledge. This data provides good evidence for previously unreported decay modes of several s-channel $\Sigma$ resonances to quasi two-body final states. Some aspects of the discussion concerning the use of the impulse

approximations should also contribute to deeper understanding of this subject.

Table 1.1 Details of runs

| Run | Dates | Momentum (GeV/c). | No. of pictures | Average No. of K's/ pictures |
|---|---|---|---|---|
| 1 | 18th-24th March 1966 | 1.65 | 111,000 | 6 |
| 2 | 7th-14th April 1966 | 1.65 | 117,000 | 10 |
| 3 | 4th-20th March 1967 | 1.45 | 247,000 | 14 |
| 4 | 25th March-5th April 1967 | 1.65 | 200,000 | 14 |

247,000 pictures, 3.5 million $K^-$ particles at 1.45 GeV/c.

428,000 pictures, 4.7 million $K^-$ particles at 1.65 GeV/c.

# CHAPTER 1 The Beam-line and Bubble Chamber.

## 1.1 The Beam-line.

### 1.1.1 Description.

The K1 beam-line provided beams of $K^+$, $\pi^+$, $K^-$ and $\pi^-$ particles from 1.32 to 2.2 GeV/c momentum for the Saclay bubble chamber installed at the Rutherford Laboratory. It was operational from December 1964 to May 1967, and was designed by Dr. A. Seagar and others; unfortunately, no detailed description has been published, apart from a short description in a thesis[1].

The important beam parameters are given in table 1.2, and the layout, in figure 1.1. The beam-line comprised two similar stages; each stage defined momentum by a bending magnet acting in the horizontal plane, and a vertical collimator (CH). The $K^-$ particles were accepted, and $\pi^-$ particles rejected in each stage by an electrostatic separator with horizontal plates, and a horizontal collimator (CV). After the second mass collimator, CV3, a short section defocussed the beam and steered it into the bubble chamber.

The copper target was situated in Octant 4 of Nimrod, the 7 GeV/c proton synchroton; it was flipped up on the inside of the beam which was then steered onto it using the radio frequency accelerating cavity[2]. Negative particles from the collisions of the circulating proton beam emerge from Straight 5 at $20^\circ$ to the circulating beam. Collimator CV1 defined the vertical acceptance, and QO defined horizontal acceptance. Doublets of quadrupole magnets (Q) focussed the beam at the collimators, and ensured a parallel beam through the separators. These had horizontal stainless steel electrodes, in 10 foot sections, 10 cms apart, and were tilted to follow the beam trajectory. Pairs of bending magnets (VM)

Table 1.2 Important parameters of the K1 beam-line for this experiment.

The target was a metal bar 2.5 mm wide and 10 mm high; for runs 1 and 2 it was 150 mm long and made of beryllium, and for runs 3 and 4 it was 100 mm long, made from copper.

Number of protons incident on target = about 5 x 10" per pulse.

Initial angular acceptance = + 6 mrad. vertically, + 12.5 mrad. horizontally.

Length of beam-line = 55 metres.

Electrostatic separator fields = 40 KV/cm.

Momentum bite = 1%.

Momentum spread at chamber = about 1½%, because of straggling in counters and in the bubble chamber "window".

Number of $K^-$ particles reaching chamber = 6-15 per pulse.

Length of $K^-$ pulse = 500 secs.

Contamination by $\pi^-$ particles = about 12% for run 2

= about 1 - 2% for runs 1, 3, and 4.

corrected the bending effect of the separators. The purpose of the second stage was to eliminate $\pi^-$ and $\mu^-$ particles produced by $K^-$ decays and collisions with the collimator jaws, and to redefine the momentum. The mass collimators CV2 and CV3 were skewed in the horizontal plane, and specially shaped, to reduce chromatic aberration. (S.M. was a shutter magnet not used for our run).

The beam performance was monitored by a counter near the target, and four scintillation counters (S2,S3,S5,S6) in the beam. The bubble chamber flash tubes were not fired if less than four particles reached the chamber in a single pulse.

1.1.2 Tuning the beam-line.

The procedure used varied greatly, as steps often had to be repeated when errors were found. The outline was as follows:

i) Nominal values for bending magnet and quadrupole currents and separator voltages, had been calculated using the beam-handling program Tramp[3]. The collimator settings were decided from the calculated beam profile. All separators and magnets were switched on and set to the nominal values.

ii) CV1 was closed to prevent saturation of the counters, and both pairs of VM magnets were tuned to transmit $\pi^-$ particles.

iii) The second stage bending magnet (M3) was tuned for maximum transmission. For some runs when Nimrod operating conditions were different from those used in Tramp, the second stage was left at the nominal values, and the first stage magnets (M1 or M2) were tuned instead.

iv) CV1 was re-opened; all counter delays were set for $K^-$ particles, and all VM magnets were retuned for $K^-$'s. Figure 1.2 shows a typical tuning curve, from which the $\pi^-$ and $\mu^-$ contamination can be estimated to be 20%.

v) Finally the particle tracks in the chamber were observed, and Q9 and VM5 were altered to produce a good beam spread, and optimum beam height in the chamber.

### 1.1.3 $\pi^-$ contamination of the second run at 1.65 GeV/c.

The beam purity was proportional to the ratio of S2,S5,S6 coincidences to S5,S6 coincidences, and it was noticed to be low after about 30 rolls of this run. It was found that the CV1 position scales had incorrect zeroes, and that moving the lower jaw of CV1 upwards increased the indicated purity. Probably the beam had been hitting the lower plate of separator 1, and some of the resulting off-momentum $\pi^-$ particles had been reaching the chamber. However, later studies of delta rays and collisions from incident $\pi^-$'s (section 5.2) showed that the contamination stayed high until 15 rolls later, when the beam had been steered with VM3 and VM4. Possibly the beam had been hitting the plates of the second separator; the exact reasons were never found out. But this was the only run with high contamination, and the contamination averaged over all runs was low.

## 1.2 The Bubble Chamber.

The Saclay 82 cm bubble chamber was built in 1960 as a circular 50 cm chamber[4], and converted to its present form in 1964. No detailed description of the converted chamber is available. Its operating parameters are given in table 1.3. A piston expansion system was used, and a novel feature was the use of two hydrogen or deuterium heat-exchangers to cool down and then to stabilize the chamber; these were hollow containers which could be filled with the liquefied gas to increase their conductivity. Figure 1.3 shows the construction of the chamber.

When filled with hydrogen, the chamber was expanded twice during each Nimrod pulse, but this was not attempted for deuterium runs because of the higher operating pressures needed.

Table 1.3 Operating conditions of the Saclay 82 cm bubble chamber, when filled with deuterium.

Pressure = about 7 atmospheres.

Pressure drop = about 3 atmospheres.

Temperature = $32^{\circ}K$.

Magnetic field = 19.5 Kilogauss.

Total volume = 82 x 50 x 50 $cm^3$ = 210 litres.

Useful volume = 180 litres.

Flash delay = about 1 msec.

Bubble size at time of flashes = .3 mm.

Frequency of expansion = once per Nimrod pulse, i.e. every 2.2 seconds.

---

The optical system is shown in figure 1.4. The three cameras used separate rolls of 50 mm Ilford TC semi-perforated film. The demagnification for tracks in the centre of the chamber was 11.3, and a small lens stop, of f/8, ensured that the whole depth of the chamber was in focus. The arrangement of cameras gave stereo angles of $13^{\circ}$, typically.

Straight through, dark field illumination was used, with four flash tubes on the far side of the chamber and a screen of cylindrical lenses to condense the light. Two complete grids of fiducial crosses were engraved on the inside of each chamber glass to provide a reference system. A data box displayed the frame no. and experiment no. and was photographed to one side of the chamber image.

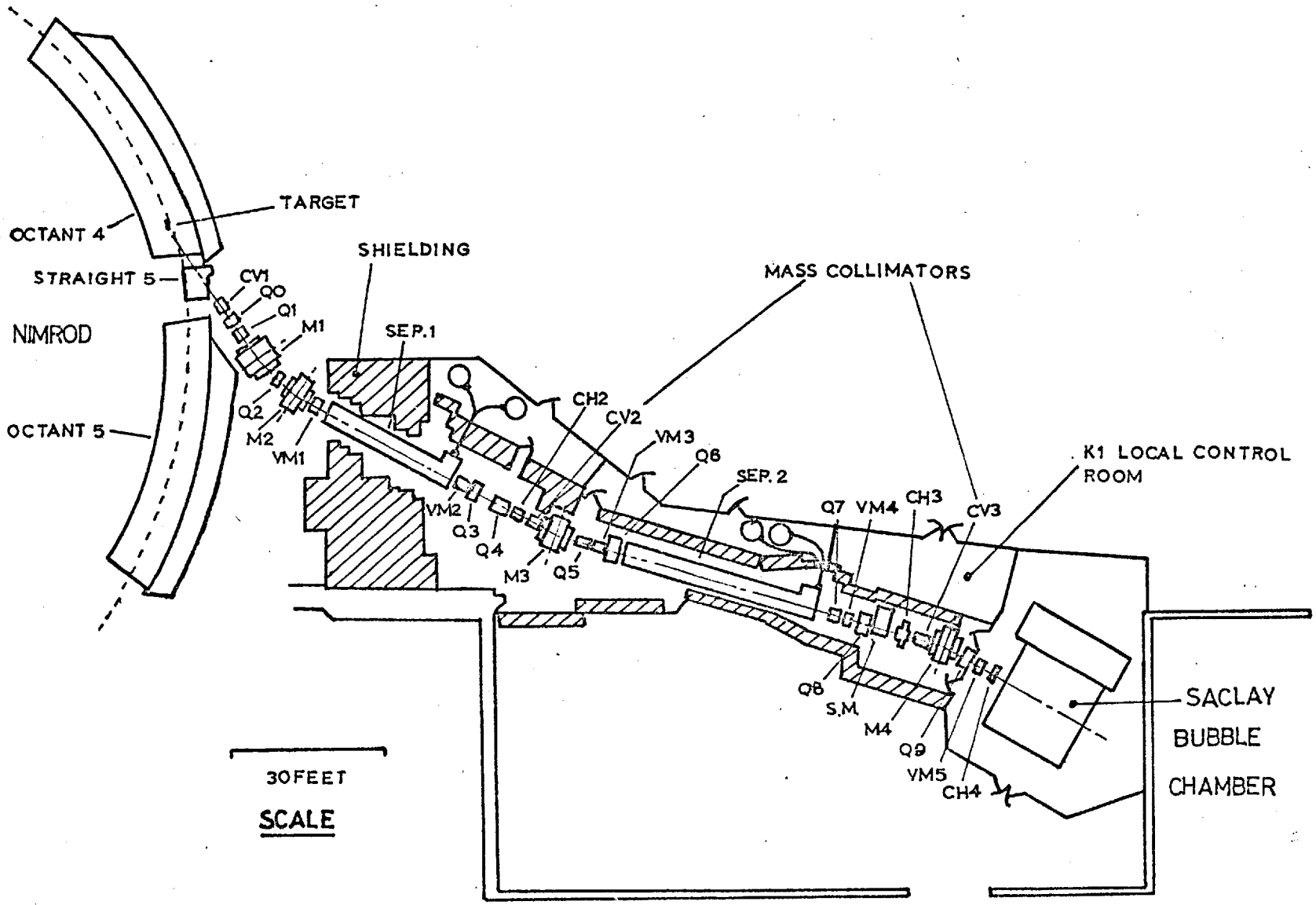


FIGURE 1.1 LAYOUT OF K1 BEAM-LINE.

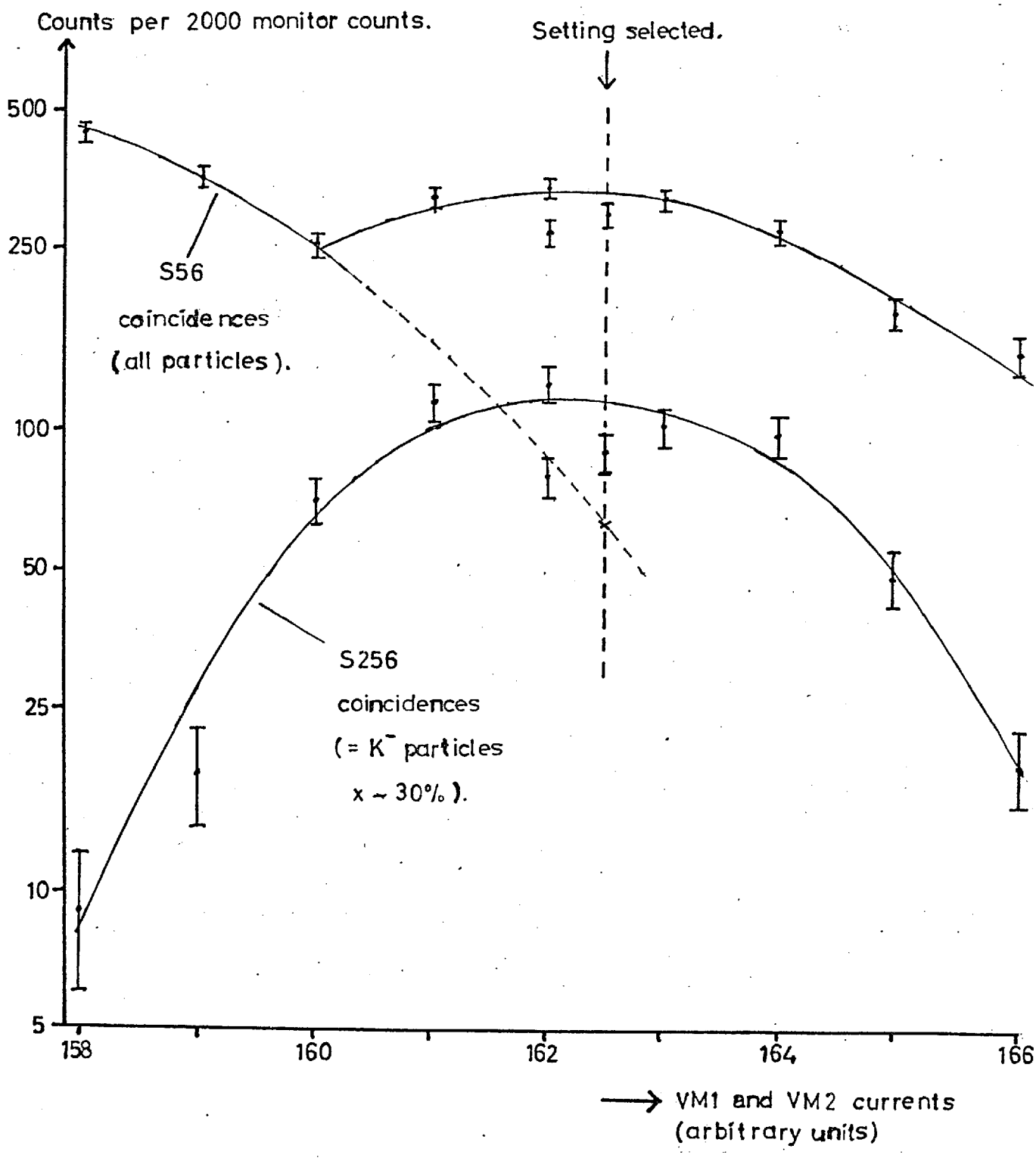


FIGURE 1.2 TUNING CURVES FOR 1.45 GEV/C RUN.

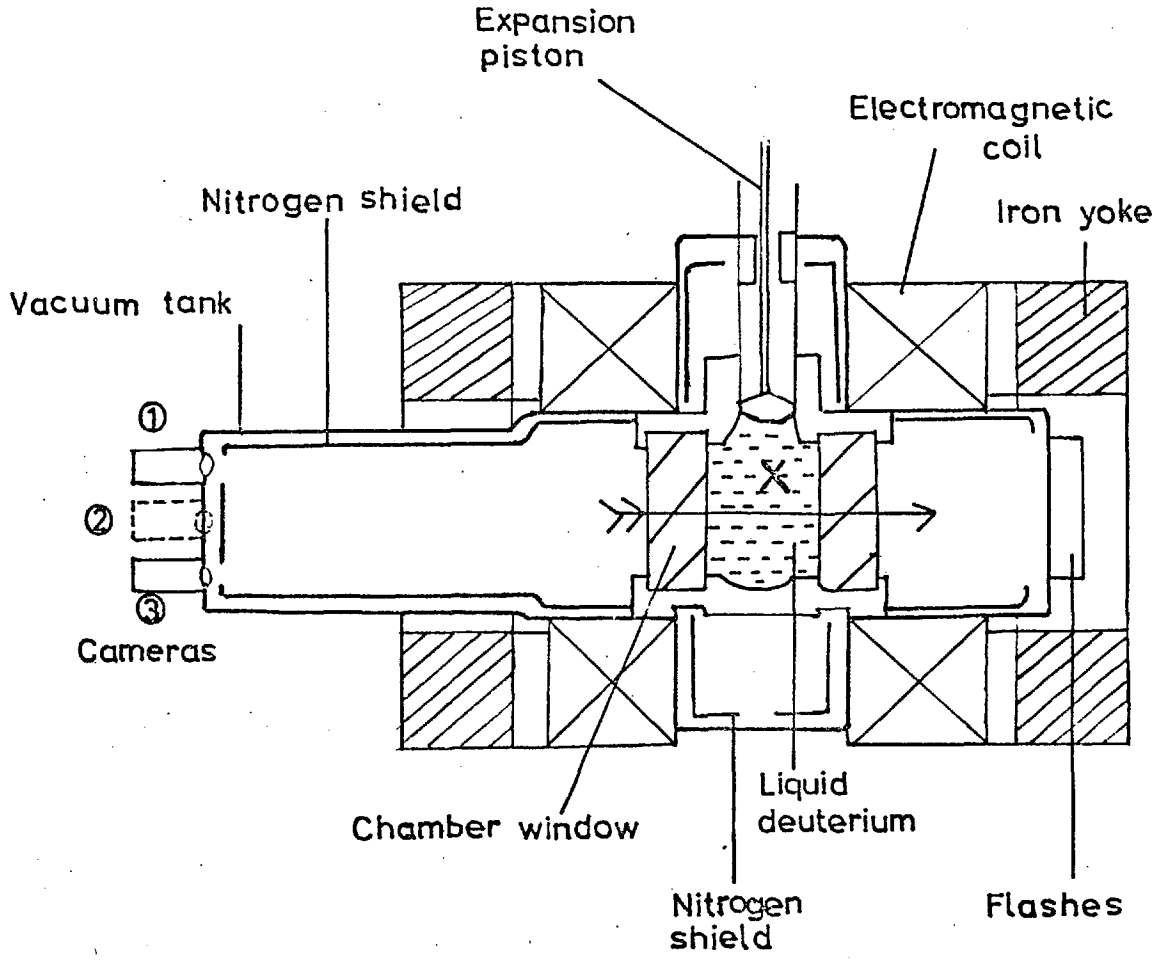


Arrow indicates direction of magnetic field.

X indicates beam entry position. Beam travels out of paper.

FIGURE 1.3 SECTIONAL VIEW OF BUBBLE CHAMBER.

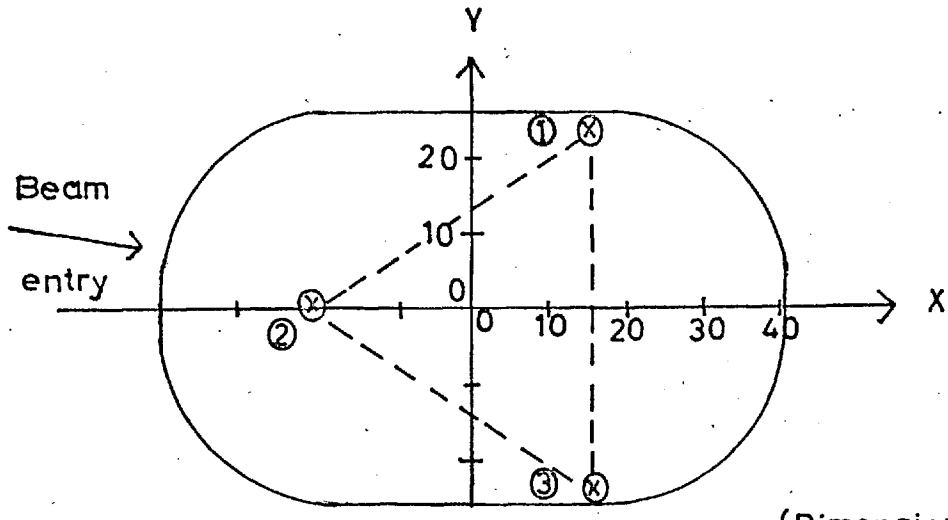


(Dimensions in cms)

A) Camera positions.

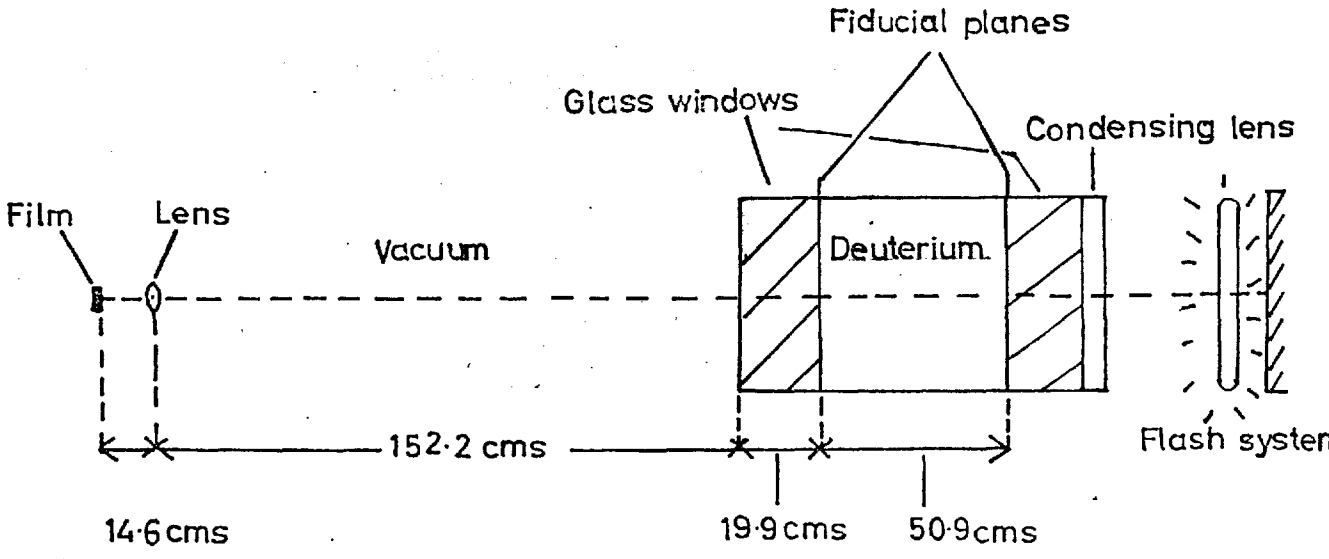


B) Optic axial distances.

FIGURE 1·4 BUBBLE CHAMBER OPTICAL SYSTEM.

# CHAPTER 2 Scanning and Measuring.

## 2.1 General notes.

The film obtained was divided equally between the four collaborating groups, and the scanning, measuring, and computer processing of selected collisions was done separately. All groups used basically similar event selection criteria, and used similar measuring machines, except that the Glasgow and Edinburgh groups used semi-automatic machines, which were slightly more accurate than the manual machines. The system described here is the one used at Imperial College.

## 2.2 Scanning.

### 2.2.1 Organization.

The scan-tables used carried three rolls of film, and projected an approximately full-size image of the chamber onto a horizontal table in front of the scanner.

For ninety per cent of the film, two independent scans and a check-scan were made, and events satisfying the criteria of section 2.2.2 were recorded. The check-scans compared and corrected the first two scans and provided data to enable scanning efficiencies to be calculated for all topologies and all scanners; they were usually carried out by physicists. For the remainder of the film, only one scan was made, by selected technical assistants; however, later, every fifth roll was re-scanned and check-scanned, in order to obtain scanning efficiencies. The average efficiency for a single scan was about 80%, and after the check-scan it was about 97%.

Each selected collision was recorded on a computer card. Figure 2.1 shows the front of a typical card. Coded information was written on

the right hand side of the card, and was later punched on the left hand side, so that cards could be read automatically and used for automated bookkeeping. On the back of the card the scanner drew a labelled sketch of the event, and any special measuring instructions, for example a T to indicate a tag needed for a stopping positive track. Also note was made of any electron pairs, Dalitz pairs or $\pi^+ \rightarrow \mu^+ \rightarrow e^+$ decays, to help with particle identification later.

The coded information indicated the following: a sign-on card was filled in by every scanner starting a new shift or a new roll, and gave the scanner's identification number, the scan number, experiment number and roll number; this was punched onto all cards for that shift. The frame number, event number, and zones are self-explanatory. The topology code is given in figure 2.2. The six comment digits gave estimated track ionisations, indicated the presence of alternative origins for neutral vees, and stated if the event was unmeasurable, because of a faint image or overlapping tracks. Unfortunately the ionisation estimates could not be relied on because of systematic under- or over-estimation by many scanners.

### 2.2.2 Selection of required event types.

The scanning criteria were designed to select fittable collisions between the incident $K^-$ particle and the neutron. The proton and neutron are fairly loosely bound in the deuterium nucleus, and for many collisions, only one nucleon is struck, while the other nucleon, referred to as the spectator particle, simply escapes with a momentum due to its Fermi motion, which is usually less than about 300 MeV/c (see chapter 4). Thus the criteria required a slow proton to be produced at the collision vertex, which could be a spectator to a $K^-$ - neutron collision. Two classes of

events were accepted at Imperial College:

A) Events with an odd number of tracks leaving the collision vertex ("odd-prongs"), except for one-prong events with no associated neutral vee, which could never give a constrained fit to any physical hypothesis.

By charge balance, a slow unseen positive particle must have been produced in such collisions; this could only be a proton or a deuteron, as $\pi^+$, $K^+$ or $\Sigma^+$ particles would decay after stopping. Later calculation showed that deuteron production was quite rare, except in elastic scattering, which is not relevant here. This category also included decays of the beam particles, $K^- \to \pi^+\pi^-\pi^-$, called "tau" decays.

B) Collisions with an even number of prongs, producing at least one positive, non-decaying track of more than four times minimum ionisation.

This selected protons slower than about 400 MeV/c, and also some slow $\pi^+$, $K^+$ or $\Sigma^+$ particles that happened to interact or leave the chamber without decaying. The latter were identified and the events including them were rejected when checking the kinematic fitting results.

About two-thirds of events selected were in category A. About one-third of all collisions were rejected because they fell in neither category, and there was therefore a considerable saving in measuring and computing time.

Other groups in the collaboration scanned and measured all fittable collisions, and it turned out that these results were needed for cross-section calculations.

### 2.2.3 Other Criteria.

Collisions had to have an incoming beam track of the correct curvature, and travelling within $15^\circ$ of the expected direction; a template was used to check these points. Also, for the first two runs, beam tracks

entering the chamber more than 16 cm above the centre of the chamber were rejected, as Dr. Miller had calculated that such tracks had passed through the thick metal chamber enclosure, and had, therefore, lost about 30 MeV/c momentum.

Collisions had to take place within a rectangular fiducial region defined on view two; this was to ensure accurate measurement, and to simplify cross-section calculations. No fiducial region was defined at this stage for decay vertices, but one was chosen later when obtaining histograms (see chapter 5).

Decays of charged secondary particles from a collision were only recorded if the (sagitta / chord length) in the projected view, up to the decay, was 0.02. This had the effect of rejecting nearly all $\pi^{\pm}$ and $K^{\pm}$ decays, but a negligible fraction of $\Sigma^{\pm}$ and $\Xi^{-}$ decays (see table 2.1). This criteria takes account of time dilation and is independent of the direction of the track. No tracks leaving secondary collisions were measured.

Neutral vee decays were accepted as associated if their estimated line of flight passed within one inch of the collision vertex, in the projected view on the scan table, or within half an inch of a negatively

---

Table 2.1 Effect of (sagitta / length) cut on charged particle decays.

| Particle | Maximum t/T in decay c.m. | Fraction decaying within this time (%) |
|---|---|---|
| $\pi^{\pm}$ | $4.92 \times 10^{-3}$ | 0.5 |
| $K^{\pm}$ | 0.0367 | 3.5 |
| $\Sigma^{+}$ | 13.6 | 99.99 |
| $\Sigma^{-}$ | 6.80 | 99.88 |
| $\Xi^{-}$ | 6.97 | 99.91 |

(T = average lifetime, from reference 24)

charged decay. A neutral vee could be included with more than one event, but a final choice was made using the results of the kinematic fitting.

Unmeasurable events were recorded, but were used only in cross-section calculations.

The identified slow proton in an even-prong event was always labelled as track 1, and the Geometry and Kinematics programs treated this track as a proton only, thus saving computing time.

## 2.3 Measuring the collisions.

Four measuring machines were used, two of the National type[5], and two built in the college workshops. The former had two image screens, the latter one, and the National machines were also slightly more accurate.

An optical system projected an image of the selected view onto the screen(s). A dot on the screen(s) defined the point of measurement, and the image could be moved relative to this. The movement was digitised by two Moiré fringe-systems, and the co-ordinates of the image could be punched out on paper tape.

The measurer was supplied with an ordered set of scan cards for one roll, and found an event on all three views. The event and measurement identification were set up on a switchboard, and punched out. For each view, four fiducial crosses and then the event tracks and vertices were measured and punched; about eight points were measured for each track. One back-glass and three front-glass fiducials were chosen, which were visible on all views.

## 2.4 The bookkeeping system.

The system used was improved and simplified through two years of use; the final version is described here.

The whole chain of event processing is summarized in figure 2.3. All scan cards were punched and listings of the cards were then obtained and kept for calculation of scanning efficiencies. Later this calculation was done by a computer program, which read the punched cards. After the check-scan the information punched on the corrected cards was stored on a magnetic tape, the directory tape; simple computer programs produced event lists and event totals from this, and also the tape was read by the Bind program, part of the function of which is to check the frame numbers and topologies specified by the measurers. After measuring and after checking the results of the Bind, Geometry, and Kinematics programs, the scan cards were sorted into four categories:

1) Events with good measurements, and unmeasurable events.

2) Events needing to be remeasured.

3) Events incorrectly scanned; these cards were corrected and put into category 1 or 2.

4) Events not including a proton with momentum less than 350 MeV/c; those were called "No Events" and were not used any further.

After checking the Kinematics program results, all cards in category 2 were returned to the measuring machines for remeasurement. Three measurement passes were done for all rolls, and a fourth pass was done for some rolls with a high failure rate. After this, the fraction of events that still did not have good measurements, or were unmeasurable ranged from 5 - 15% for all topologies, except a few rare topologies which were worse. This seemed good enough to avoid omission biases, especially as the unmeasurable events (about 5% of the total) were usually caused by overlapping beam tracks, flash failures, and other factors unconnected with any physical collision parameters.

Initially, processing results were filled in on the event lists,

but later, it was found that sufficient information was given by the physical separation of scan cards into categories, plus remeasuring instructions and other notes written on the cards. Data on the performance of scanners and measurers was obtained from the calculated scanning efficiencies, and from failure rates calculated by Bind and a post-Geometry program; this provided a useful feed-back.

The basic innovation of this system was the use of computer cards and of a directory tape; this provided a simple, trouble free, way of dealing with large numbers of events, and eliminated the hand compilation of event lists. However the updating of the directory tape did become tedious, and better systems could be devised.

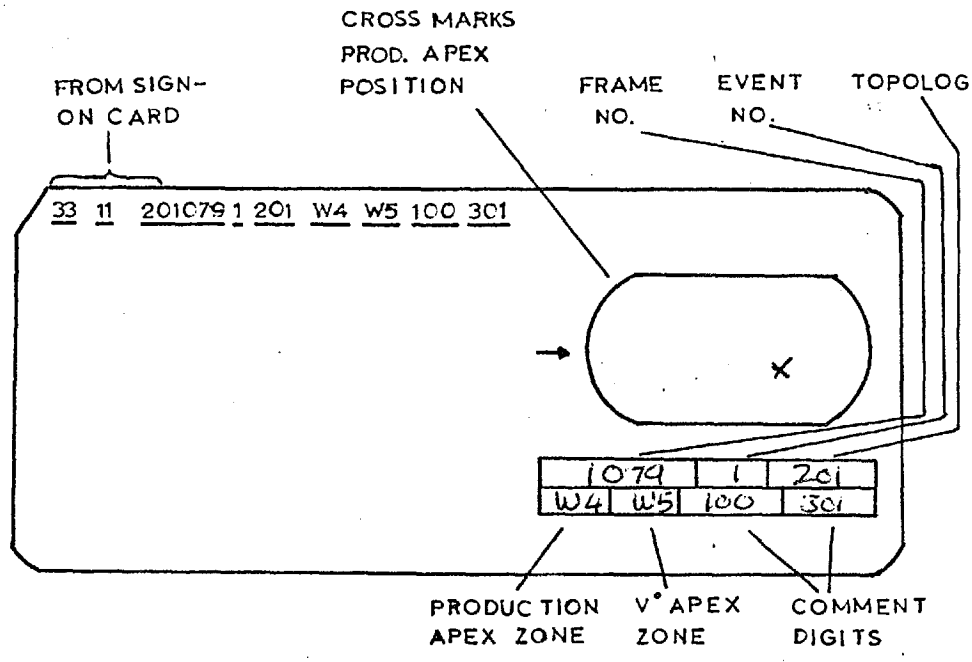


FIGURE 2.1 SCAN CARD INFORMATION

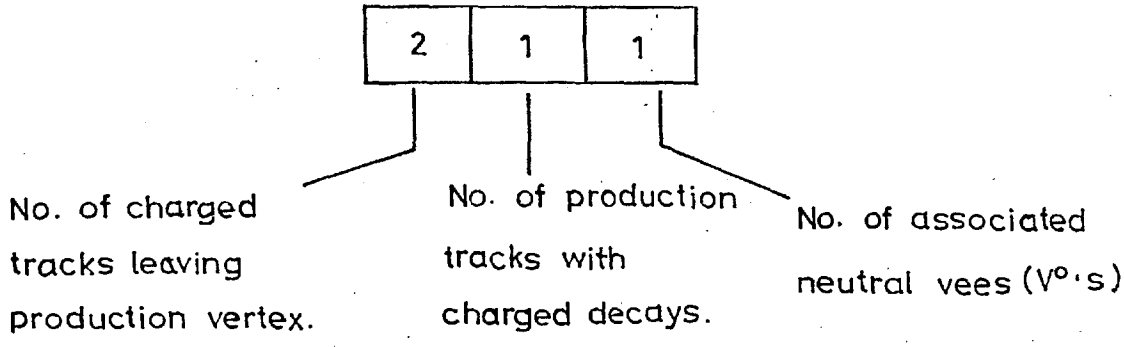


FIGURE 2.2 TOPOLOGY CODE

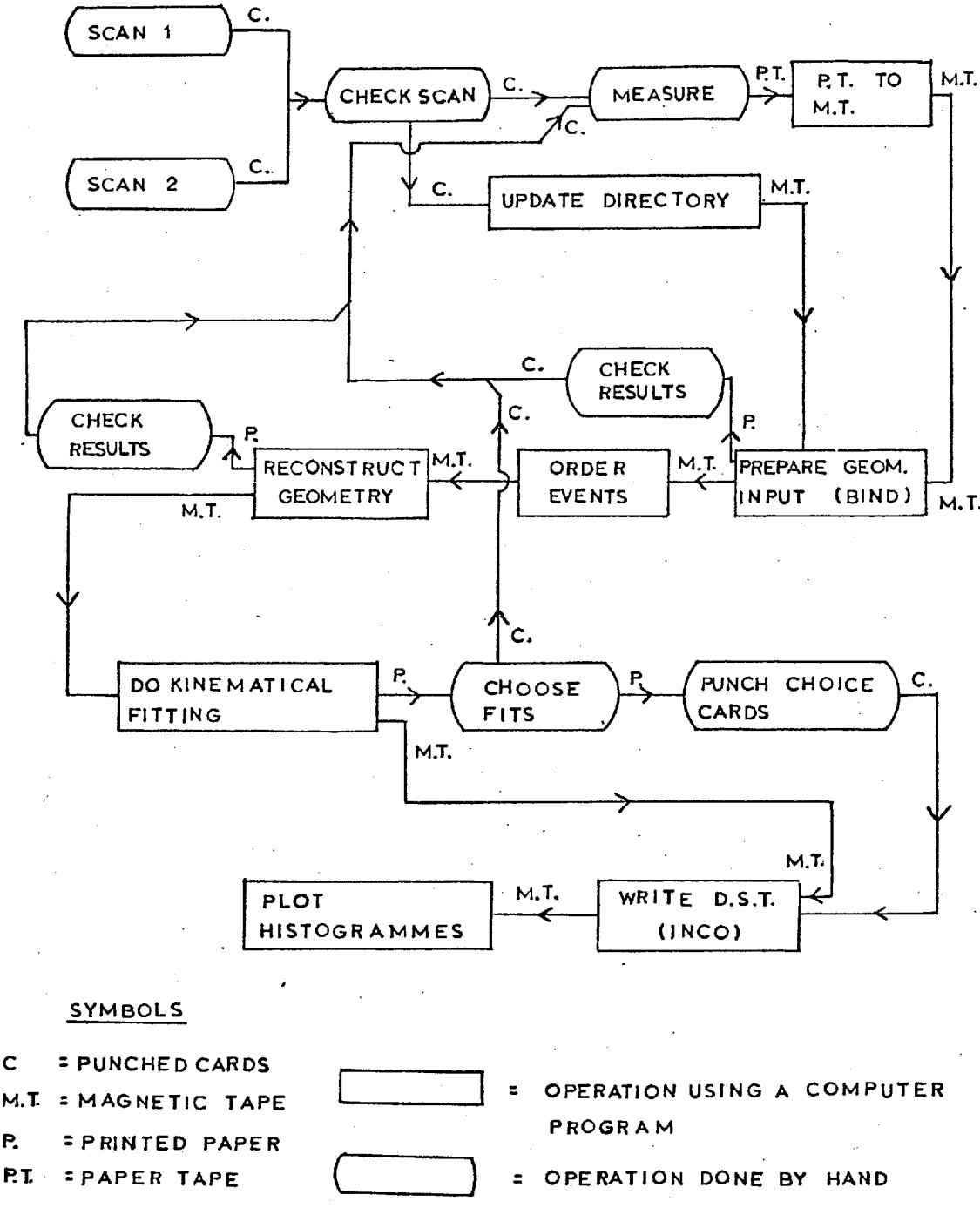


SYMBOLS

C = PUNCHED CARDS
M.T. = MAGNETIC TAPE
P. = PRINTED PAPER
P.T. = PAPER TAPE

= OPERATION USING A COMPUTER PROGRAM

= OPERATION DONE BY HAND

FIGURE 2.3 FLOW CHART FOR EVENT PROCESSING

# CHAPTER 3 Computer processing of events.

## 3.1 Introduction.

The system is summarized in figure 2.3. All the programs used were pre-existing, although many needed correction or modification for this experiment. The Imperial College group started using the Rutherford High Energy Laboratory (RHEL) system of programs[6], but changed to the CERN system[14),15),16)] after processing about one-third of the film. This change made the group's analysis compatible with other bubble chamber groups at Imperial College, and so saved program development time. Other collaborating groups used the RHEL programs throughout.

There were two main programs. The "Geometry" program reconstructed the tracks and vertices of a collision in three dimensions, from measurements made on the three photographs taken. The "Kinematics" program tested various hypotheses concerning the nature of the outgoing secondary particles, by requiring agreement with the relativistic energy-momentum conservation laws. Other programs prepared an input tape for the Geometry program, and merged and ordered the several types of output tapes.

The system used by the Imperial College group is described here; it is very similar to that used by the other $K^-d$ groups, except for a few differences that are pointed out.

## 3.2 Paper tape conversion and event checking.

The paper tape from the measuring machines was transferred to magnetic tape, using a small program running on an IBM 1401 computer.

The program Bind[7] read this magnetic tape, and, for all events passing various checks, wrote out records onto an output tape, in the format

required for input to the Geometry program (reference 8, appendix II). The frame and event number and topology of each event was checked against the directory tape (section 2.4). An event that failed any check, or could not be decoded, was written out onto a "failed event" output tape. Some of these events could be rescued by an editing program; but as the failure rate was usually only about 8%, it was simpler to remeasure them. A summary of measurers' failure rates was printed after each roll had been processed.

When using the CERN system, the event labelling system and the output format of Bind were considerably changed.

The RHEL system required events in strictly ascending frame number order, and the ordering was done by a program ECPS.

## 3.3 The Geometry program.

### 3.3.1 General description.

Consider the RHEL program first [8),9),10)].

Information for one event was read from the input tape and stored. Then the reconstruction of tracks was carried out in four stages. Firstly, the rays for each measured point were calculated, and any badly out-of-line points were rejected. Secondly, the depth was calculated for points measured on a selected "main view", using the rays for all views. Thirdly, the first space fit was carried out; a helix was fitted to the main view results. Lastly, the accurate helix fit used the results of the first space fit as starting values. For each measured track point, the program calculated a residual "d", the distance between the point and the nearest point on the assumed helix, after both points had been projected back onto the film reference plane. $\Sigma(d^2)$ was calculated for all track points on all views, and was minimized to obtain the best values of the helix parameters.

The track parameters were $(\text{momentum})^{-1}$, dip and azimuth angles;

the corresponding error matrix was calculated using either a standard film measurement error, or the r.m.s. residual, if it was larger than a certain limit. Each charged track slowed down because of Coulomb scattering, and this was taken account of in the fit. The momentum of any stopping track was calculated from a range-momentum table.

To reconstruct event vertices, points measured on tracks connected to a vertex were used, as well as vertex measurements, in order to obtain more accuracy (reference 9, section 3).

Finally the event bookkeeping information was written onto an output magnetic tape in one record, and the vertex and track reconstruction results were written out in a second record, in the format given in reference 9.

The Thresh geometry program needed different data and different tape formats, but operated in a similar way. However, it did not take account of the slowing down of tracks, did not use track measurements to improve vertex reconstruction, and did not consider all three components of magnetic field (see section 3.3.5). As a result, the track and vertex reconstruction errors were about 25% larger than those from the RHEL geometry program. This affected the effective mass resolution for these events, but was not a serious problem.

### 3.3.2 Special features.

For both versions of the program, the method of operation did not have to be changed for deuterium events; odd-prong as well as even-prong collisions could be processed.

Recent modifications to the RHEL geometry program are described in reference 10. Of these, the lens distortion corrections and the improved magnetic field calculations were used, and are discussed in the

following sections. The improved procedures for vertex reconstruction, for beam-track tests, and for stopping tracks were also used; but the other small improvements were not put in.

Even-prong events with fast spectator tracks were not required for the final analysis. Therefore, the RHEL geometry program was modified to print out, for these events, the minimum spectator momentum, p(min), that was compatible with the measured value; p(min) = (p-2.σ(p)). If this was larger than 350 MeV/c, the event was rejected.

### 3.3.3 Criteria for remeasurement or rejection of events.

Events were remeasured for track or vertex failure, or if a "tag" on a stopping track was not recognised, or if one view was completely missing. The reason for failure was noted on the scan card to help the measurers.

Two classes of events were rejected (both were called "No Events"). The first class comprised events without a slow proton, where the "proton" had previously been wrongly identified, or was too fast. The second class comprised events with fault number 8, that is, for which the beam track was outside certain limits on momentum, angles, and entry position. Later studies showed that about one-half of such events were produced by $\pi^-$ or off-beam $K^-$ particles. The rejection rate was about 20% for the first two runs, which meant a 10% rejection of good events; so for later runs, which suffered very little beam contamination, no tests were made on the beam tracks.

The other collaborating groups did not reject such events.

### 3.3.4 Lens distortion corrections.

These are described in reference 10, section 2.

It was found that if optical constants were obtained without

considering lens distortions, the fiducial crosses were reconstructed with a systematic error in z position. The flat fiducial planes were reconstructed as curved surfaces, bending towards the cameras by about 3 mm at each end of the chamber (figure 3.1). As a consequence of these distortions, tau decays were badly fitted; chi-squared values were generally too high, and the distribution of beam track dip "stretch functions" (see section 3.4.1, equation 3.4) and of the z-component of missing momentum were asymmetric (figure 3.2 a).

To correct for this, all points on the film reference plane were transformed according to the expression:[11]

$$\begin{bmatrix} x^1 \\ y^1 \end{bmatrix} = \begin{bmatrix} x \\ y \end{bmatrix} (1+a_1x+a_2y+a_3xy+a_4x^2+a_5y^2+a_6r^4) \quad (3.1$$

where $r^2=x^2+y^2$, and the coefficients $a_1$ - $a_6$ were different for each view. This transformation could correct for film tilt and normal lens distortions. The old points-to-ray conversion was used, instead of the new method given in reference 10, section 2.

Best values of these coefficients and of the other optical constants were obtained by the program Mongoose[11], which is based on the fitting program Minfun. The input for Mongoose was averaged fiducial measurements from the measuring machines, and the surveyed values of fiducial positions on the chamber glass windows. The film measurements were corrected according to equation 3.1, and transformed to the front or back chamber glass fiducial plane. Then all parameters were varied to minimize the sum of squared deviations on these planes.

The geometry and kinematics results were improved considerably by these corrections (see figures 3.1 and 3.2b ). (In figure 3.1 neither rolls 21 nor 50 were processed using both methods; they were however roughly comparable, and the improvement seen was quite clear). The average

helix fit residuals and vertex residuals were also improved slightly, but the kinematics results from tau fits were the most sensitive indicators. Thresh used a similar distortion correction procedure, and the required parameters were obtained from the RHEL parameters, without refitting. The reconstruction of fiducials by both systems agreed closely.

### 3.3.5 Magnetic field calculations.

The RHEL geometry program took account of non-uniform magnetic fields, and made a full calculation of the effects of the small components of the field in the x-y plane.

Bz, the main component of magnetic field, was calculated from a polynomial fitted to field measurements made throughout the space in the centre of the chamber magnet. Bx and By were calculated from polynomials derived from the Bz polynomial by use of Maxwell's equations. These three polynomials were derived and fitted by the Birmingham $K^-$d group[12].

$$Bz = C(91)\left[a_1+a_2z+a_3(2z-r^2)+a_4(2z^3-3zr^2)+a_5(8z^4-24z^2r^2+3r^4)\right]$$
$$Bx = x.z.C(91)\left[-2a_3-a_4.3z+a_5(-16z^2+12r^2)\right]$$
$$By = y.z.C(91)\left[-2a_3-a_4.3z+a_5(-16z^2+12r^2)\right] \qquad (3.2$$

These formulae assume cylindrical symmetry, but not symmetry about the z=0 plane, unlike the formulae given in reference 9. The x, y and z coordinates had to be measured relative to a known field symmetry centre, which was near the centre of chamber.

Bx and By affected the curvature of dipping tracks; this was taken account of by correcting Bz.

$$Bz^1 = Bz+ \quad (\sin\vartheta.Bx-\cos\vartheta.By).\tan\lambda \qquad (3.3$$

This is expressed in the helix fit coordinate frame. Note that $\tan\lambda$ was reversed for negative tracks in subroutine Slope, and was restored to normal after the helix fit.

Also four field ratios were calculated, which involved Bz and the radial x-y component at three points along each track. These were used in calculations of the slowing-down corrections to the helix fit.

The r.m.s. residual between the fitted polynomial and the original field measurements was 0.3% of Bz, which was very good. The use of a polynomial rather than a table of the original field measurements saved computing time and needed fewer program instructions.

The nominal value for Bz at the field centre (C(91)) was calculated from magnet current readings, but was checked by plotting ideograms of the fitted $\bar{K}^o$ mass from kinematics neutral vee fits. As a result, it had to be corrected by up to 1%. The full width of the ideogram was about 10 MeV. The peak and the width of the ideogram varied very little when different forms of the polynomial were used.

Thresh did not calculate the magnetic field; this was done in Grind when a field table was used, calculated from the above Bz polynomial for convenience. Grind did not calculate Bx or By, nor correct Bz, nor calculate slowing-down corrections. The $\bar{K}^o$ mass ideogram had a width of about 15 MeV, compared to a width of 9 MeV found for the same events processed through the RHEL system. This reflected the more sophisticated calculation methods of the RHEL system.

A fuller discussion of the derivation of these versions of the field polynomials, and of the correction to Bz, is given in reference 13.

### 3.3.6 Choice of error constants.

The RHEL Geometry program required nine error constants of various sorts, and Thresh required even more. In general, values used by previous Imperial College or RHEL experiments were taken. However constants concerned with reconstruction errors were checked by plotting histograms of

the errors obtained from measured events, and by requiring flat distributions for fit probabilities from the Kinematics program. These constants are given in table 3.1. Only RHEL constants are discussed here.

The medians of the helix fit error histograms (figures 3.3a and b) should have been roughly equal to $\sigma_F$; in fact they were higher than this. $\sigma_F$ was used in the calculation of errors for all helix fit parameters; but if the r.m.s. measurement error was larger than a constant ($C(106)^{\frac{1}{2}}$), it was used instead of $\sigma_F$. Because these constants were close (8 and 12μ respectively), a small underestimation of both did not matter. The maximum error of 30μ was clearly satisfactory; tracks with a larger error were failed.

Two vertex errors were calculated; the first using vertex and track measurements, and the second using vertex measurements only. The histograms of these errors should have had median values close to $\sigma_F$ and $\sigma_V$ respectively; figures 3.4a and b show that this was so.

Some other error constants were checked similarly. The Thresh

Table 3.1 Values of error constants used in the Geometry programs.

| Program | Symbol | | Value used |
|---|---|---|---|
| RHEL | $\sigma_F$ | Standard track error. | 8μ (on film) |
| | $C(106)^{\frac{1}{2}}$ | Check for r.m.s. helix fit error. | 12μ |
| | NC(20) | Maximum h.f. error. | 30μ |
| | $\sigma_V$ | Standard vertex error. | 15μ |
| Thresh | - | Standard film error. | 20μ (on film)<br>250μ (on front glass) |

constants were obtained and checked by the same method. They were generally larger than the corresponding RHEL errors, probably because of the less sophisticated calculations made (see section 3.3.1).

### 3.3.7 Beam track parameters.

The average beam track momentum at entry to the bubble chamber was taken from histograms; the values used were 1.450 GeV/c for the third run, and 1.650 GeV/c for all of runs 1, 2 and 4. An average momentum error of 30 MeV/c was found from studies of tau fit probability and stretch function distributions. These values were imposed by the Geometry program on all beam tracks, as the measured values fluctuated considerably; this gave satisfactory tau fit results.

## 3.4 The Kinematic fitting program.

### 3.4.1 General description.

The RHEL Kinematics program was written by A.G. Wilson[17),18)], and the CERN program, Grind, by R. Böck and others[15)]. The principles of each are very similar, although programming details are different. The laws of conservation of energy and momentum are used to test various possible particle assignments for each event; also, for a successful assignment, these laws are used to calculate the parameters of any unseen particle, and to improve the accuracy of the parameters for the seen particles.

The program read the Geometry program results for an event from a magnetic tape. A section of the program decoded the event topology, and decided which of the particle assignment hypotheses should be tested. For each hypothesis, the parameters for any unseen particle were calculated, using the four constraint equations that express the conservation laws. Then all track parameters were varied in order to minimize the value of

the chi-squared for the fit, subject to the constraint equations. Lagrangian multipliers were used and an iterative procedure was necessary. If an event had several vertices, fits were made at each vertex successively, starting with the most highly constrained vertices; and then a multivertex fit was made. Finally new values of track parameters and error matrix elements for all successful hypotheses were written out onto a magnetic tape, and summaries were printed for all hypotheses tried.

These summaries included the predicted ionization and the stretch functions for each track. The latter were defined as:

$$\text{stretch } (X) = \frac{(X(\text{fitted})-X(\text{measured}))}{\sigma(X(\text{fitted})-X(\text{measured}))} \qquad (3.4$$

where X is one of the three track parameters. A stretch function should have a Gaussian distribution with zero mean and standard deviation of one; a different width could be caused by incorrect choice of geometry error constants, and a non-zero mean could indicate biases in reconstruction of events. Thus histograms of these functions provided useful tests of the quality of event reconstruction[19].

### 3.4.2 $P_x$, $P_y$, $P_z$ fitting.

Failure to see a spectator proton implies that its momentum is less than about 80 MeV/c, and this information can be used in the kinematic fitting. Other experiments[20] have used the normal track parameters ($^1/p$, dip angle, and azimuthal angle), but this is unsatisfactory because the errors in these parameters are not Gaussian for the unseen spectator; the spectator angles are completely unknown, and $^1/p$ can go to infinity. However, if $p_x$, $p_y$, and $p_z$, the components of momentum, are used for all tracks, with starting values zero and errors of 30 MeV/c for the spectator,

these errors are roughly Gaussian, and the expected spectator momentum distribution is approximately reproduced. (Since a particle travelling along a camera axis is unseen for a higher momentum than one travelling normal to the camera axis, a larger error in $p_z$ was appropriate, and 40 MeV/c was used.)

Events with an unseen proton spectator and a missing neutral particle, cannot be fitted without knowledge of the spectator particle, but become one-constraint fits when the above method is used. It will be seen in chapter 4, however, that results from such fits were not very satisfactory.

### 3.4.3 Selection criteria.

A hypothesis had to satisfy the following criteria before it was accepted:

1) Predicted and observed ionization must agree, within the accuracy of observation.

2) Chi-squared probability for the production vertex fit must be at least 1% for 3-and 4-constraint fits, or at least 5% for 1-and 2-constraint fits. Events with decays must have a successful multivertex fit also (i.e. at least 0.1% chi-squared probability).

3) The momentum of the proton from the production vertex must be less than 150 MeV/c for an unseen proton, or less than 350 MeV/c for a seen proton.

4) If an hypothesis involving 3 or 4 constraints at the production vertex is ambiguous with one involving 1 or 2 constraints, reject the latter; this does not apply to $\Lambda^\circ/\Sigma^\circ$ ambiguities, however.

5) The true lifetime of all charged decay fits must be within the limits specified in figure 3.5[21].

6) Accept events with up to 3 ambiguous fits; remeasure or class as unmeasureable any event with more than this.

7) Events giving only zero-constraint fits are classed as unmeasureable.

Multineutral events were not assigned to channels. No fit probability ratio tests were used to decide between ambiguous fits. Any associated electron pair, Dalitz pair, or $\pi^+ \rightarrow \mu^+ \rightarrow e^+$ decay was also used to help eliminate hypotheses.

Other groups in this collaboration did not reject events with fast seen proton spectators (criterion 3). Otherwise they used very similar criteria.

The minimum fit probability cuts were chosen after a study of 3- and 4-prong fits[22]. With a 0.1% cut these showed a large low probability "tail" for the 4-constraint fits to $K^-d \rightarrow ppK^-\pi^-$ (figure 3.8a); 4-constraint tau decay fits did not show this (figure 3.8b), so that incorrect errors or inaccurate geometry reconstruction were not the cause. Very probably, the "tail" came from contamination from events in other channels, e.g. $K^-d \rightarrow ppK^-\pi^-\pi^0$. A cut at 1% reduced the "tail" greatly, and also eliminated most ambiguities. For 1-constraint fits there was no "tail" (figure 3.9a), but a higher probability cut was chosen for safety, as misfitting is generally easier for fits with less constraints. Neutral vee and multivertex fits showed a slight bias towards low probabilities (figure 3.9b), but a cut at only 0.1% was applied, as the production fit probability cut seemed to give adequate protection against contamination.

### 3.4.4 Checks on results.

Many of the checks on the kinematic fitting results were in fact tests of the choice of errors and accuracy of reconstruction of the geometry program. Of these, the tau decay stretches and fit probabilities

and the $\bar{K}^o$ ideograms were most important and have already been discussed in sections 3.3.5 and 3.3.6.

The fitting of neutral and charged decays was studied in detail[23]. Of 127 neutral decays giving good geometry results, eight appeared to be unassociated or $K_L^o$ decays, and 95% of the rest gave satisfactory fits, with the expected stretch and probability distributions. The plots of true lifetimes for $\bar{K}^o$ and $\Lambda^o$ decays given in figures 3.10 and 3.11, agree with the expected distributions, which were given by:

$$\delta N = \frac{N(\text{total})}{T} \exp(-t/T).\delta t \qquad (3.5$$

where $\delta N$ is the number of decays seen in true time interval $\delta t$,

$t$ is the true lifetime of the decay,

$T$ is the average true lifetime,

and $N(\text{total})$ is the total number of decays occurring, which is obtained from the observed total by correcting for unseen short lifetime decays.

Average lifetimes are given in table 3.2.

Charged decays were more difficult to check; a one-prong scatter could look just like a charged decay to scanners, so that the fraction of

Table 3.2 Average true lifetimes for charged and neutral decays (in units of $10^{-10}$ seconds.)

| Decay | Average for 1.45 GeV/c run | Average for 1.65 GeV/c run | Current world average[24] |
|---|---|---|---|
| $K_S^o \to \pi^+\pi^-$ | .822±.020 | .798±.025 | .862±.006 |
| $\Lambda^o \to p\pi^-$ | 2.25±.035 | 2.34±.06 | 2.51±.03 |
| $\Sigma^- \to n\pi^-$ | 1.56±.05 | 1.59±.06 | 1.64±.06 |
| $\Sigma^+ \to p\pi^o$ | .95±.06 | .78±.06 | .81±.013 |
| $\Sigma^+ \to n\pi^+$ | .74±.04 | .81±.05 | .81±.013 |

decays fitting was not meaningful. Also most decay vertex fits were zero-constraint, and so gave neither stretch functions nor fit probabilities. However, charged decay fitting depended on vertex accuracy as well as track accuracy in much the same way as neutral decay fitting did; so the success of the neutral decay was encouraging for the charged decay fits.

The $\Sigma^{\pm}$ true lifetime distributions are shown in figures 3.6 and 3.7; the expected distribution was calculated in the same way as for neutral vees. Scanning losses were higher for $\Sigma^{+} \rightarrow p\pi^{o}$ than for $\Sigma^{+} \rightarrow n\pi^{+}$; this is because of the smaller laboratory decay angles accessible to the former, and a correction for this is discussed in chapter 5. There were many $\Sigma^{-}/K^{-}$ ambiguities but these were nearly all resolved by use of criterion 5 in section 3.4.3.

## 3.5 Preparation of Data Summary Tape.

The program Inco[25] read events from the magnetic tape written by the RHEL Kinematics program, and selected fit results for frame numbers and hypotheses specified on choice cards. For each selected fit, one record was written onto a Data Summary Tape (D.S.T.).

A choice card was punched by hand for each event giving a satisfactory fit. Up to three hypothesis names could be specified.

The D.S.T. format is given in table 3.3. Event identification, vertex positions, and track directions and momenta were recorded; further kinematic quantities were calculated by the Statistics program (see next section). The event code was zero for unique fits, and two for ambiguous fits (which appeared in successive records). The track labels were the serial numbers of the vertices between which the particle travelled, or were zero, if no vertex was involved. The track mass code was an integer number of magnitude 1-20, which specified which particle was thought to have caused the track; negatively charged particles had a

Table 3.3 Data Summary Tape Format.

Layout of a fit record.

Word no.
|
Event identification
|
↓

| | | |
|---|---|---|
| 0 | I = no. of words following in this record. | |
| 1 | Frame no. | |
| 2 | Event no. | |
| 3 | Packed hypothesis no. (12 bits per part) | |
| | i | Topology |
| | ii | Rest of hypothesis name |
| | iii | No. of constraints for fit. |
| 4 | Event code. | |
| 5 | Chi-squared of fit. | |
| 6 | Probability of fit. | |
| 7 | No. of vertices in the event. | |

For each vertex:

| | | |
|---|---|---|
| 1 | Missing mass squared | $(GeV/c^2)^2$ |
| 2 | Error on m.m.$^2$. | |
| 3-5 | x, y, and z coordinates of vertex (cms.). | |
| 6 | No. of tracks at vertex. | |

For each track at current vertex:

| | | |
|---|---|---|
| 1 | Packed code (6 bits per part) | |
| | i | Beginning label |
| | ii | End label |
| | iii | Mass code. |

Table 3.3 Data Summary Tape Format (continued).

| | | |
|---|---|---|
| 2 | Length | (cms.). |
| 3 | Azimuth | (radians). |
| 4 | Dip | (radians). |
| 5 | Momentum | (GeV/c). |

For multivertex events, chi-squared, probability and track parameters are taken from the final multivertex fit.

code of negative sign. An end-of-block record was written after all events from one input tape had been read, and an end-of-tape record was written after the last block on the D.S.T.

The $p_x$, $p_y$, $p_z$ variables for unseen spectator particles were changed to the equivalent $^1/p$, dip, and azimuth variables. For events containing two protons, the unseen proton or slowest proton was given mass code 20 instead of the usual value of 5. This indicated it as the probable spectator, and the justification for this is discussed in chapter 4.

A modified version[26] of the CERN program Slice[16] produced a D.S.T. of identical format from a Grind output tape. The program altered all the track and vertex labels and track mass codes to the RHEL systems, as well as carrying out the operations mentioned above.

After a D.S.T. had been created, some hypothesis numbers were changed by a special program, in order to have agreement with other groups in the collaboration.

## 3.6 The Statistics program.

### 3.6.1 General description.

The program[27] read a Data Summary Tape, and plotted histograms and two-dimensional scatter plots of various physical quantities, for specified hypotheses, subject to selections if required. Standard subroutines were available which calculated, for instance, effective masses for all permutations of outgoing particle pairs, momentum transfer to one or more particles, and decay angles of resonances. Many other subroutines were written specially for this experiment, and calculated, for example, the total energy in the $K^-n$ centre of mass system, particle momenta and directions in the laboratory system, and lifetimes and decay

angles for charged and neutral weak decays.

The standard selections available were for effective mass of any particle combination, missing mass, momentum transfer and for $\cos\vartheta$, where $\vartheta$ is the centre of mass production angle for any single particle or combination of particles. Other selections were added for track length, momentum and dip, for beam track parameters, centre of mass energy and decay polar angles. Up to three selections or anti-selections on these quantities could be specified for any one plot. Events could be selected or rejected singly according to frame number, or in blocks according to the block number. The latter facility allowed events from different groups to be plotted separately, as such events were written in different blocks on the D.S.T. Unique and ambiguous fits could be plotted separately or together.

Histograms could be plotted with each event weighted to correct for charged or neutral decays that had occurred either outside the chamber, or so close to the collision vertex that they were not detected[28) 29)]. The method used is described in chapter 5.

For two-dimensional plots, information was written on a temporary output magnetic tape, which was read through after being completed. This tape could be kept to provide input data for other programs.

The advantages of this program compared to the CERN program SUMX[30)] are that the writing of data for histogram plotting is much simpler, and that since the D.S.T. contains less information for each event, it can be read much more quickly. However, disadvantages also exist; the data-uniting for two-dimensional plots is rather complicated, and also "or" combinations and complex "and" combinations of selections cannot be made.

### 3.6.2 Special facilities for deuterium collisions.

For each hypothesis, a particle could be specified that was to be excluded when defining the centre of mass-systems; thus events could be plotted as collisions on the neutron, proton, or deuteron (if no spectator was specified). Also events could be plotted only if one of the outgoing baryons (usually the proton) was slower than the other. This slower baryon was the probable spectator.

Unseen spectators had their length set zero or negative in the Kinematics program, and this was the most convenient way to distinguish these events from seen spectator events. One of the new selections could select on this length.

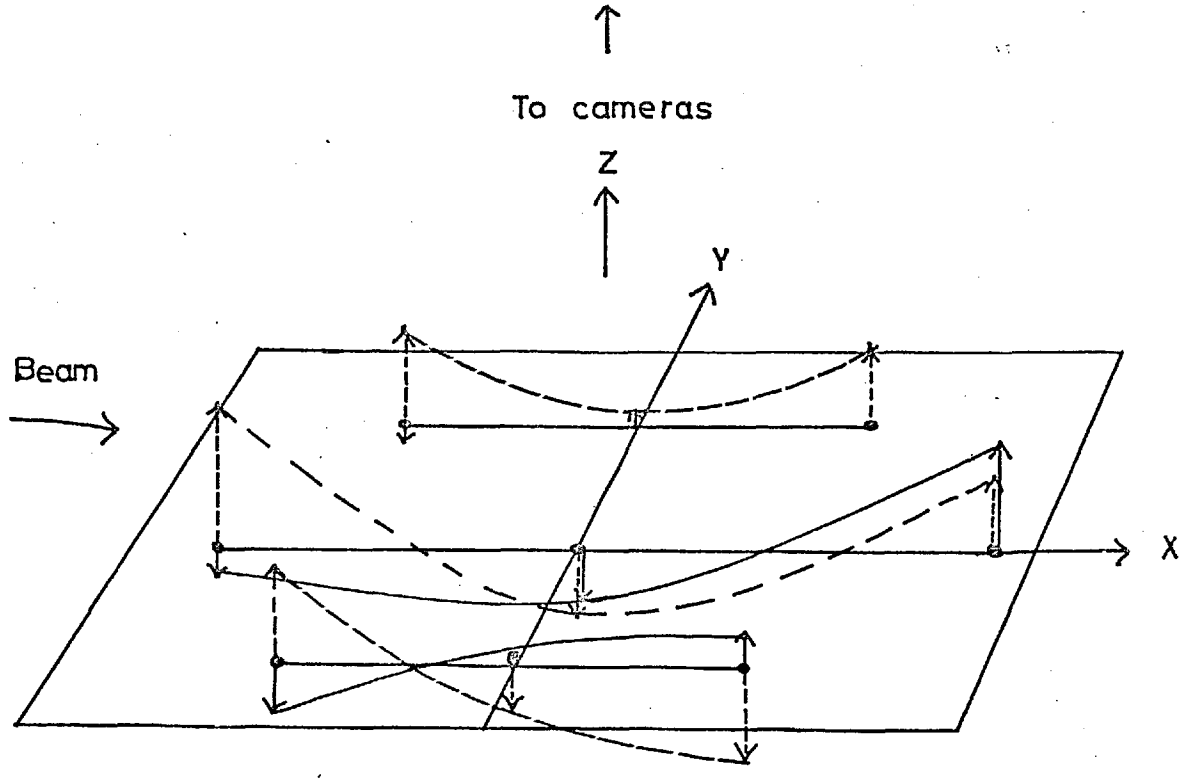


I 1mm. Scale of residuals.

10 cms
10 cms
Scale of X—Y plane.

= Average residual in Z, roll 50, no distortion correction.

= Same, for roll 21, with distortion correction.

FIGURE 3.1 RECONSTRUCTION OF BACK-GLASS FIDUCIALS.

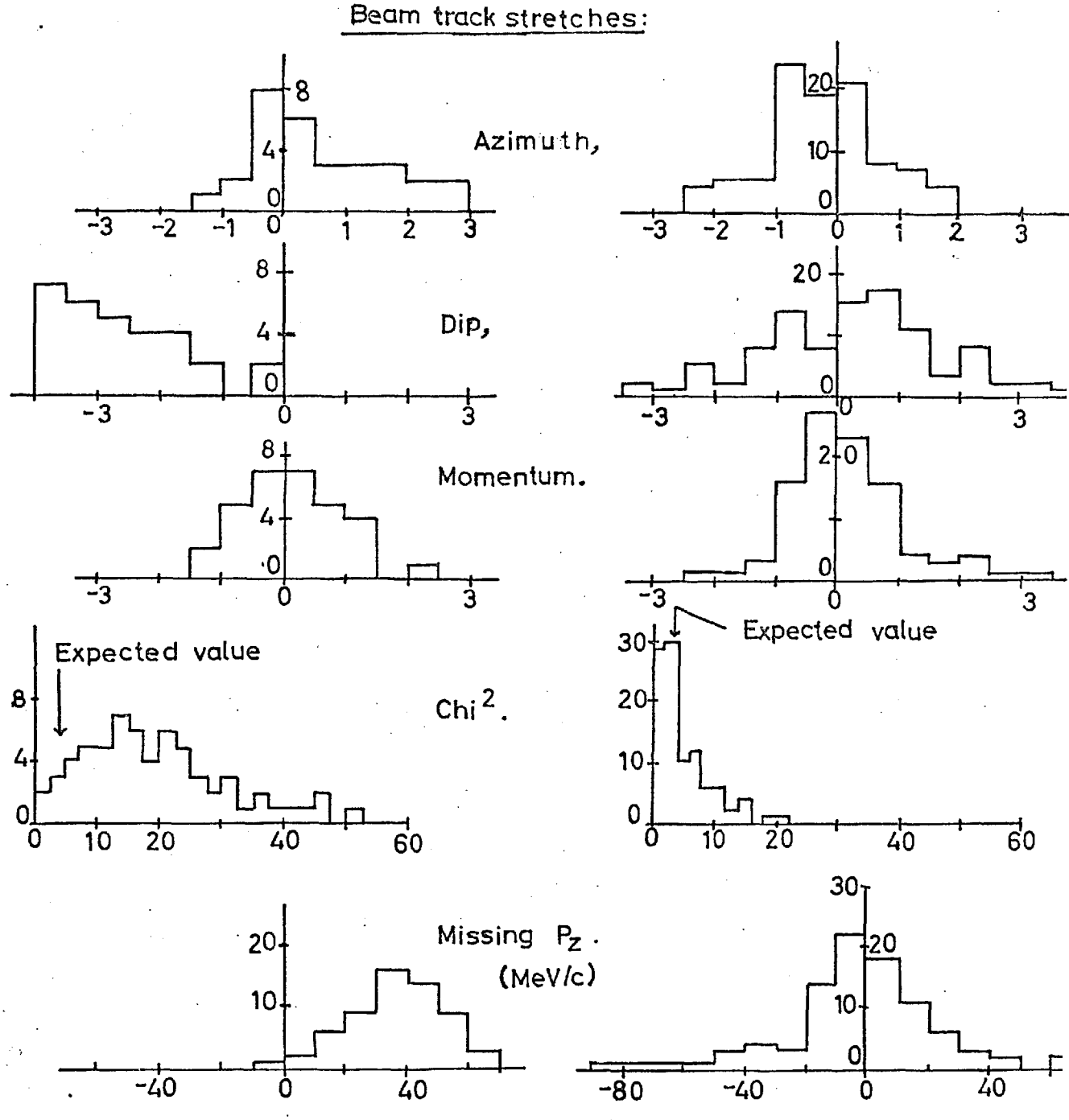


a) No distortion corrections. b) with distortion corrections.

FIGURE 3.2 TAU DECAY FITS.

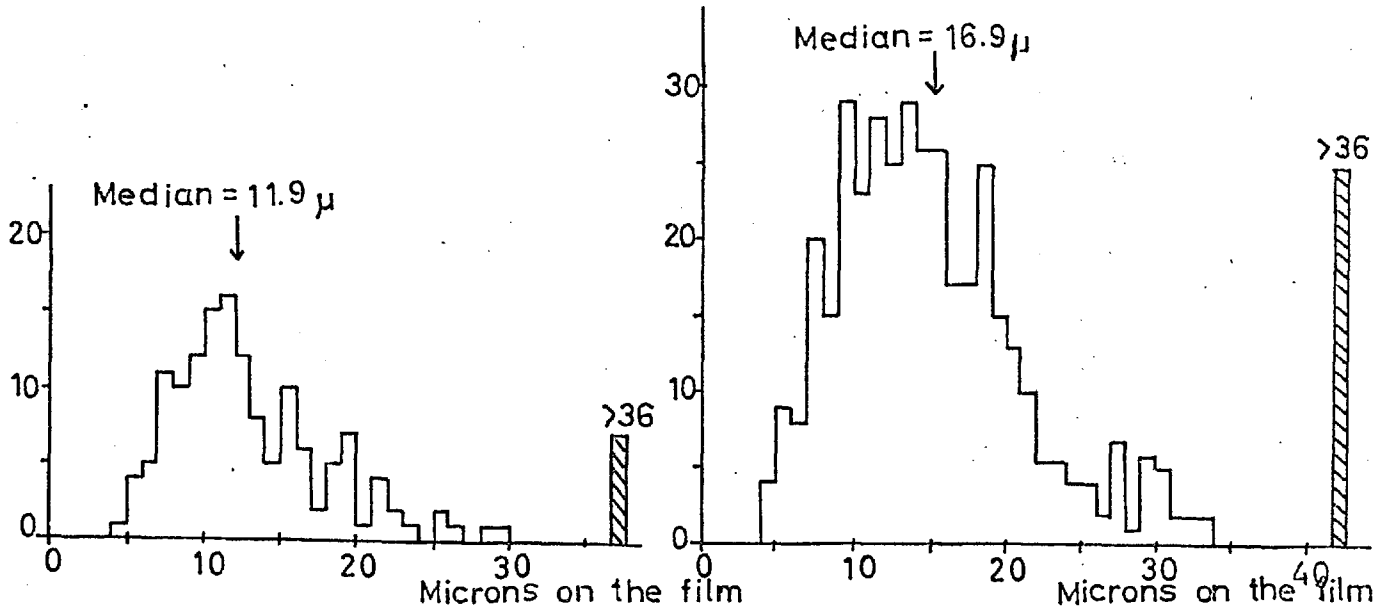


a) Beam tracks longer than 2 5cms. 130 tracks

b) Non beam tracks. 394 tracks

FIGURE 3.3 HELIX FIT ERRORS. (2nd run at 1.65 GeV/c)

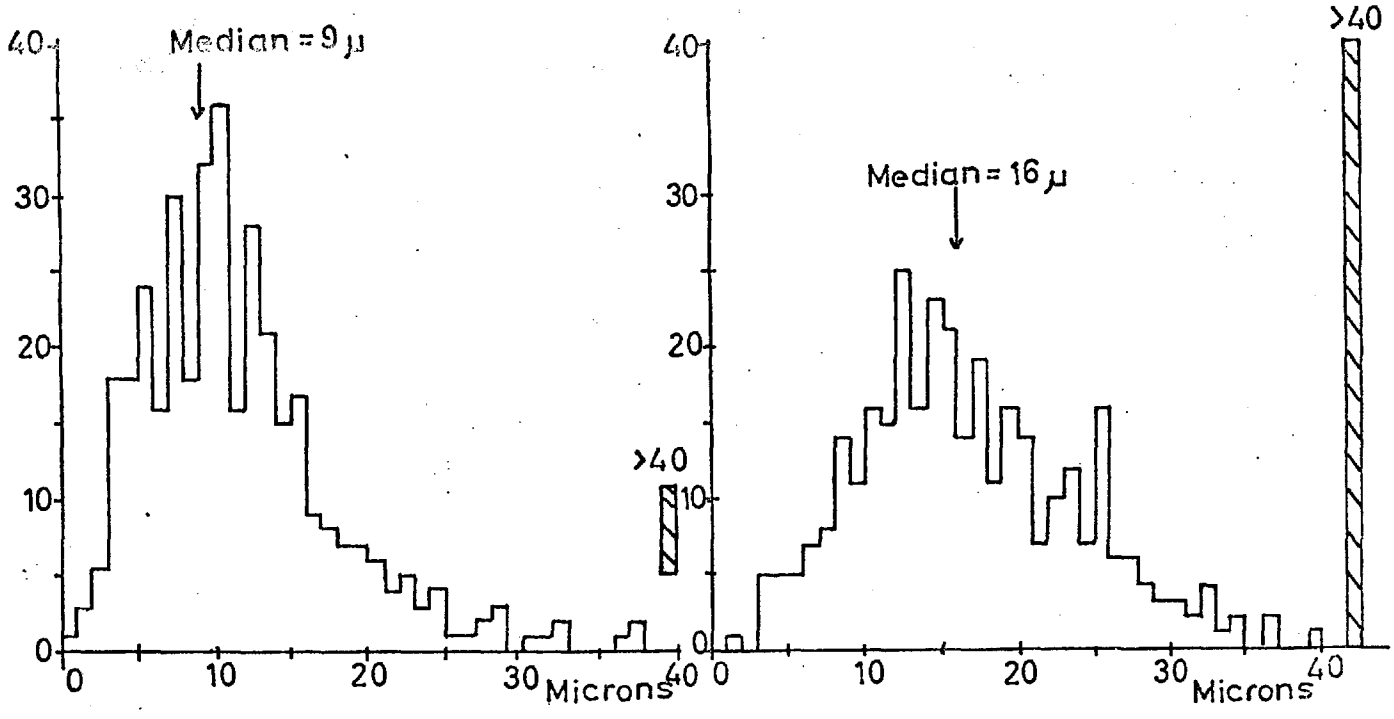


a) From track measurements. (first error) 160 events.

b) From point measurements. (second error) 160 events.

FIGURE 3.4 VERTEX ERRORS, ON FILM.

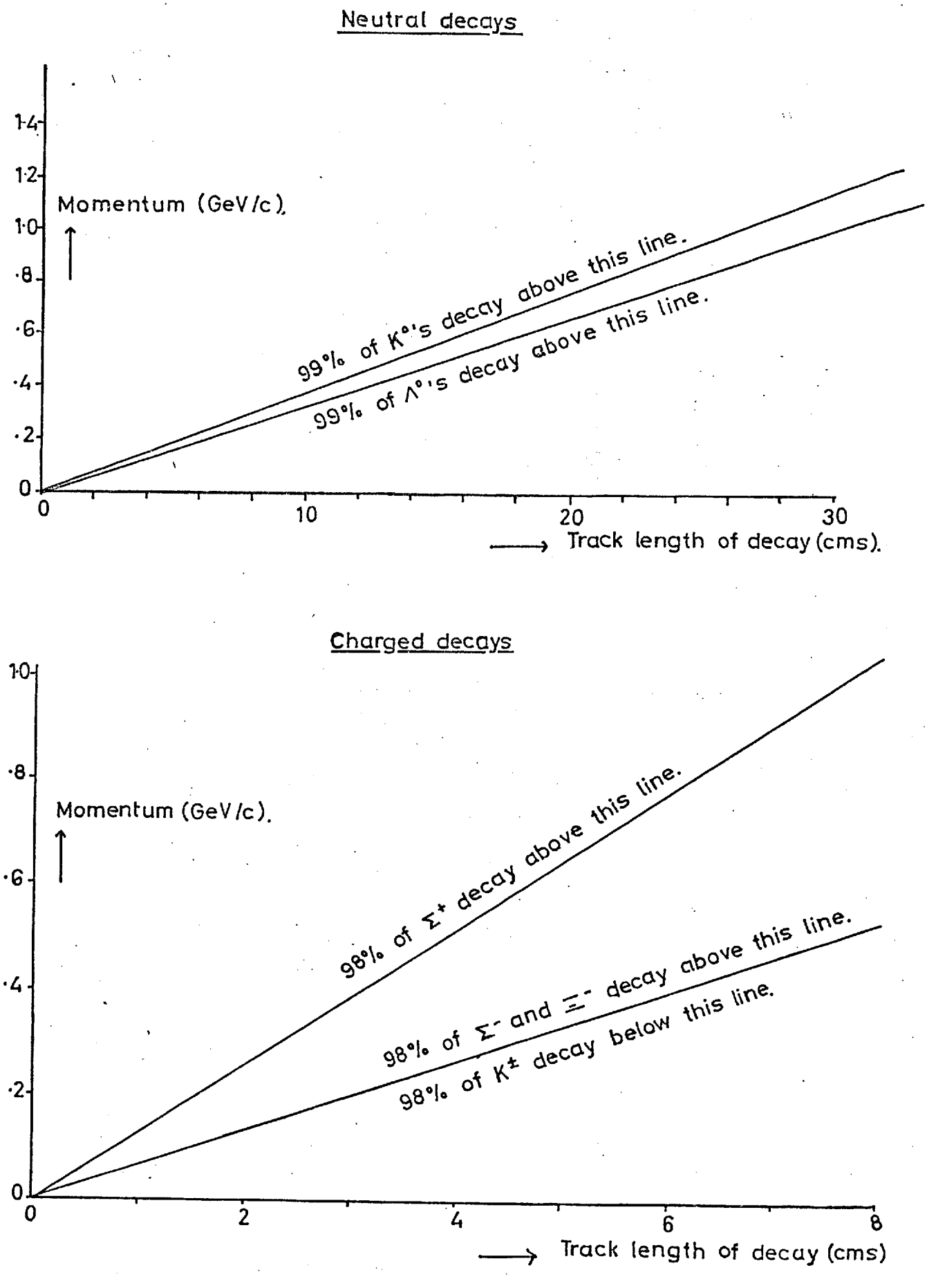


FIGURE 3.5 CHECKS ON TRUE DECAY LIFETIME.

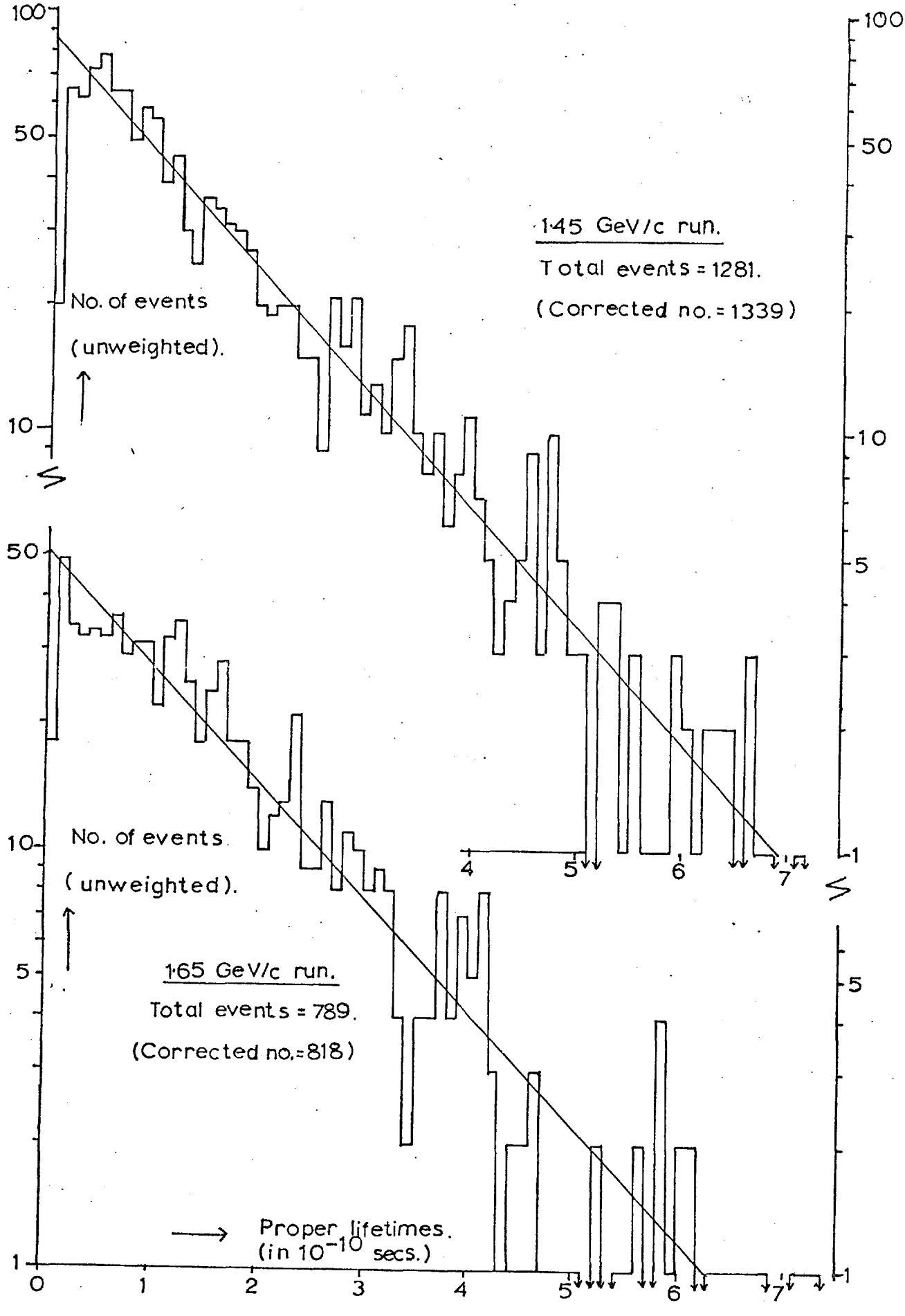


FIGURE 3.6 LIFETIMES FOR $\Sigma^- \rightarrow n\pi^-$.

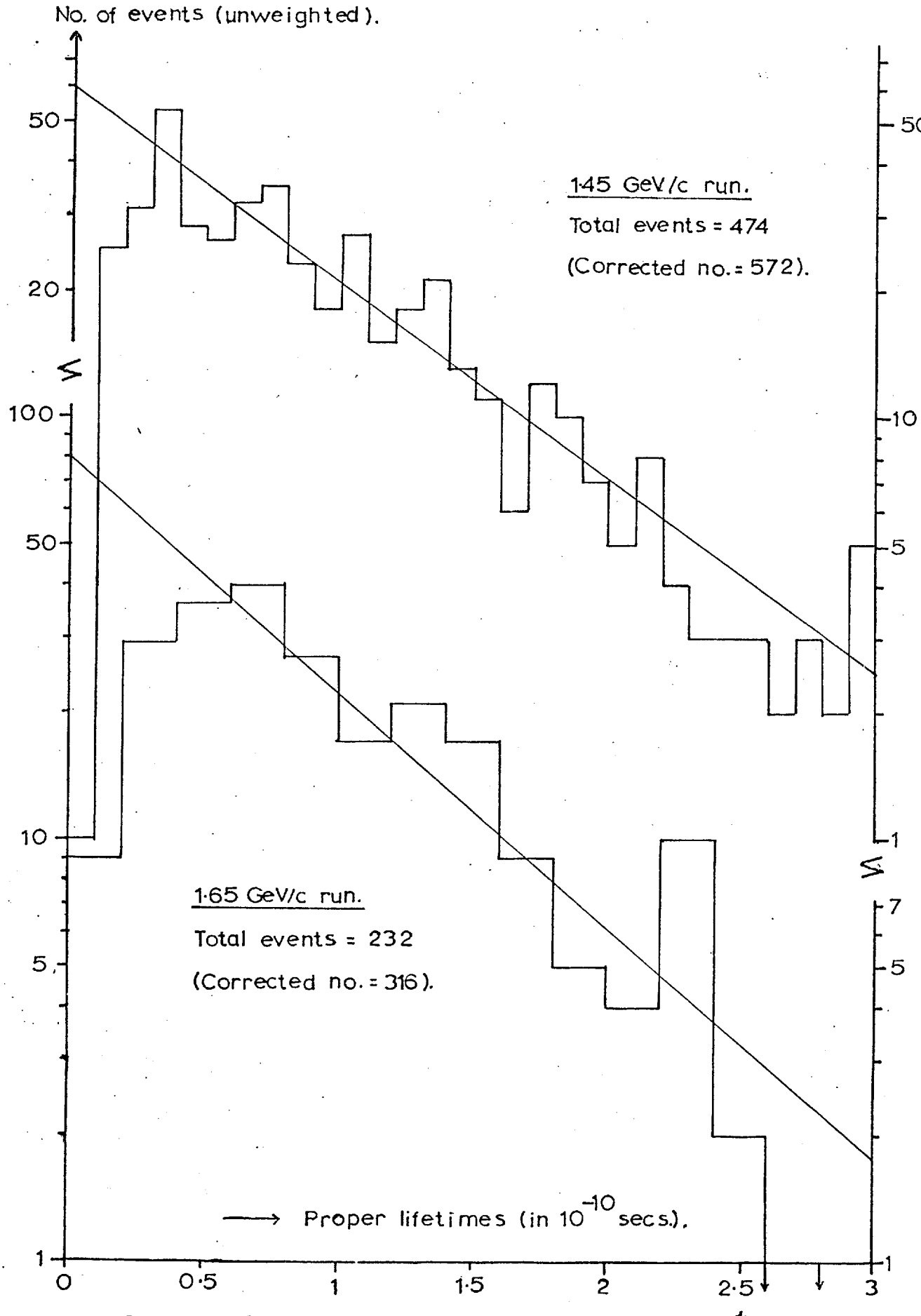


FIGURE 3.7a LIFETIMES FOR $\Sigma^+ \rightarrow p\pi^\circ$.

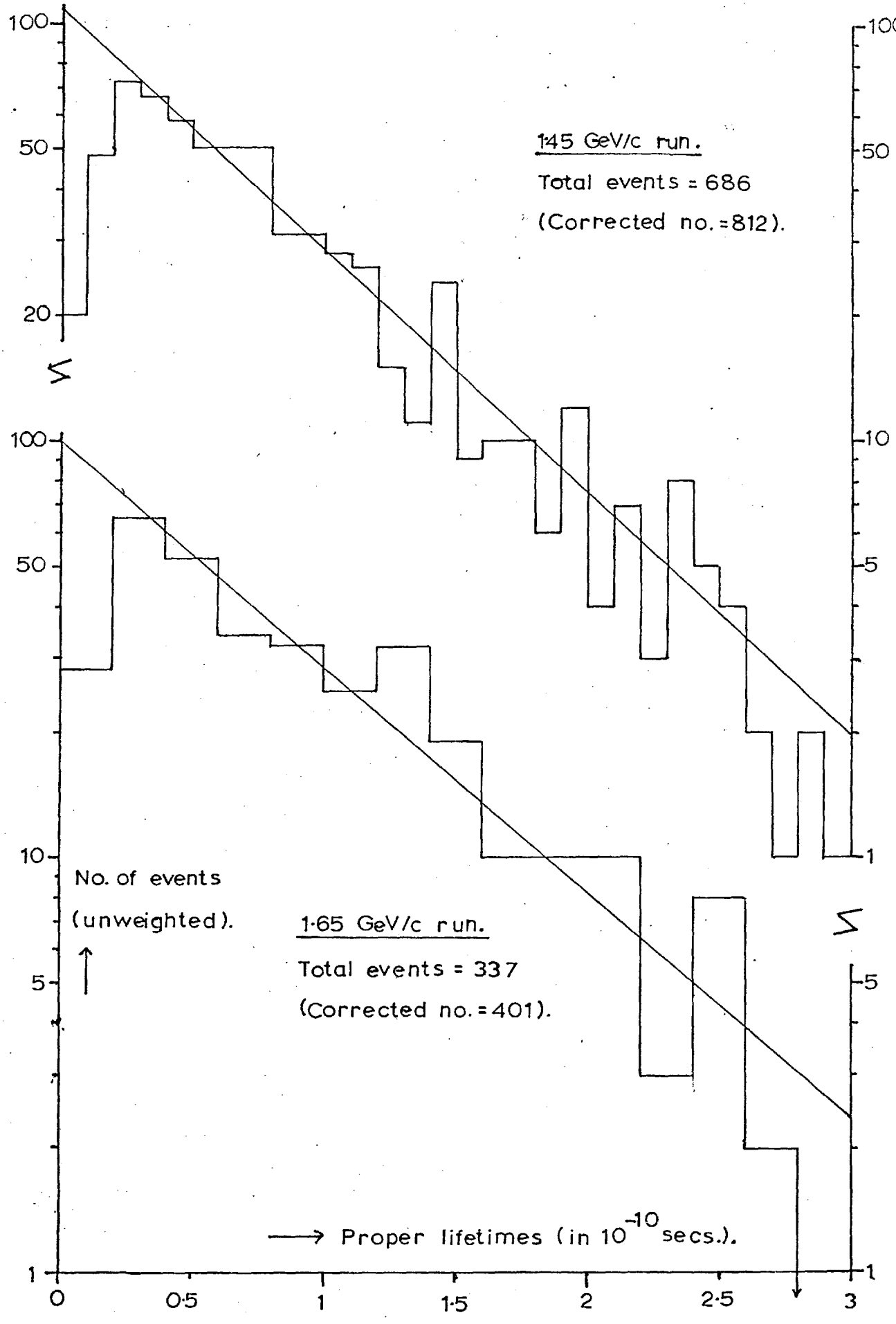


FIGURE 3.7b LIFETIMES FOR $\Sigma^+ \to n\pi^+$.

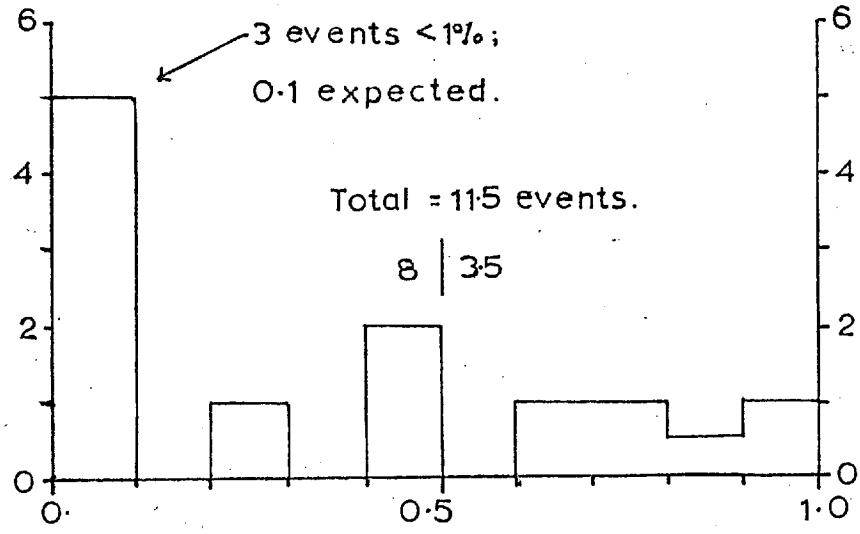


a) 4-constraint fits to $K^-d \to K^-\pi^-pp$, with prob. > 0·1 %. Unique and ambiguous events from 8 rolls of 1·65 GeV/c film.

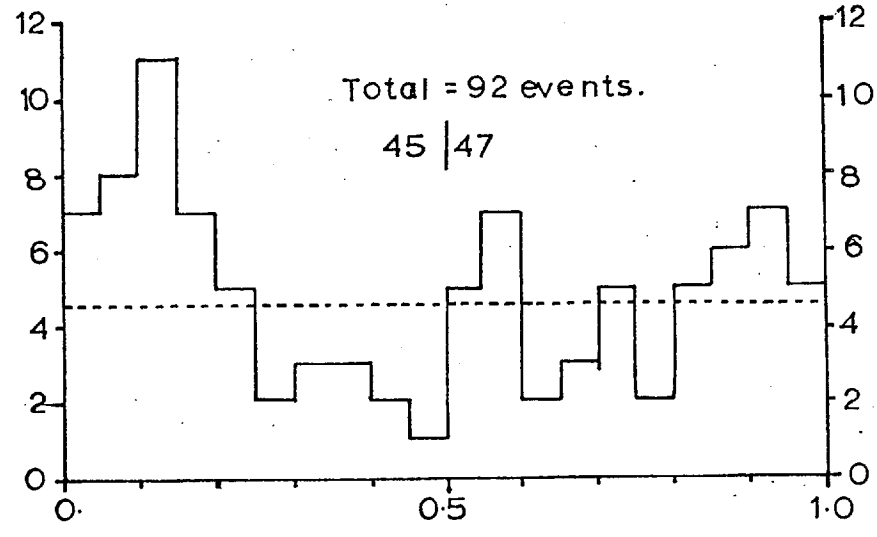


b) 4-constraint fits to tau decays, with prob. > 0·1 %. Unique and ambiguous events from 80 rolls of 1·65 GeV/c film.

FIGURE 3·8 FIT PROBABILITIES.

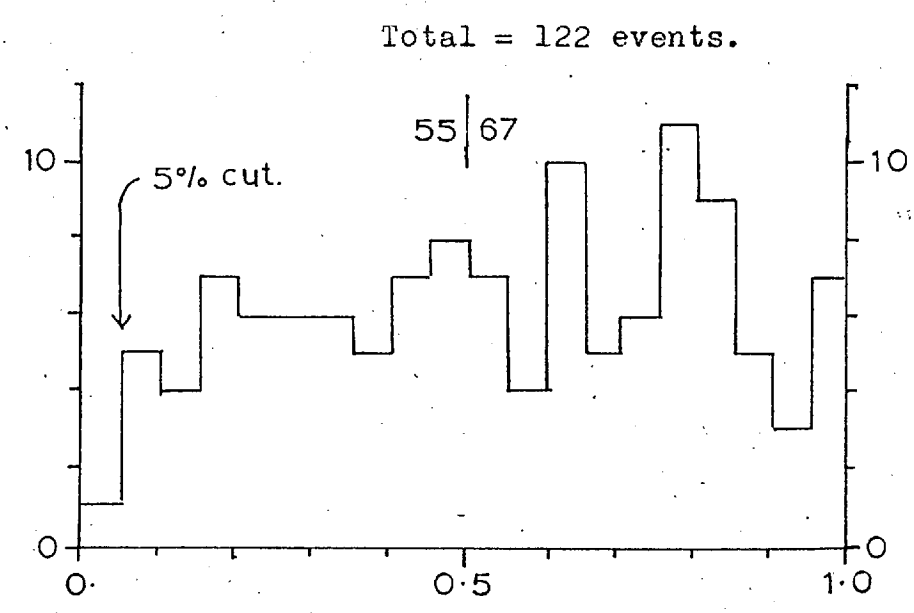


a) 1-constraint production vertex fits for all rel--evant $V^0$ and charged decay fits. Unique events from 21 rolls of 1·65 GeV/c film.

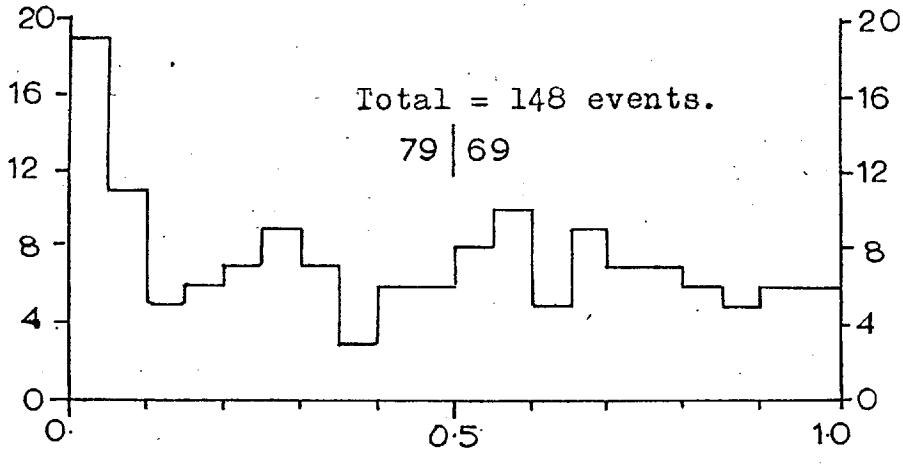


b) 4-constraint multivertex fits to the reactions $K^-d \to \bar{K}^0\pi^-np$ , and $K^-d \to \Lambda^0\pi^-\pi^0p$ , which give 1-constraint prod. fits. Unique events from 80 rolls of 1·65 GeV/c film.

FIGURE 3·9 FIT PROBABILITIES.

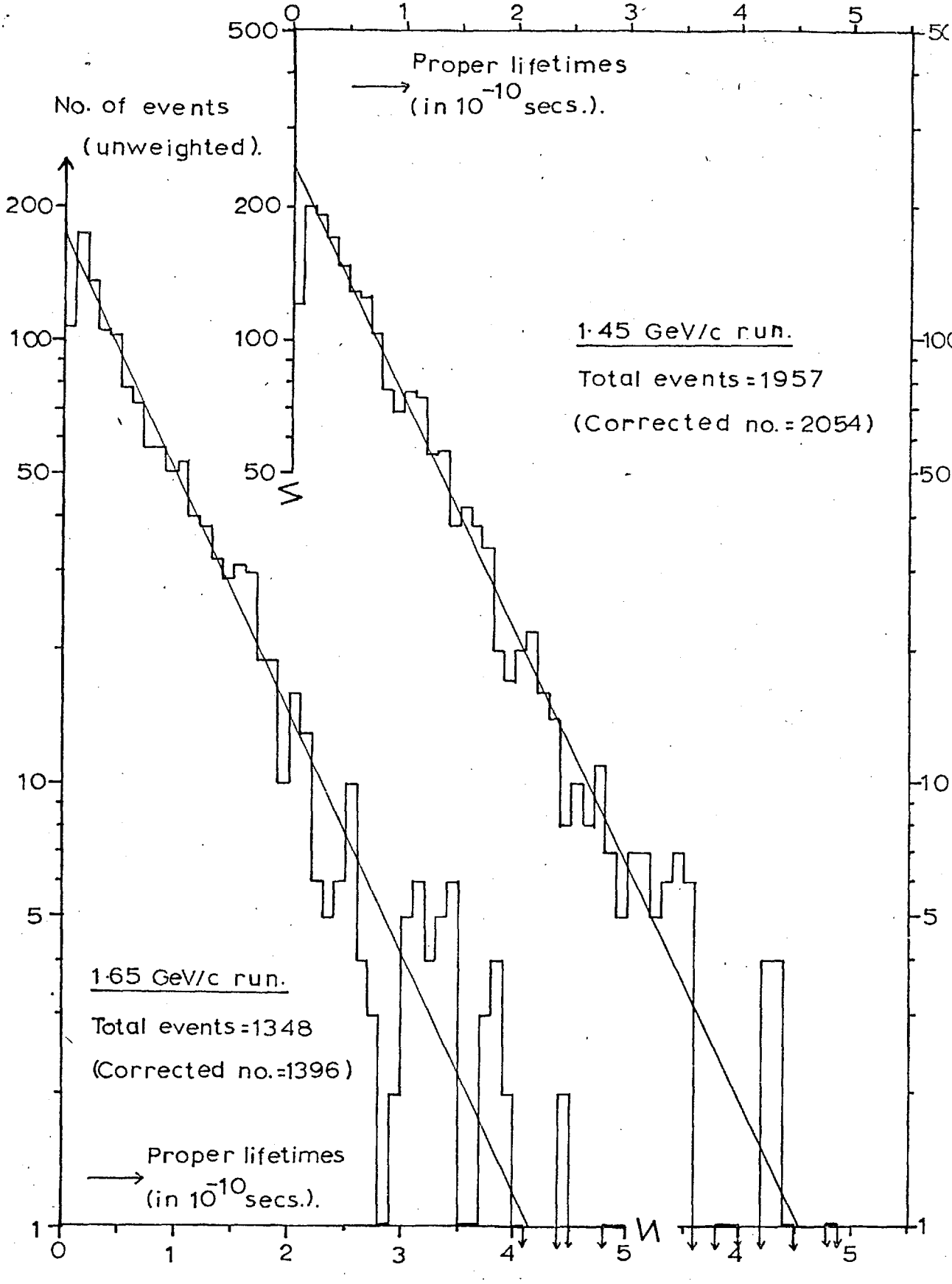


FIGURE 3.10 LIFETIMES FOR $K^0_S \to \pi^+ \pi^-$.

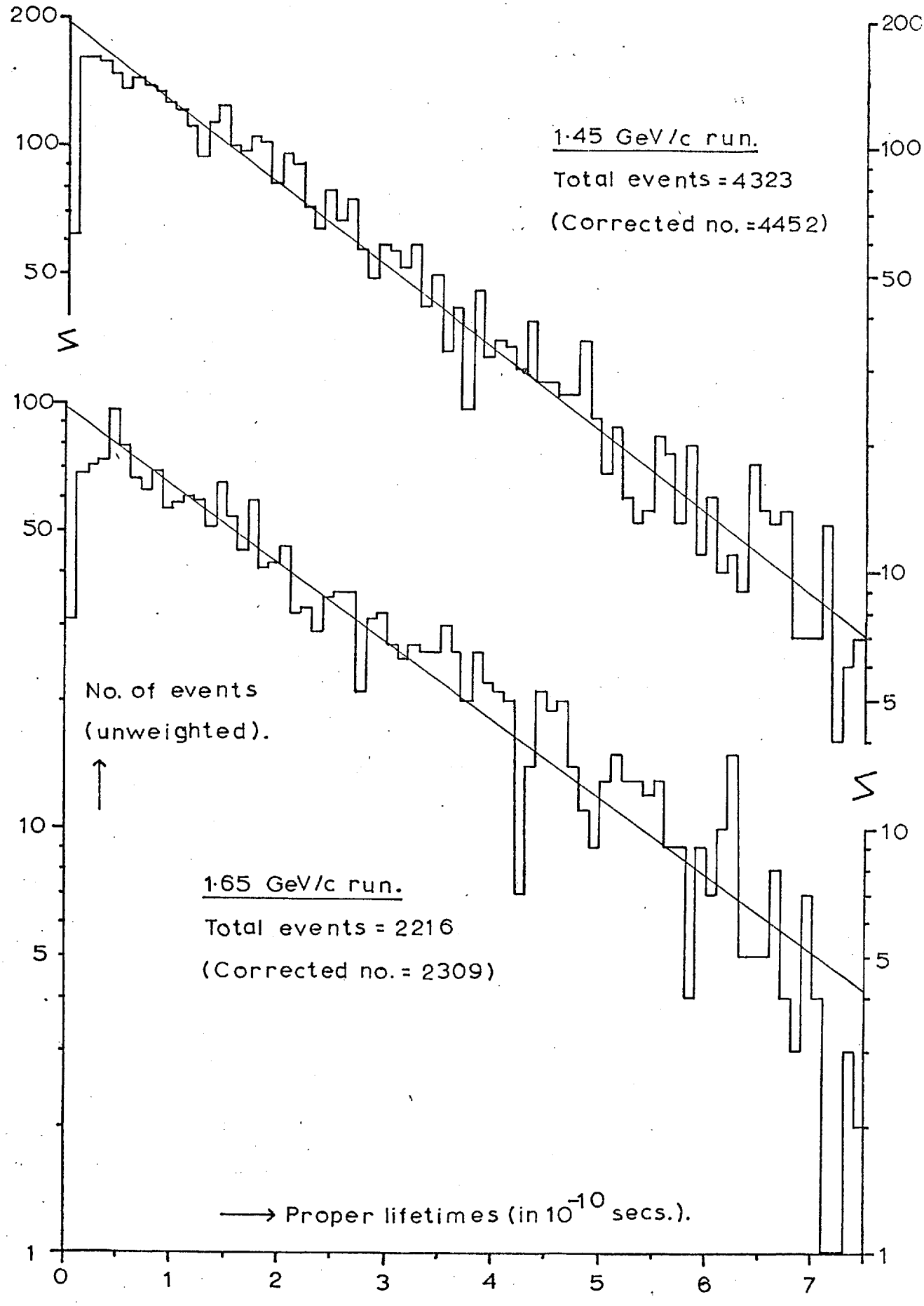


FIGURE 3.11 LIFETIMES FOR $\Lambda^0 \rightarrow p\pi^-$.

## CHAPTER 4 Selection of events satisfying the impulse approximation.

### 4.1 Introduction.

In order to study $K^-n$ interactions in a deuteron, use must be made of the impulse approximation[31-34], which supposes that a collision takes place with a single target nucleon, while the other nucleon remains a "spectator" with its momentum unaffected by the collision. The formal requirements for the validity of this approximation are:

a) The incident particle never interacts strongly with more than one constituent of the system at the same time (i.e. no double scattering).

b) The amplitude of the incident wave is nearly the same for bound and free nucleons.

c) The binding forces can be neglected for the duration of the strong interaction. (Only this criterion corresponds to the impulse approximation in classical scattering theory.)

The deuteron is weakly bound (binding energy = 2.23 MeV), and the mean separation of the nucleons is 4 Fermis. This indicates that a high percentage of collisions will be describable by the approximation , although the criteria for selecting events that satisfy the approximation must be established empirically.

For all calculations, the wave function formulated by Hulthén[35] has been used, namely:

$$\psi(\underline{r}) = (\text{Constant}).\frac{e^{-\alpha r}}{r}.(1-e^{-\mu r}) \qquad (4.1$$

with $\alpha = .232$ Fermi$^{-1}$, and $\mu = 4.2\ \alpha$[36]

Although this expression is conveniently simple, it is not reliable at small nucleon separations, i.e. high relative nucleon momenta;

it deviates from a more accurate description by more than 25%, for a momentum larger than 260 MeV/c[36].

The Hulthén function gives rise[42] to the following nucleon momentum distribution:

$$P(p)dp = (\text{Const.}).p^2 \left[\frac{1}{\alpha^2+p^2} - \frac{1}{\beta^2+p^2}\right]^2 dp \qquad (4.2$$

$\beta = \alpha+\mu$

This distribution predicts that the probability of a nucleon being faster than 300 MeV/c is only 1%. It is shown in section 4.3 that because of double scattering and failure of the Hulthén function, considerably more fast nucleons are observed.

## 4.2 Choice of spectator particle.

The spectator momentum should be distributed according to equation 4.2, i.e. peaked at 80 MeV/c with less than 1% above 300 MeV/c, whereas the recoil baryon typically had a fairly flat distribution ranging from 80 to 1500 MeV/c. It was therefore reasonable to choose the slowest nucleon as the spectator. To ensure agreement with the impulse approximation an upper limit of 280 MeV/c was imposed for this slower nucleon, (this is discussed in section 4.3). These criteria have been used by most previous deuterium bubble chamber experiments, although the choice of upper momentum limit varies considerably; see for example references 37 to 40.

If a hyperon and a proton are seen in the final state, then, to the extent that double collisions are ignored, the hyperon has to be the recoil baryon. The proton has always been selected as the spectator in these channels, even where the hyperon is slower. A study of such channels can indicate how reliable it is to choose the slowest nucleon as the

spectator for the nucleon-proton (N-p) channels.

Plots were made of p(proton) versus p(second baryon) for eight common channels[41]:

| | | | |
|---|---|---|---|
| $K^-d \to \Lambda^0 p\pi^-$ <br> $\quad \hookrightarrow p\pi^-$ | (4.3) | $K^-d \to \Sigma^+\pi^-\pi^-$ <br> $\quad \hookrightarrow n\pi^+$ | (4.7 |
| $K^-d \to \Lambda^0 p\pi^-\pi^0$ <br> $\quad \hookrightarrow p\pi^-$ | (4.4) | $K^-d \to ppK^-\pi^-$ | (4.8 |
| $K^-d \to \Sigma^-\pi^+\pi^-$ <br> $\quad \hookrightarrow n\pi^-$ | (4.5) | $K^-d \to ppK^-\pi^-\pi^0$ | (4.9 |
| $K^-d \to \Sigma^+\pi^+\pi^-$ <br> $\quad \hookrightarrow p\pi^0$ | (4.6) | $K^-d \to pn\bar{K}^0\pi^-$ <br> $\quad \hookrightarrow \pi^+\pi^-$ | (4.10 |

(Only events scanned at Birmingham and Glasgow were used because of the more restrictive criteria imposed at Imperial College: see section 2.2.2).

A total of 3300 events were plotted.

On all scatter plots, six regions were defined, and are shown in figure 4.1.a. (The use of 300 MeV/c rather than 280 MeV/c as a boundary has only a small effect on the conclusions below). Figures 4.1b, c and d show the appearance of typical plots. For events producing two protons the momentum of the faster is plotted as the ordinate, and so only half the plot is populated.

For the hyperon-proton (Y-p) channels, events in regions 1, 2 and 4 were selected as having a proton spectator satisfying the impulse approximation. However, if the spectator was selected as the slower baryon, events in regions 4 and 5 would have the hyperon incorrectly chosen as the spectator; the fraction of events in these regions averaged 2% for the Y-p channels.

When there were two nucleons in the final state, only the

criterion that the slower nucleon is the spectator was used. It was assumed that this criterion could be in error in the same way as for the Y-p channels, and the figure of 2% was corrected for the different spectator and recoil baryon momentum distributions in each channel. It was then found that the method was in error for 4% of events in channels 4.8 and 4.10 (proton spectator events only) and for 1% of channel 4.9; also 1% of the proton spectator events in channel 4.10 were incorrectly identified as neutron spectator events, since they occurred in region 4. The reliability of the criteria for events in regions 1 and 4, where both nucleons are slow, was confirmed by plotting momentum distributions for these events; the spectator and recoil nucleon distributions were markedly different. Figure 4.2 shows the plots for channel 4.8. Another interesting conclusion is that most of the wrong identification was caused by double scattering, where the "recoil" nucleon happened to be slow, and the "spectator" fast; it is therefore especially important to know the size of the effect.

To summarize, the use of these criteria resulted in a zero misidentification of the spectator particle for the hyperon-proton channels, and 4% or less for the nucleon-proton channels. This should not bias the data seriously.

## 4.3 Choice of maximum spectator momentum to ensure agreement with the impulse approximation.

In figures 4.3, 4.4, and 4.5, histograms are given of the momentum, the cosine of polar angle (i.e. $\cos\vartheta$), and the azimuth angle ($\varphi$) for the spectator proton, in four of the common channels listed in section 4.2. All quantities are defined in the laboratory frame of reference, and angles are defined with respect to the beam direction.

$$\varphi(a) = \cos^{-1}\left[\frac{(\underline{B} \times \underline{z}) \cdot (\underline{B} \times \underline{a})}{\underline{B} \times \underline{z} \quad \underline{B} \times \underline{a}}\right] \qquad (4.11$$

"B" represents the beam particle, "a" the outgoing particle, and "z" the z axis, taken parallel to the optic axes.

Events from all laboratories are plotted, and include about one-third of the final data at 1.65 GeV/c. The Hulthén curves plotted are calculated from equation 4.2, and are normalised to the number of events with seen spectators from 80 - 300 MeV/c for 4.3 a and b, and to the total number of events with spectators slower than 300 MeV/c for 4.3 c and d. The first two channels give distributions widely different from those expected, when the spectator is unseen. This is not caused by deviations from the impulse approximation, and is discussed in section 4.5.

The events with the "spectator" faster than 300 MeV/c showed three effects. Firstly, there were more than the 1% expected from the Hulthen function - see table 4.1; secondly, the spectator cos$\theta$ distribution showed an excess in the forward direction; thirdly, effective mass combinations involving the "spectator" showed some resonance formation. The first effect was not proof of breakdown of the impulse approximation, as it has already been noted that the Hulthén distribution is inaccurate for fast nucleons. But the last two effects clearly indicated that double collisions were taking place. The maximum of 300 MeV/c was a first estimate of the cut-off momentum; later inspection of the spectator momentum distributions indicated that 280 MeV/c was a better value to use.

All events with spectators faster than 280 MeV/c were rejected when making physics plots, but were taken into account in calculations of

cross-sections. Table 4.1 shows the fractions of such events for channels 4.3 to 4.10.

Table 4.1 Events with "spectator" faster than 300 MeV/c, expressed as a fraction of all events.

| Channel | Fraction(%) | Channel | Fraction(%) |
|---|---|---|---|
| 4.3 | 19.0±2.5 | 4.7 | 14.1±3.5 |
| 4.4 | 20.8±1.5 | 4.8 | 8.2±1.1 |
| 4.5 | 23.2±2.8 | 4.9 | 17.3±3.8 |
| 4.6 | 15.7±4.2 | 4.10 (proton spec.) | 8.1±1.6 |

## 4.4 Agreement with the impulse approximation for events with proton spectator slower than 280 MeV/c.

Let us now consider the events with slower spectators, ignoring, for the moment, events with an unseen proton spectator together with an unseen neutral particle. The momentum spectra (figure 4.3) agree with the Hulthén curve, and no systematic deviations are seen. The two angular distributions (figures 4.4 and 4.5) are isotropic, as expected, apart from a small excess of forward events in the $pn\bar{K}^{o}\pi^{-}$ and $\Lambda^{o}p\pi^{-}\pi^{o}$ channels. An excess of unseen spectators was expected for $\varphi$ equal 0 or $\pi$, because of poor visibility for tracks parallel to the optic axes; this was observed, but was too small an effect to show up in figures 4.3 c and d.

The spectator momentum, $\cos\vartheta$, and $\varphi$ distributions for the other four channels specified in section 4.2 were also in reasonable agreement with the expected distributions.

It has been pointed out by Bigata[42] that the spectator momentum and cosθ distributions may not agree with the Hulthén prediction for two reasons; firstly, the cross-section is modified because of the moment of the neutron target by a"flux factor"; secondly, the variation of cross-section with centre of mass energy may bias the momentum spectrum. The azimuthal angular distributions should be flat, independently of these effects.

The flux factor, R is given by:

$$R = \frac{p_K\ (Md - Ep)}{p''_K \cdot X} \qquad (4.12$$

Where Ep = spectator energy in laboratory.

Md = mass of deuteron.

$p_K$ = momentum of incident $K^-$ in laboratory.

$p''_K$ = momentum of incident $K^-$ in $K^-n$ centre of mass system.

X = total energy in $K^-n$ centre of mass.

$$\text{Then } \sigma_o = \sigma_A \cdot R \qquad (4.13$$

Where $\sigma_A$ = cross-section calculated neglecting momentum of target.

$\sigma_o$ = corrected cross-section.

Take the ordinary spectator momentum distribution $\frac{dN}{dp}$, and calculate $f(p) = R\frac{dN}{dp}$ .(p is the proton momentum). Then it can be shown[42] that the function H(p), defined below, should have a flat distribution.

$$H(p) = \int_o^p f(k).dk \qquad (4.14$$

Bigata obtained a flat distribution for H(p), at a 35% confidence level.

For this experiment, the uncorrected plots agree reasonably well with the impulse approximation, and so it seems unnecessary to make more rigorous checks. It is, however, interesting to estimate what qualitative effects should arise from the neglect of these corrections.

The effect on the spectator momentum distribution is hard to estimate; but for a given value of p, opposite values of $\cos\vartheta$ have an opposite effect and hence tend to cancel. For the spectator $\cos\vartheta$ distributions we have:

$$\frac{dN}{d\cos\vartheta} \simeq \frac{\sigma_o}{R} \qquad (4.15$$

As $\cos\vartheta$ increases from -1 to +1 the value of x increases, and so R falls. Since most channels have a cross-section that falls with increasing energy, $\sigma_o$ also falls. Thus the two corrections tend to cancel. This indicates that the agreement with theory obtained from our uncorrected plots is meaningful.

A further test of the impulse approximation is to calculate the cross-section obtained for the $\Lambda^o\pi^-$ channel by unfolding the Fermi motion, using the Hulthén momentum distribution, and compare it with that obtained for $K^-p\to\Lambda^o\pi^o$. This $K^-p$ channel is pure isospin 1, and should have a cross-section equal to half of that for the $K^-n$ channel. Figure 4.6 shows values of $A_o$ obtained by this experiment and by several $K^-p$ experiments.

$$A_o = \frac{\sigma}{4\pi\lambda^2} \qquad (4.16$$

where $\lambda = \frac{\hbar}{p''_K}$ and $p''_K$ = $K^-$ momentum in $K^-n$ centre of mass.

The first four experiments were collected and fitted by Smart[43], and the line obtained by him is plotted. An experiment by Berthon et al.[44] found significant disagreement with the data points of Wohl et al.[45], and pointed out that the latter group did not make any correction for contamination of $\Lambda^0\pi^0$ fits by $\Sigma^0\pi^0$ events. The results from this experiment[46] were obtained from events with seen spectators of momentum 100 - 280 MeV/c and were subject to an overall uncertainty of 10% in addition to the error bars shown. Our points agree well with those of Berthon et al., although one point at 1.96 GeV shows a $2\frac{1}{2}$ standard deviation difference. Also our results agree well with those of Louie et al., Trower and Dauber et al., but disagree with the results from Wohl et al., and thus reinforce the possibility of the latter being in error. (For $K^-n\to\Lambda^0\pi^-$, contamination from $\Sigma^0\pi^-$ is smaller than for the equivalent $K^-p$ channels, and can be satisfactorily removed[47) 48].)

Bigata also compared $\Lambda^0\pi$ cross-sections from two $K^-n$ and $K^-p$ experiments, carried out in the same bubble chamber and subject to similar biases, and found excellent agreement.

## 4.5 Reliability of $P_x$, $P_y$, $P_z$ fits.

Channels with an unseen spectator and no neutral particle can be fitted by the conventional method, subject to one constraint, or by the $P_x$, $P_y$, $P_z$ method (see section 3.4.2), subject to four constraints. Both methods gave satisfactory spectator distributions (see figure 4.3, 4.4, and 4.5, parts c and d), and gave nearly identical results for other particles, except that the four-constraint fits gave slightly smaller fit errors. Another small advantage of the $P_x$, $P_y$, $P_z$ method was that events with one straight track could be fitted with three constraints, whereas these events would give only zero-constraint fits by the conventional method. The effective mass resolution (equation 4.17) and angular distributions from both methods agreed well with those for the same

channel where the spectator was seen.

Channels with an unseen spectator, and a non-decaying neutral particle cannot be fitted by the conventional method, and give only one-constraint fits by the $P_x$, $P_y$, $P_z$ method. The spectator distributions (figures 4.3, 4.4, and 4.5, parts a and b) are quite different from those expected, and also effects are seen in plots involving the non-spectator particles (for example, see figure 4.7). The cause of this seems to be that the fit is so weakly constrained that the three components of spectator momentum cannot be pulled far enough from their starting values; therefore the spectator momentum spectrum peaks at zero, not at about 40 MeV/c as expected. Also, most of the "pulling" of the spectator momentum takes place along the beam direction, as the momentum errors from measurement are largest in this direction. Thus the distribution of $\cos\vartheta$ for the spectator displays a large excess of events in the forward and backward directions. The anisotropy of the spectator $\varphi$ distribution is probably caused by the choice of an error in $P_z$ larger than those in $P_x$ and $P_y$; it seems that the three errors should have been made equal.

This misfitting of the spectator meant that the neutral particle was also badly fitted, and the centre of mass energy and the definition of the c.m. reference system were both wrong. The first effect was seen in an extensive study of effective mass distributions[49]. The mass resolution $\Delta M$ was calculated for several prominent resonances.

$$(2.\Delta M)^2 = \Gamma_M^2 - \Gamma_E^2 \qquad (4.17$$

$\Gamma_M$ and $\Gamma_E$ are the measured and expected widths respectively of the Breit Wigner curve. $\Gamma_E$ values are taken from reference 24.

For mass combinations not including the neutral particle $\Delta M$ was about 2 6 MeV, both when the spectator was seen and when it was unseen.

For mass combinations including the neutral particle, $\Delta M$ was about 26 MeV when the spectator was seen, and about 54 MeV when the spectator was unseen. Figure 4.7 shows $Y_1^*(1385)$ production as an example. This loss of resolution is clearly rather serious. Also the peak of the $Y_1^*(1385)$ resonance in figure 4.7a occurs at about 1420 MeV, two standard deviations higher than expected. Smaller upward shifts were seen for other resonances; this is a strong indication of misfitting.

Results from a 3 GeV/c $K^-n$ experiment described in a thesis by W. Hoogland[50] confirmed that the mass resolution was worsened for one-constraint inserted spectator fits; but an order-of-magnitude calculation indicated that no shift in resonance peaks should occur. This is in contradiction to our results. The results of the $P_x$, $P_y$, $P_z$ method of fitting (method A), were compared with a fitting method using the conventional variables, with $^1/_p = 45 \pm 30$ MeV/c $^{-1}$, and dip and azimuth equal to zero with large errors (method B). For the one-constraint inserted spectator fits, method A gave results similar to those from this experiment; method B gave a better spectator momentum distribution, but worse anisotropy in the spectator angular distributions. Also the mass resolution was worsened, and a shift in the position of the resonance peaks was expected. Thus method B seemed to be even worse than method A.

These conclusions have been confirmed by our Glasgow collaborators, using artificial "events" generated by a Monte Carlo program[51]. They used method A, and also tried a method that used the fitted spectator parameters from method A and the measured parameters for other particles, to carry out a "second iteration" of method A; although this improved the spectator momentum distribution, which then peaked at 50 MeV/c, the strong angular anistropies were unchanged. The spread of centre of mass energy

was found to be too narrow, because the fitted spectator momentum was too small. Both this study, and Hoogland's agreed that although the misidentification of one-constraint inserted spectator fits was worse than for the corresponding seen spectator fits, it was not excessive (about 13% for one example in reference 51).

To summarize, four-constraint inserted spectator fits using the $P_x$, $P_y$, $P_z$ method show some advantages over the conventional one-constraint fits. However, one-constraint inserted spectator fits lead to biased and inaccurate results. Such fits have been used to calculate cross-sections, or for the study of processes exclusively involving the seen outgoing particles, but they were excluded from all other studies.

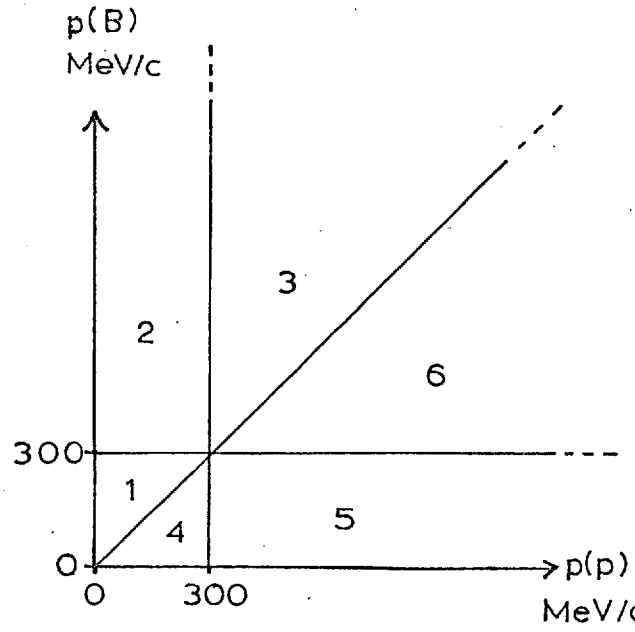


a) Definition of regions.

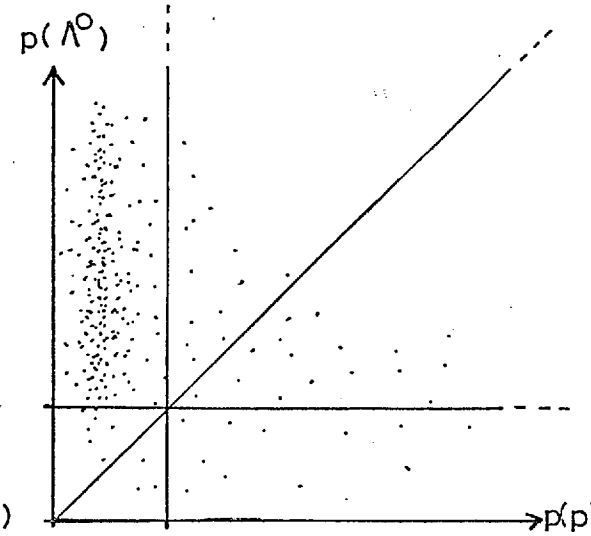


b) Channel 4.3; $\Lambda^{o}$ p $\pi^{-}$.

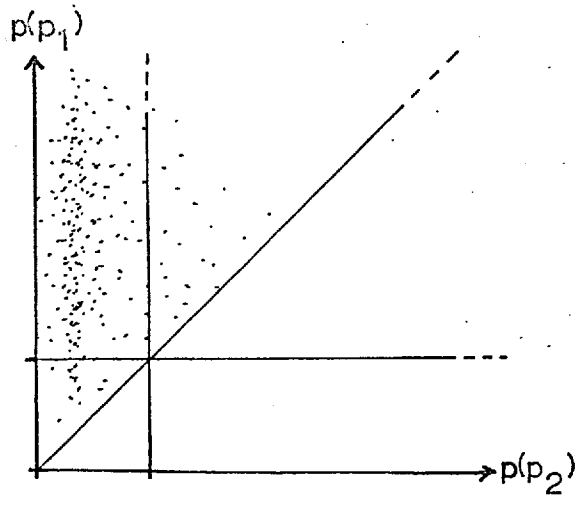


c) Channel 4.8; pp$K^{-}\pi^{-}$.
($p_1$ is selected to be the faster proton).

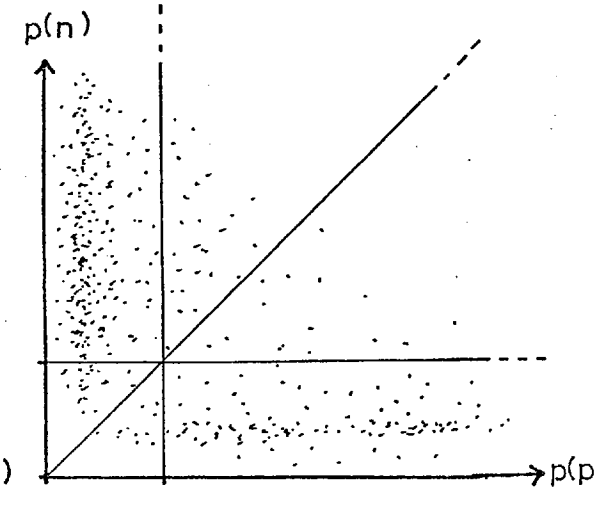


d) Channel 4.10; pn$\bar{K}^{o}\pi^{-}$.

FIGURE 4.1 SCATTER PLOTS OF PROTON VERSUS BARYON LAB. MOMENTA.

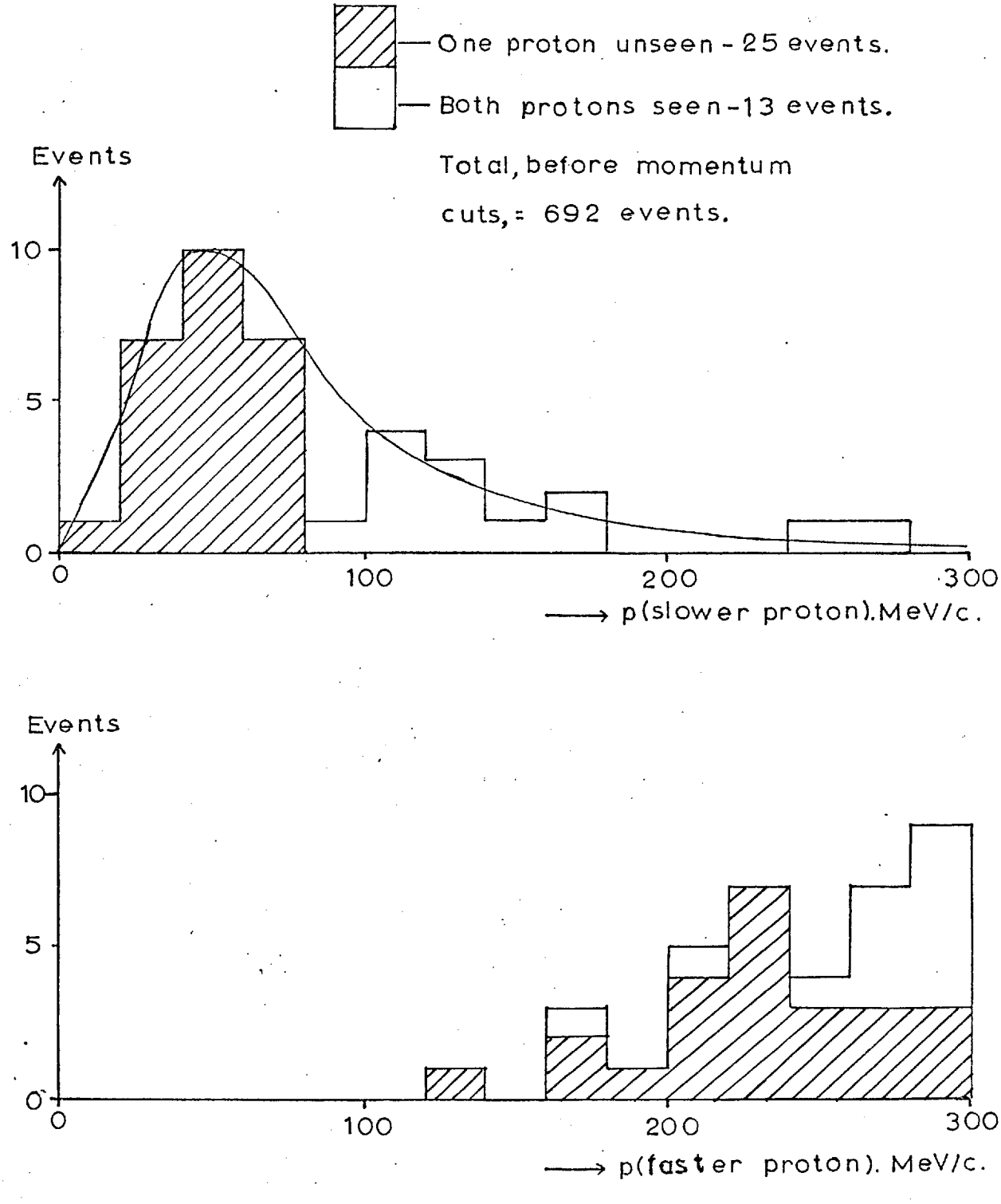


FIGURE 4.2 MOMENTUM SPECTRA FOR $ppK^-\pi^-$, WHEN BOTH PROTONS SLOWER THAN 300 MEV/C.

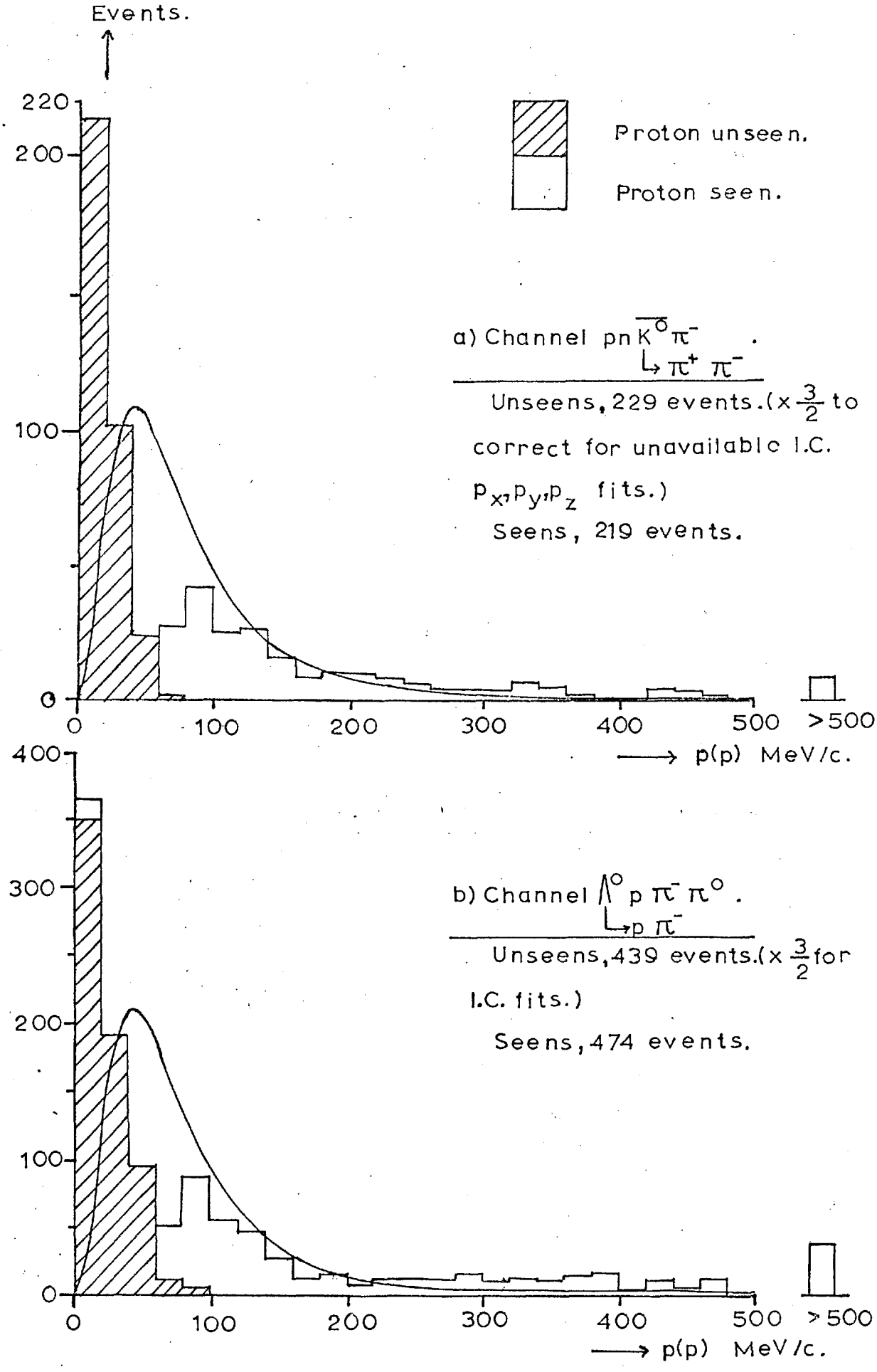


FIGURE 4.3 MOMENTUM DISTRIBUTIONS FOR PROTON.

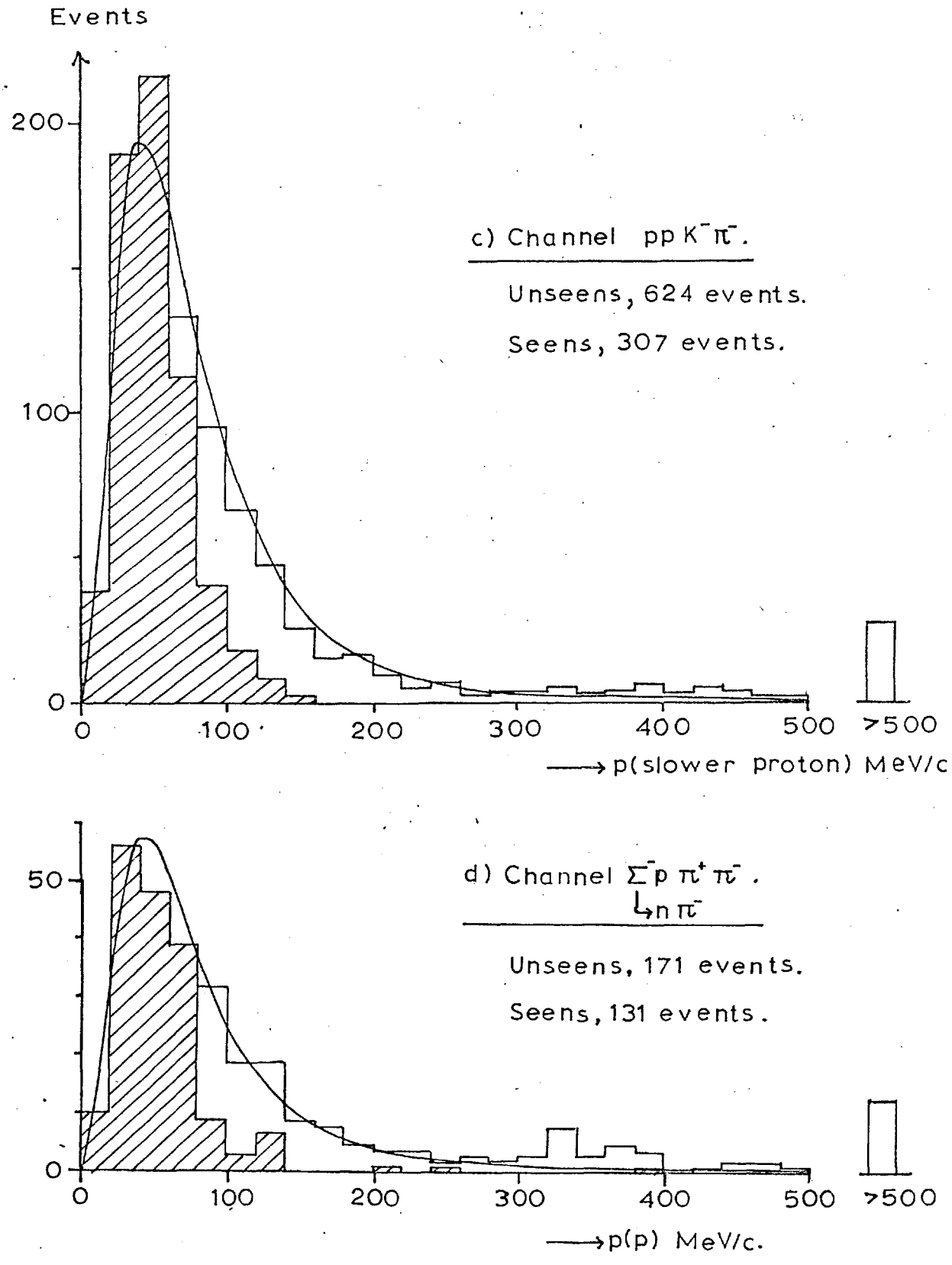


FIGURE 4.3 (continued).

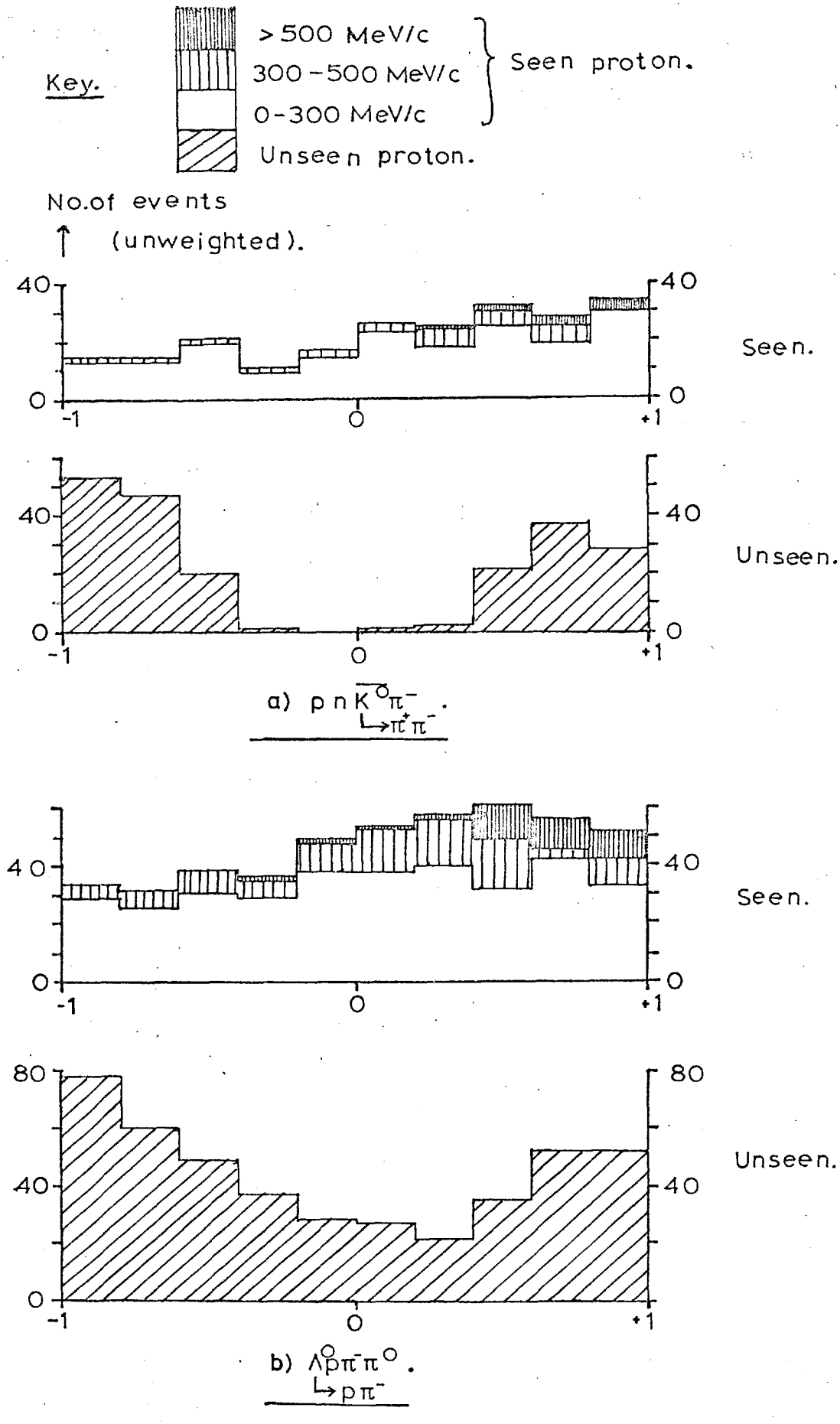


FIGURE 4.4 COS(Θ) FOR PROTON.

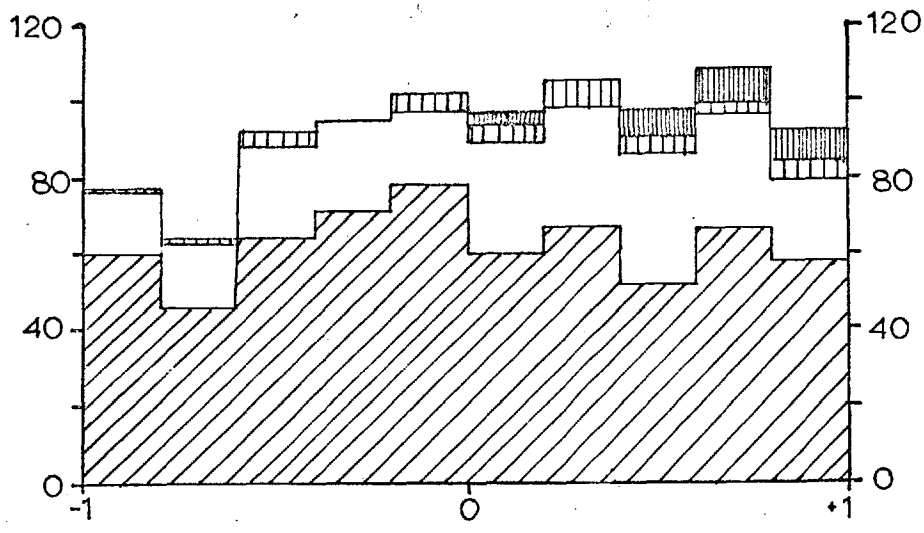


c) $pp K^-\pi^-$. (cosθ plotted for slower proton).

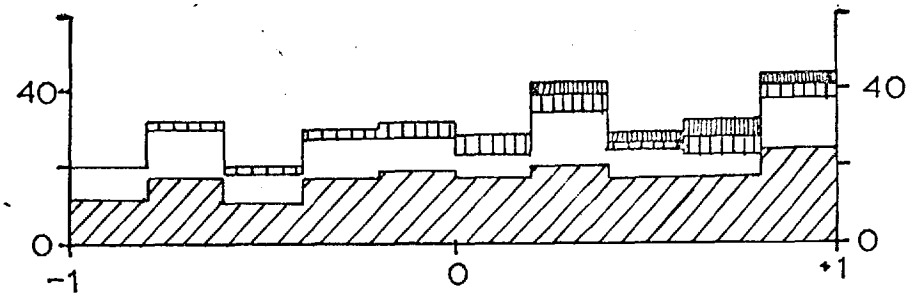


d) $\Sigma^-\bar{p}\pi^+\pi^-$ . $\hookrightarrow n\pi^-$

FIGURE 4.4 (continued).

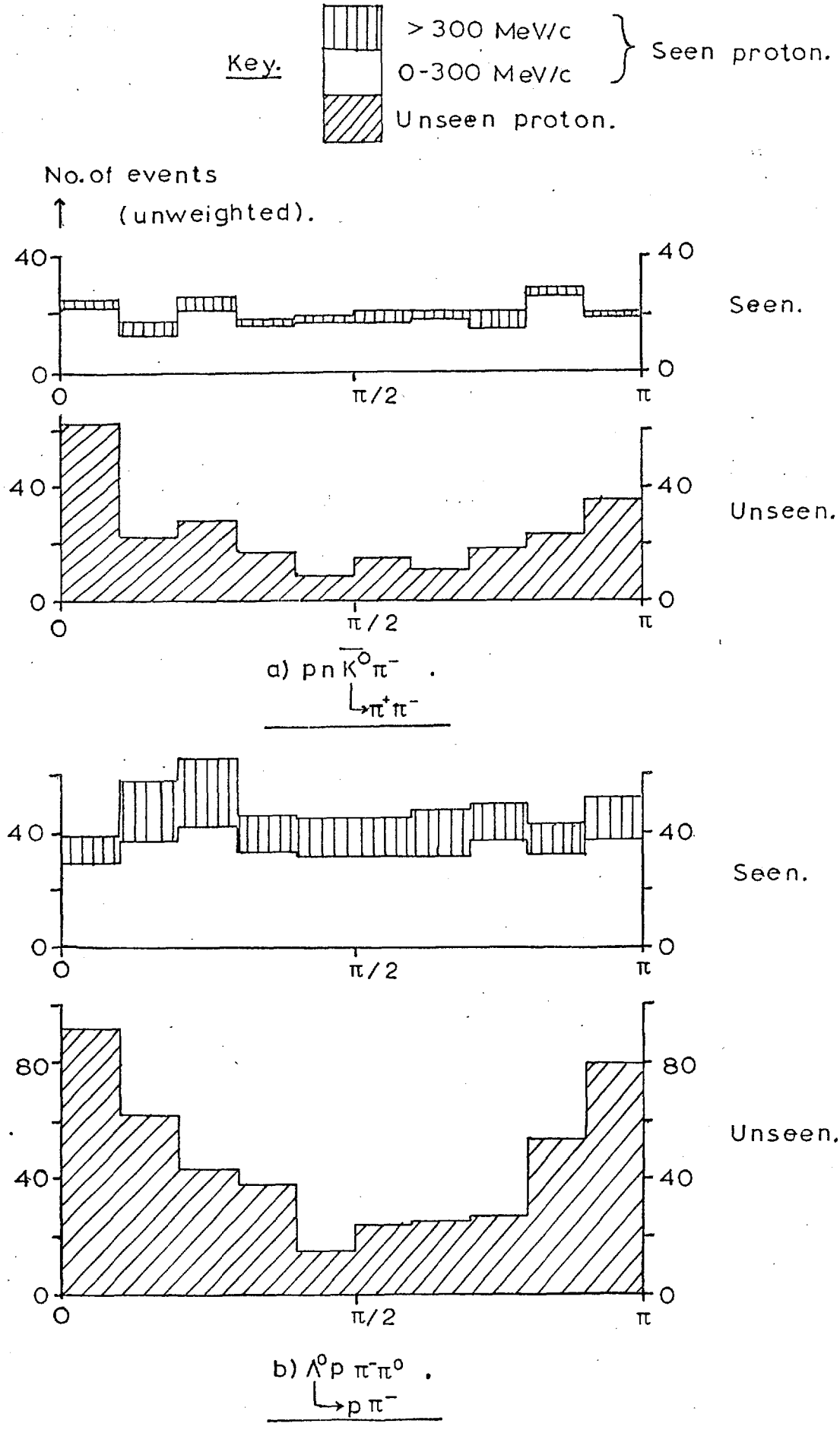


FIGURE 4.5 AZIMUTHAL ANGLE FOR PROTON.

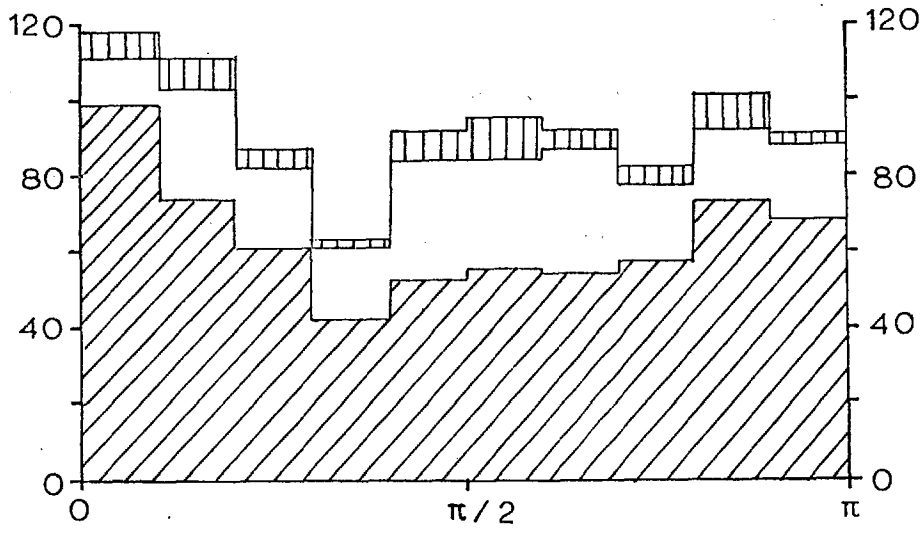


c) $pp K^- \pi^-$. (plotted for slower proton).

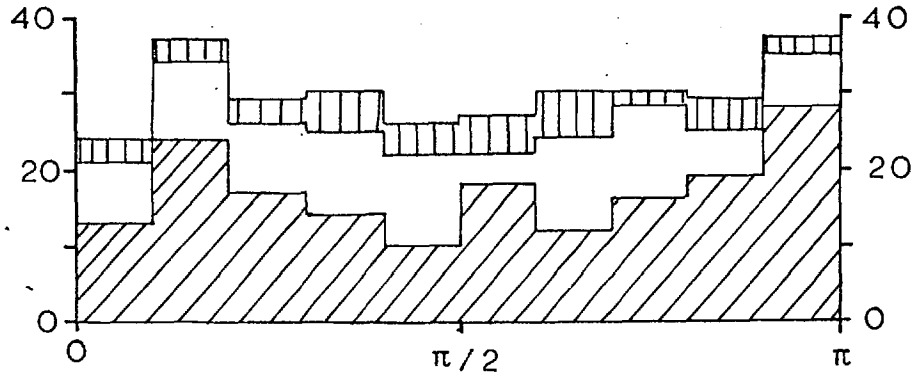


d) $\Sigma^- p \pi^+ \pi^-$ .
$\hookrightarrow n \pi^-$

FIGURE 4.5 (continued).

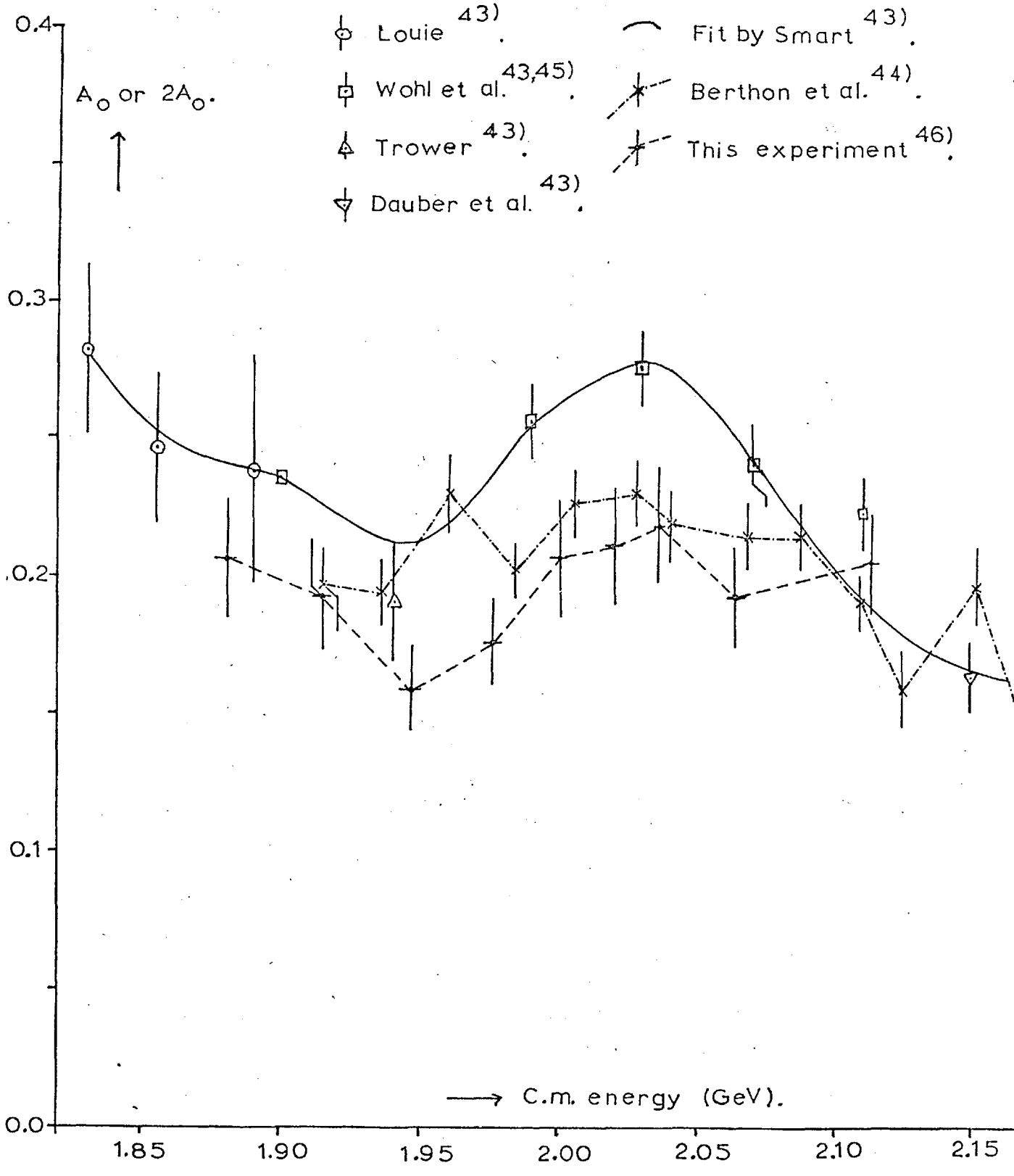


FIGURE 4.6 $A_o$ FOR $K^-n \to \Lambda\pi^-$, AND $2A_o$ FOR $K^-p \to \Lambda\pi^o$, VERSUS C.M. ENERGY.

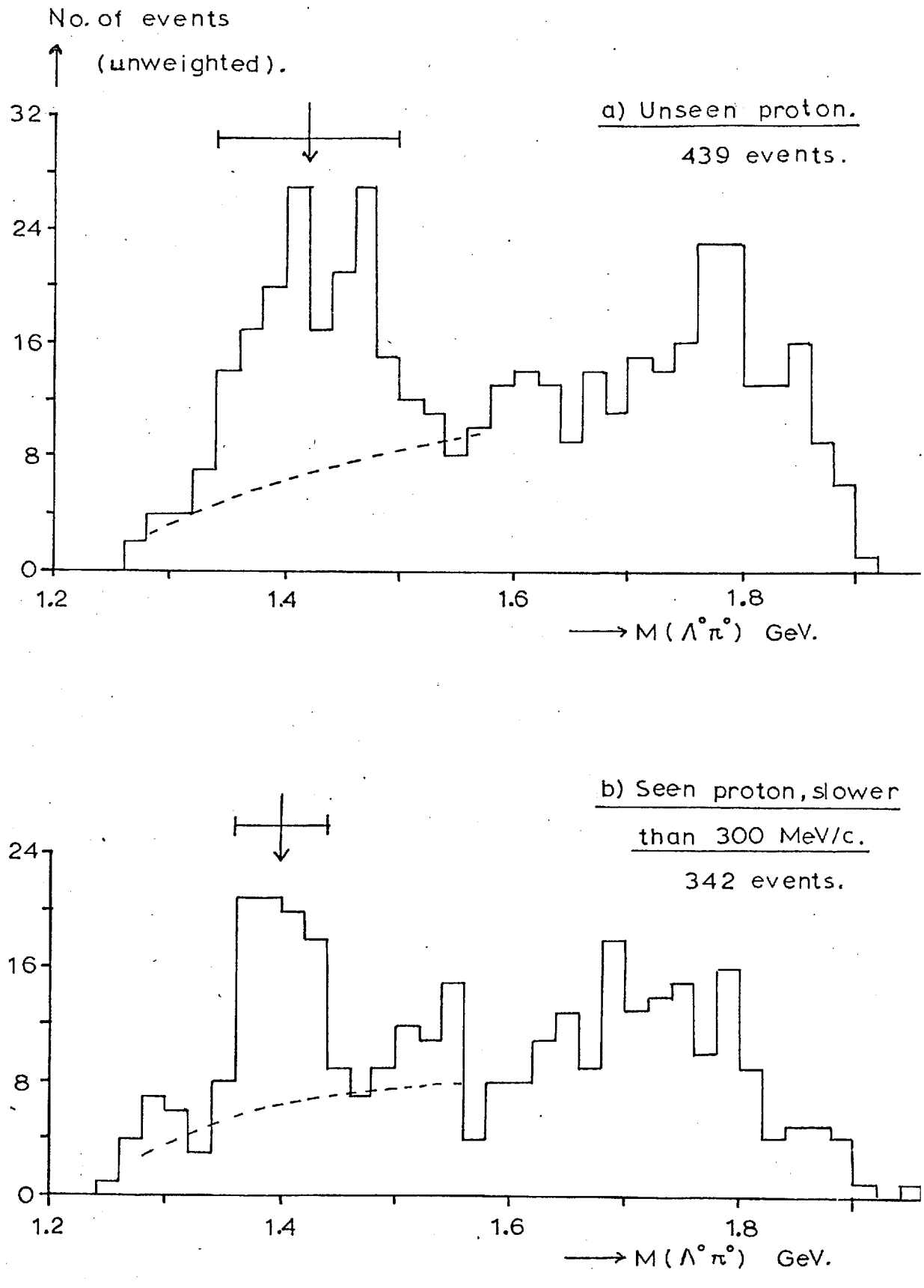


FIGURE 4.7 $\Lambda^\circ\pi^\circ$ EFFECTIVE MASS FOR $\Lambda^\circ p\pi^-\pi^\circ$. $\hookrightarrow p\pi^-$

## CHAPTER 5 Contamination and decay weighting.

### 5.1 Estimation of fraction of $\pi^-$ particles in the beam.

Two different methods were used. Firstly, events with the topology 400 were kinematically fitted to the following reactions:

$$\pi^- d \rightarrow \pi^- \pi^- pp \qquad (5.1$$

$$K^- d \rightarrow K^- \pi^- pp \qquad (5.2$$

Both reactions gave four-constraint fits (since both protons were seen), and were well separated; only about 6% of the events fitting 5.1 also fitted 5.2. The ratio of fits for each reaction was corrected for the cross-section difference; the factor, $\sigma(K^-) / \sigma(\pi^-)$, was 0.71.

For the second method, all delta rays on beam tracks leading to interactions were recorded. Since the momentum of all beam tracks that passed the scanning criteria was similar, $\pi^-$ particles had a larger value of $\beta (= v/c)$ than did $K^-$ particles, and could therefore create more energetic delta rays. It was found that at 1.65 GeV/c, delta rays of radius greater than 1.8 cms were nearly all produced by $\pi^-$ particles, with an efficiency of 3.1% for an average beam track length of 40 cms. The fraction of $\pi^-$ particles calculated was corrected for the difference of $\pi^- n$ and $K^- n$ total cross-sections. The ratio used was 0.80.

These two methods were used by all the collaborating groups on about one half of the pictures scanned and results from each agreed well. Also the results from different groups were compatible, except for one second run value that disagreed with all other determinations, and was therefore discarded. The averages figures are given in table 5.1.

Only the second run was seriously contaminated, and it was found that $\pi^-$ beam tracks from this run tended to enter the bubble chamber lower

Table 5.1 $\pi^-$ contamination.

| Run | Momentum (GeV/c) | $(N_{\pi^-}) / (N_{K^-})$ at bubble chamber. (%) |
|---|---|---|
| 1 | 1.65 | $2.7 \pm 0.7$ |
| 2 | 1.65 | $13.3 \pm 3.0$ |
| 4 | 1.65 | $1.5 \pm 0.6$ |
| 1+2+4 | 1.65 | $4.3 \pm 0.8$ |
| 3 | 1.45 | $1.0 \pm 1.0$ |

than $K^-$'s, i.e. with a smaller y coordinate. 60% of $\pi^-$ beam tracks could be rejected. But the final contamination of all 1.65 GeV/c data (runs 1, 2 and 4) would only be reduced by 1% as a result, and so no action was taken.

Of the channels discussed in later chapters, only channel 5.2 is affected by $\pi^-$ contamination. The fraction of possible $\pi^-$-induced events that fitted 5.2 as well as 5.1 varied with the degree of constraint of the fit; it was 6% for a four-constraint fit when both protons were seen, 60% for a one-constraint unseen spectator fit, and probably about 40% for a four-constraint unseen spectator fit using the Px, Py, Pz variables. The calculated contaminations, corrected for cross-section differences, were 2% and 0.5% for the 1.65 GeV/c and 1.45 GeV/c data respectively.

## 5.2 Contamination of all three-body channels.

### 5.2.1 Introduction.

The contamination from misidentification of $K^-$-induced events as well as from $\pi^-$-induced events is examined; in fact the latter only matters for the 300 and 400 channels. The following channels are considered; each involves a proton spectator, satisfying the criteria of chapter 4.

$$K^- n \rightarrow \Lambda^0 \pi^- \pi^0 \quad (\Lambda^0 \rightarrow p\pi^-) \qquad (5.3$$

$$K^- n \rightarrow n K^0 \pi^- \quad (K^0 \rightarrow \pi^+ \pi^-) \qquad (5.4$$

$$K^- n \rightarrow p K^- \pi^- \qquad (5.5$$

$$K^- n \rightarrow \Sigma^- \pi^- \pi^+ \quad (\Sigma^- \rightarrow n\pi^-) \qquad (5.6$$

$$K^- n \rightarrow \Sigma^+ \pi^- \pi^- \quad (\Sigma^+ \rightarrow p\pi^0) \qquad (5.7$$

$$K^- n \rightarrow \Sigma^+ \pi^- \pi^- \quad (\Sigma^+ \rightarrow n\pi^+) \qquad (5.8$$

All channels were fitted by the $p_x$, $p_y$, $p_z$ method when the spectator was unseen, except for one half of the Imperial College events for channels 5.5 to 5.8 from the 1.65 GeV/c run. Therefore channels 5.5 to 5.8 gave four-constraint fits nearly always. These latter channels were the most heavily contaminated, by $K^-$-induced events from other channels. The discussion in chapter 4 shows that, for events in these channels with an unseen spectator, the event identification was fairly reliable, although the kinematic track parameters were seriously biased. Such events are used for cross-section calculations, and so must be discussed here.

In general the 1.65 GeV/c data had larger contamination that the 1.45 GeV/c data, because for the former, momentum errors were slightly larger and hence misidentification was easier.

### 5.2.2 Quantities plotted.

To investigate contamination and losses for the above decays, histograms of the two decay angles were plotted:

$$\cos \vartheta_d(e) = \hat{\underline{D}}p . \hat{\underline{e}}_d \qquad (5.9$$

$$\varphi_{1z} = \cos^{-1}\left[\frac{(\hat{\underline{D}}_1 \times \hat{\underline{z}})\ (\hat{\underline{D}}_1 \times \hat{\underline{e}}_1)}{|\hat{\underline{D}}_1 \times \hat{\underline{z}}|\ |\hat{\underline{D}}_1 \times \hat{\underline{e}}_1|}\right] \qquad (5.10$$

The $\hat{}$ on vectors indicates unit length. D, e and z represent the decay parent, the selected decay product, and the bubble chamber z axis respectively. The first subscript specifies the reference system, l is the laboratory system, p the production centre of mass system, and d the decay c.m. system.

Cos $\vartheta_d$ should have a flat distribution for all charged or neutral decays from 2 or 3 body channels, since the polarisation of any decaying particle must be normal to $\hat{D}p$, by parity conservation.

Also the distribution of $\varphi_{lz}$ should be flat, since any polarisation of the decay parent is randomly orientated relative to the z axis. However, scanning losses may occur when the decay plane contains the z axis, i.e. at $\varphi_{lz} = 0$ or $\pi$.

Histograms were also examined for true decay lifetime, projected decay length, coordinates of production and decay vertices and (missing mass)$^2$, which is defined thus:

$$(\text{missing mass})^2 = (E_{in} - \Sigma E_{out})^2 - (\underline{p}_{in} - \Sigma \underline{p}_{out})^2 \qquad (5.11$$

The summation is carried out over seen outgoing particles; unfitted directions and momenta must be used. For example in channel 5.5, the (m.m.)$^2$ should be zero, and in channel 5.3, it should equal $(m(\pi^0))^2$.

5.2.3 $\bar{K}^- n \rightarrow \Lambda^0 \pi^- \pi^0$ , $\Lambda^0 \rightarrow p\pi^-$ (channel 5.3).

This channel suffers the worst contamination, and is discussed in some detail because of its importance in the later analysis.

The identification of the $\Lambda^0$ was very reliable. About 1% of the decay vertex $\Lambda^0$ fits were ambiguous with $\bar{K}^0$ fits, and half of these gave multivertex fits to 5.4, as well as to 5.3, and were excluded from 5.3 for convenience. Fits to $\gamma \rightarrow e^+ e^-$ were unfortunately not attempted. A $\bar{K}^0$ decay

or $\gamma$ conversion could emulate a $\Lambda^o$ decay where the proton travelled forward in the $\Lambda^o$ c.m., that is, with $\cos\theta_d = +1$. The histograms of $\cos\theta_d$ for unique fits showed a very small excess here, certainly less than 1% for both beam momenta. A study of $\varphi_{1z}$ histograms indicated that scanning losses were also less than 1%.

Once the $\Lambda^o$ had been identified, there were still four possible contaminating channels, numbers 5.12 to 5.15, given in table 5.2. The last two channels were unfittable, and their cross-sections were estimated from fittable channels involving different charge states of the same particles. Isospin Clebsch-Gordan coefficients were used to calculate resonant cross-sections, and the non-resonant cross-sections were assumed to be equal to those for the fittable reactions. For example the non-resonant cross-sections for the $\Sigma^+\pi^-\pi^-$ and $\Sigma^-\pi^+\pi^-$ channels were .07 and .08 mb respectively at 1.65 GeV/c, and so .075 mb was taken for this part of channel 5.14.

Channel 5.12 was always preferred to 5.3, as it was more highly constrained. For channel 5.12 the $(\text{m.m.})^2$ distribution was very narrow, and

Table 5.2 Channels possibly contaminating $K^-n \to \Lambda^o\pi^-\pi^o$, $\Lambda^o \to p\pi^-$.

| Channel | No. of constraints | Cross-sections (mb) | | Reference number |
|---|---|---|---|---|
| | | At 1.45 GeV/c | At 1.65 GeV/c | |
| $K^-n \to \Lambda^o\pi^-$ | 4 | 2.8 | 2.0 | 5.12 |
| $K^-n \to \Sigma^o\pi^-$, $\Sigma^o \to \Lambda^o\gamma$ | 1 | 0.80 | 0.45 | 5.13 |
| $K^-n \to \Sigma^o\pi^-\pi^o$, $\Sigma^o \to \Lambda^o\gamma$ | -2 | ~0.6 | ~0.6 | 5.14 |
| $K^-n \to \Lambda^o\pi^-\pi^o\pi^o$ | -2 | ~0.6 | ~0.6 | 5.15 |

also the missing energy was closer to zero, whereas the missing energy for 5.3. was usually large. Thus the two channels were kinematically well separated, and losses from 5.3 should be negligible.

About 4% of seen spectator events and 6% of unseen spectator events for channel 5.3 were ambiguous with 5.13. Histograms of $\cos\theta_d$ for the $\Sigma^o$ decay for these events were not flat, but had an excess of forward $\gamma$'s, (figure 5.1). This excess was probably caused by true 5.3 events with a fast $\pi^o$ that could simulate a fast forward $\gamma$ , and thus also fitted 5.13. Figure 5.2 shows $\cos\theta_d$ for the complementary situation of $\Lambda^o/\Sigma^o$ ambiguities; section 6.2 discusses this. On this basis, about one-third of the ambiguous events really came from channel 5.3, and thus, rejecting ambiguous events lost only about 2% of good 5.3 events.

The contamination from channels 5.14 and 5.15 is best investigated from histograms of $(\text{missing mass})^2$ for channel 5.3; see figure 5.3 for 1.45 GeV/c results. The minimum values of $(\text{m.m.})^2$ are about $m^2(\pi^o)$ for the $\pi^o\gamma$ from 5.14 and $4m^2(\pi^o)$ for 5.15. Thus we expect 5.14 to be a larger source of contamination; unfortunately these events will not all cause an excess number of events on the high mass side of the $(\text{m.m.})^2$ peak, since measurement errors can produce some events with $(\text{m.m})^2$ less than $m^2(\pi^o)$ which tend to cancel the excess caused by the other events. Figure 5.4 shows the distributions of excess events. We assumed that half the 5.14 events did not appear in the excess, and also that the contaminations from 5.15 events was half that from 5.14 events; the results are shown in table 5.3. If all events with $(\text{m.m.})^2$ greater than 0.7 GeV$^2$ were removed, this reduced contamination considerably without losing too many genuine events; see table 5.3.

After having rejected all ambiguous events, and those with $(\text{m.m})^2$ greater than .07 GeV$^2$, the remaining contamination and losses are shown in

Table 5.3 Contamination of channel 5.3 by channels 5.14 and 5.15.

| Events | Fraction of true | | Total (%) | Total after cut (%) | True 5.3 removed by cut (%). |
|---|---|---|---|---|---|
| | 5.14 (%) | 5.15 (%) | | | |
| 1.45 GeV/c seen spectators. | 4.7 | 2.3 | 7.0 | 4.9 | 3.3 |
| 1.45 GeV/c unseen spectators. | 6.5 | 3.2 | 9.7 | 4.7 | 7.0 |
| 1.65 GeV/c seen spectators. | 8.0 | 4.0 | 12.0 | 7.0 | 5.0 |
| 1.65 GeV/c unseen spectators. | 13.0 | 6.5 | 19.5 | 9.3 | 7.9 |

table 5.4. All estimates are subject to errors of about one-half, because of statistical fluctuations and because of the assumptions made. Only the seen spectator events were used for physics plots, and thus the remaining biases should not be too serious.

### 5.2.4 $K^- n \to n\bar{K}^0 \pi^-$ (channel 5.4).

$$\hookrightarrow \pi^+\pi^-$$

The numbers of ambiguous fits, mainly involving channel 5.3 only, were less than 1% at both momenta. These were, therefore, not used.

Table 5.4 Contamination and losses for channel 5.3, from all sources.

| | Contamination from 5.14 and 5.15 (%) | Losses to 5.13, 5.14 and 5.15 (%) |
|---|---|---|
| 1.45 GeV/c seens | 4.9 | 5.5 |
| 1.45 GeV/c unseens | 4.7 | 8.6 |
| 1.65 GeV/c seens | 7.0 | 7.0 |
| 1.65 GeV/c unseens | 9.3 | 10.3 |

The histograms of $\cos\vartheta_d(\pi^-)$ for the $\bar{K}^o$ decay showed a significant excess (for unique events) at $\cos\vartheta_d = -1$, of 2% and 4% at 1.45 and 1.65 GeV/c respectively; see figure 5.5. This probably came from misfitting of true $\Lambda^o$ decays from channels 5.14 or 5.15; misfitted $\gamma$ decays from the $\Sigma^o$ channels would cause excesses at -1 and +1. The $\varphi_{1z}$ histograms showed no losses.

When the $\bar{K}^o$ had been identified, the only possible contamination was from:

$$K^-n \rightarrow n \begin{matrix} \bar{K}^o\pi^-\pi^o \\ \lfloor_{\pi^+\pi^-} \end{matrix} \qquad (5.16$$

This channel was unfittable. However, the width of the $(\text{m.m.})^2$ neutron peak for 5.4 was about one-fifth of the separation of the neutron and $(n + \pi^o)$ peaks (figure 5.6), so very little misfitting should occur. By calculating the excess on the high mass side of the neutron peak, as done for channel 5.3, the contamination was found to be less than 0.5% and 3.0% for all events with seen and unseen spectators respectively.

It should be noted that the peak of the $(\text{m.m.})^2$ histogram at 1.45 GeV/c was at .875 $(\text{GeV})^2$, that is, .005 $(\text{GeV})^2$ lower than expected. Channel 5.13 showed a similar effect. This was probably caused by underestimation of the beam momentum by about 4 MeV/c, but should affect the overall quality of fitting only a little.

Thus there are no serious contamination problems for this channel.

### 5.2.5 $K^-n \rightarrow pK^-\pi^-$ (channel 5.5).

The possible sources of contamination were:

$$\pi^-n \rightarrow p\pi^-\pi^- \qquad (5.17$$

$$K^-n \rightarrow pK^-\pi^-\pi^o \qquad (5.18$$

Confusion of $K^-$ with $\pi^-$.

The $\pi^-$ contamination has been discussed in section 5.1 and was not serious. Channel 5.5 was always preferred to 5.18 as it was more highly constrained; these channels are kinematically well-separated, for the same reasons stated for channels 5.3 and 5.12, and thus contamination of 5.5 was negligible. Figure 5.7 shows the $(\text{m.m.})^2$ plots for all four-constraint fits, i.e. seen spectator events and unseen spectator events fitted using the $p_x$, $p_y$, $p_z$ method. Figure 5.8 shows the plot for all Imperial College one-constraint unseen spectator fits, which has a wider peak, with an excess of high $(\text{m.m.})^2$ events. Thus the use of the $p_x$, $p_y$, $p_z$ method leads to an important improvement here. But the one-constraint fits were only 10% of all fits to this channel for the 1.65 GeV/c run, and were not used for the 1.45 GeV/c run, and so the final contamination was small.

When fits to 5.5 with $\pi^-$ and $K^-$ particles interchanged were ambiguous, the fit with lower probability was rejected, but this occurred for less than 5% of all fits. Table 5.5 summarizes the situation.

### 5.2.6 $K^-n \to \Sigma^{\mp}\pi^-\pi^{\pm}$ (channels 5.6, 7, and 8).

Ambiguities with $K^{\mp}$ decays were largely eliminated by use of criterion 5 in section 3.4.3; only about 0.5% of all fits to these channels remain ambiguous. The reliability of this criterion seemed very good, as discussed in sections 3.4.4.

Table 5.5 Contamination of $K^-n \to pK^-\pi^-$.

| | From 5.17 (%) | From 5.18 (%) | From $\pi^-/K^-$ confusion. (%) | Total (%) |
|---|---|---|---|---|
| 1.45 GeV/c run | 0.5 | ~0.2 | ~2. | 2.7 |
| 1.65 GeV/c run | 2.0 | 1.5 | ~2. | 5.5 |

Other contamination could come from $K^- n \rightarrow \Sigma^{\mp} \pi^- \pi^{\pm} \pi^0$ events. However, the corresponding channels were kinematically well separated, just as channels 5.3 and 5.12 were. The total contamination was less than 3%, which was not serious.

However, both the cos$\vartheta$d and $\varphi_{lz}$ histograms were anistropic because of scanning losses. This was worst for channel 5.7, that is, for $\Sigma^+ \rightarrow p\pi^0$. These losses were corrected by a weighting method discussed in the next section.

## 5.3 Weighting for unseen weak decays.

### 5.3.1 Introduction.

Some charged and neutral decays (e.g. of $\Sigma^+ \rightarrow p\pi^0$ or of $\Lambda^0 \rightarrow p\pi^-$) occur outside the bubble chamber, or too close to the collision vertex to be distinguished. Also certain configurations may be very difficult to see when scanning. All of these losses are dependent on the momentum of the parent particle, and must therefore, be corrected for, in order to avoid biases, and in order to compute cross-sections.

To correct for the first kind of loss, a minimum observable projected decay length ($l_{min}$) and a maximum observable decay volume were chosen. Then all events with decays outside these limits were rejected, and the remaining events were weighted thus:

$$\text{Weight} = \frac{1}{\exp(-t_{min}/T) - \exp(-t_{max}/T)} \qquad (5.19$$

Where $T$ = average true lifetime

$$t_{min} = \frac{m.l_{min}}{p.\sin(dip)} \qquad (5.20$$

$$t_{max} = \frac{m.l_{max}}{p} \qquad (5.21$$

$l_{max}$ = distance from collision vertex to edge of decay volume, along decay parent direction. (5.22

To select $l_{min}$, histograms of the projected decay length were plotted, and for most channels a loss of events was seen for l less than about 5 mm. Then plots were made of the total weighted number of events ($N_w$) versus the value of $l_{min}$ selected. For $l_{min}$ less than 3 mm, the scanning losses were not completely corrected for, and $N_w$ was too small; as $l_{min}$ was increased, $N_w$ increased, and then flattened off. The optimum $l_{min}$ was at the turnover point. To help locate this point, error bars were drawn showing the expected fluctuation of one $N_w$ relative to the previous one. The expression 5.23 is corrected for the use of weighted events.

$$\sigma(N_{w2}-N_{w1}) = \sqrt{(N_{01}-N_{02})}\cdot\frac{N_{w2}}{N_{02}} \qquad (5.23$$

($N_0$ = unweighted number of events.)

Figure 5.9 shows the $N_w$ plots for three important cases, and table 5.6 summarizes all the $l_{min}$ values used.

The production and decay fiducial volumes used are shown in figure 5.10 and table 5.7. The production volume was chosen during scanning, to be a rectangular area on the pictures from the second camera; in three dimensions this becomes a box with sloping sides. The z limits of the production volume

Table 5.6 Values of $l_{min}$ selected.

| Decay | $l_{min}$ (cms) | |
|---|---|---|
| | 1.45 GeV/c events | 1.65 GeV/c events |
| $K^o_s \rightarrow \pi^+\pi^-$ | 0.3 | 0.3 |
| $\Lambda^o \rightarrow p\pi^-$ | 0.3 | 0.3 |
| $\Sigma^- \rightarrow n\pi^-$ | 0.4 | 0.5 |
| $\Sigma^+ \rightarrow p\pi^o$ | 0.9 | 0.5 |
| $\Sigma^+ \rightarrow n\pi^+$ | 0.4 | 0.5 |

Table 5.7 Dimensions of production and decay fiducial volumes.

| | | x (cms.) | y (cms.) | z (cms.) |
|---|---|---|---|---|
| Production volume | at back glass. | -20.9 → 22.6 | -13.7 → 13.7 | ~ 0. |
| | at front glass. | -20.9 → 13.0 | -10.7 → 10.7 | → 50. |
| | at mid-point. | -20.9 → 17.8 | -12.2 → 12.2 | |
| Decay volume. | | -21.0 → 30.0 | -17.0 → 17.0 | 15. → 37. |

depended on the spread in beam z position, and were found from histograms. The decay fiducial volume was also decided from histograms; it should not include any region where decays would not be measurable, and should be at least one decay length away from the production fiducial volume, for the decays with longest lifetimes ($\Lambda^o$'s, for this experiment). The latter requirement avoids over-large decay weights that can cause large statistical fluctuations in weighted histograms. In fact optimum conditions could not be achieved; for example, the decay of a fast $\Lambda^o$ particle travelling sideways from a collision near the edge of the fiducial volume, had a potential decay length of 5 cms., equivalent to half a lifetime, and would receive a weight of about 2.8. However, such a combination of circumstances was uncommon; about 3% of $K^o_s$ and $\Lambda^o$ decays received weights greater than 1.5.

The average decay weights for neutral decays are given in table 5.8.

### 5.3.2 Small-angle decay losses for $\Sigma^\pm$ decays.

The scanning loss of small-angle $\Sigma$ decays is dependent on the

Table 5.8 Average decay weights for neutral decays.

| Decay | Channel | 1.45 GeV/c data | 1.65 GeV/c data |
|---|---|---|---|
| $K^o_s \rightarrow \pi^+\pi^-$ | $K^-n \rightarrow n\bar{K}^o\pi^-$ | 1.14 | 1.13 |
| $\Lambda^o \rightarrow p\pi^-$ | $K^-n \rightarrow \Lambda^o\pi^o\pi^-$ | 1.11 | 1.12 |

$\Sigma$ momentum. A previous experiment[28] in the CERN 81 cm bubble chamber which has similar geometry to that used here, essentially found that observed events should be weighted thus:

$$\text{Weight} = \frac{1}{1-\alpha p} \qquad (5.2.4$$

where p is the $\Sigma$ momentum in GeV/c, and $\alpha$ = .06 for $\Sigma^{\pm} \longrightarrow n\,\pi^{\pm}$ and = .30 for $\Sigma^{+} \longrightarrow p\,\pi^{o}$. Figure 5.11 shows the variation of efficiency (=1/weight) with $\Sigma$ momentum.

The best verification of this method is to compare the final weighted number for the two $\Sigma^{+}$ decay modes, which should be equal. Table 5.9 shows that the two decay modes agreed within one standard deviation. Table 5.9 also shows a very high average weight for the $\Sigma^{+} \longrightarrow p\,\pi^{o}$ decay mode for the 1.45 GeV/c data. This caused rather large fluctuations in histograms for channel 5.7, which involved this decay; however, this was the only $\Sigma^{\pm}$ decay that could be used to obtain $\Sigma$ polarization.

Table 5.9 Event totals and average weights for $\Sigma^{\pm}$ decays (Channels 5.6 to 5.8, I.C. data).

| Decay | | Unweighted No. | Weighted No. | Length weight | Angle weight | Total weight |
|---|---|---|---|---|---|---|
| 1.45 GeV/c | $\Sigma^{-} \to n\pi^{-}$ | 1185 | 1446.2 | 1.15 | 1.06 | 1.22 |
| | $\Sigma^{+} \to n\pi^{+}$ | 598 | 823.4 | 1.30 | 1.06 | 1.38 |
| | $\Sigma^{+} \to p\pi^{o}$ | 355 | 895.3 | 1.84 | 1.37 | 2.52 |
| | | | $\Delta = -72 \pm 58$ | | | |
| 1.65 GeV/c | $\Sigma^{-} \to n\pi^{-}$ | 712 | 896.0 | 1.17 | 1.08 | 1.26 |
| | $\Sigma^{+} \to n\pi^{+}$ | 280 | 406.1 | 1.38 | 1.05 | 1.45 |
| | $\Sigma^{+} \to p\pi^{o}$ | 216 | 424.6 | 1.41 | 1.39 | 1.96 |
| | | | $\Delta = -18 \pm 38$ | | | |

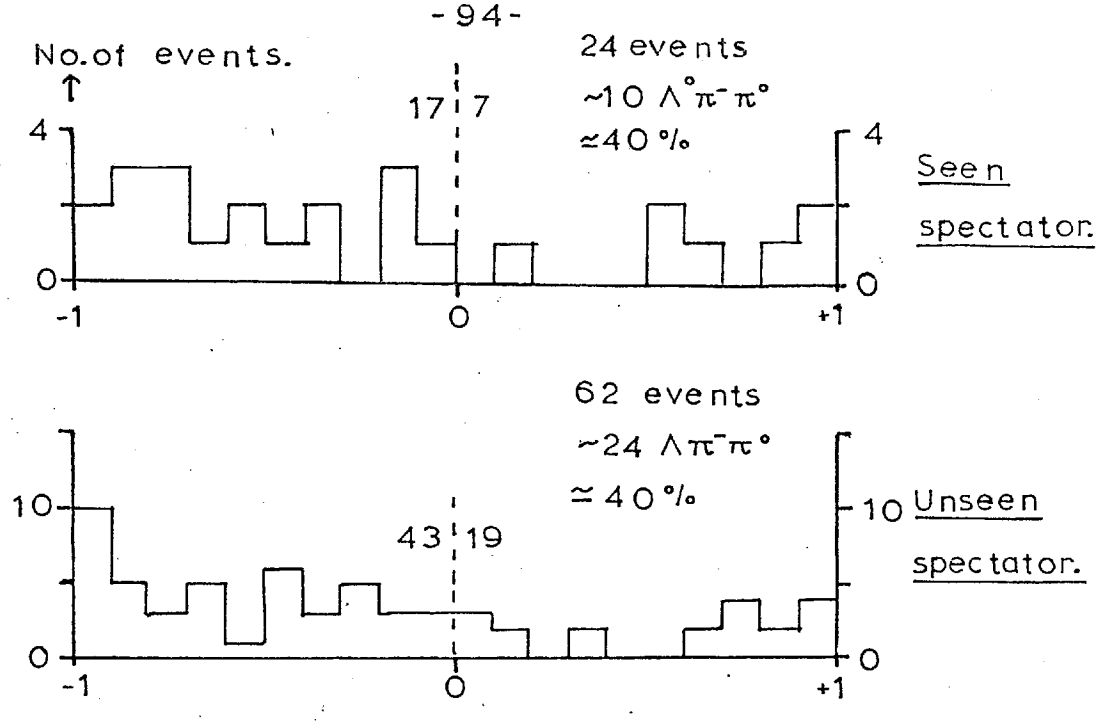


FIGURE 5.1 COS $\Theta_d$(Λ°) FOR $\Sigma^\circ\pi^-/\Lambda^\circ\pi^-\pi^\circ$ EVENTS AT 1.65 GEV/C.

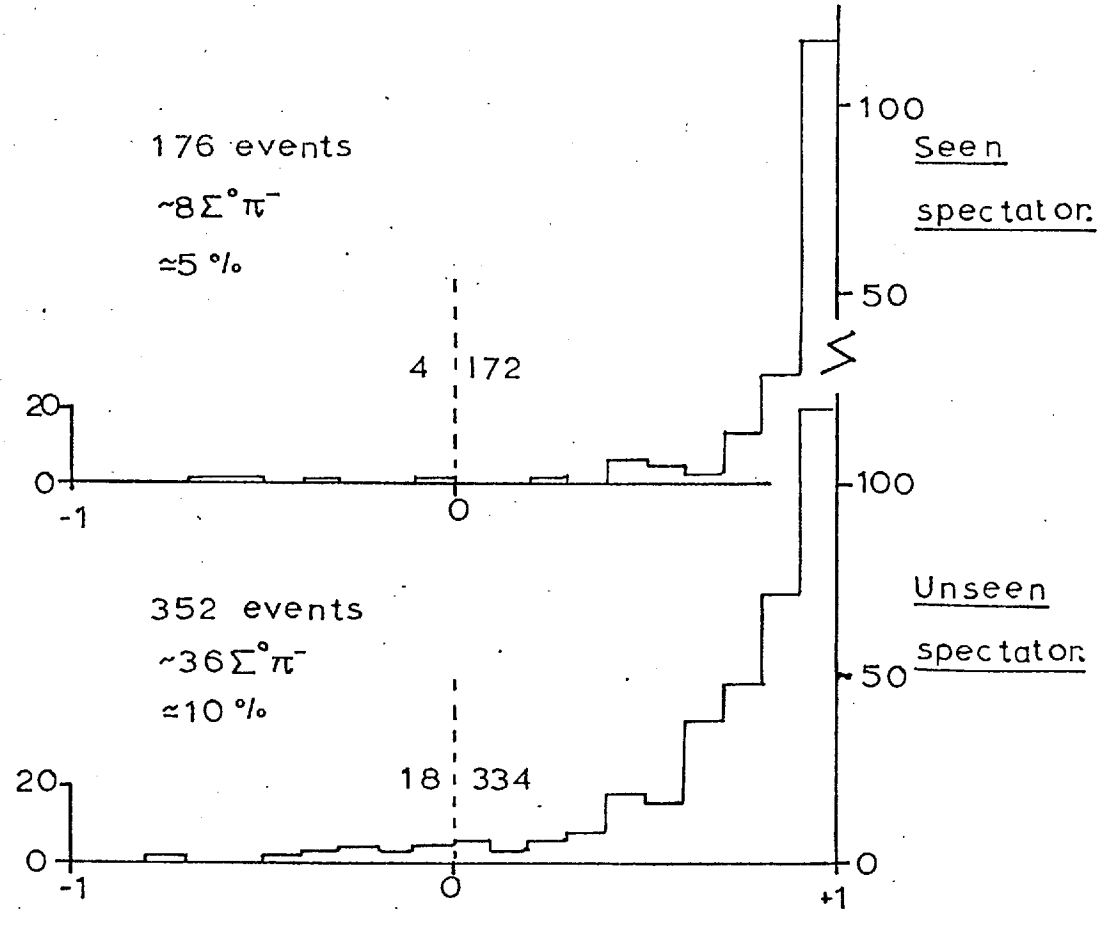


FIGURE 5.2 COS $\Theta_d$(Λ°) FOR $\Sigma^\circ\pi^-/\Lambda^\circ\pi^-$ EVENTS AT 1.65 GEV/C.

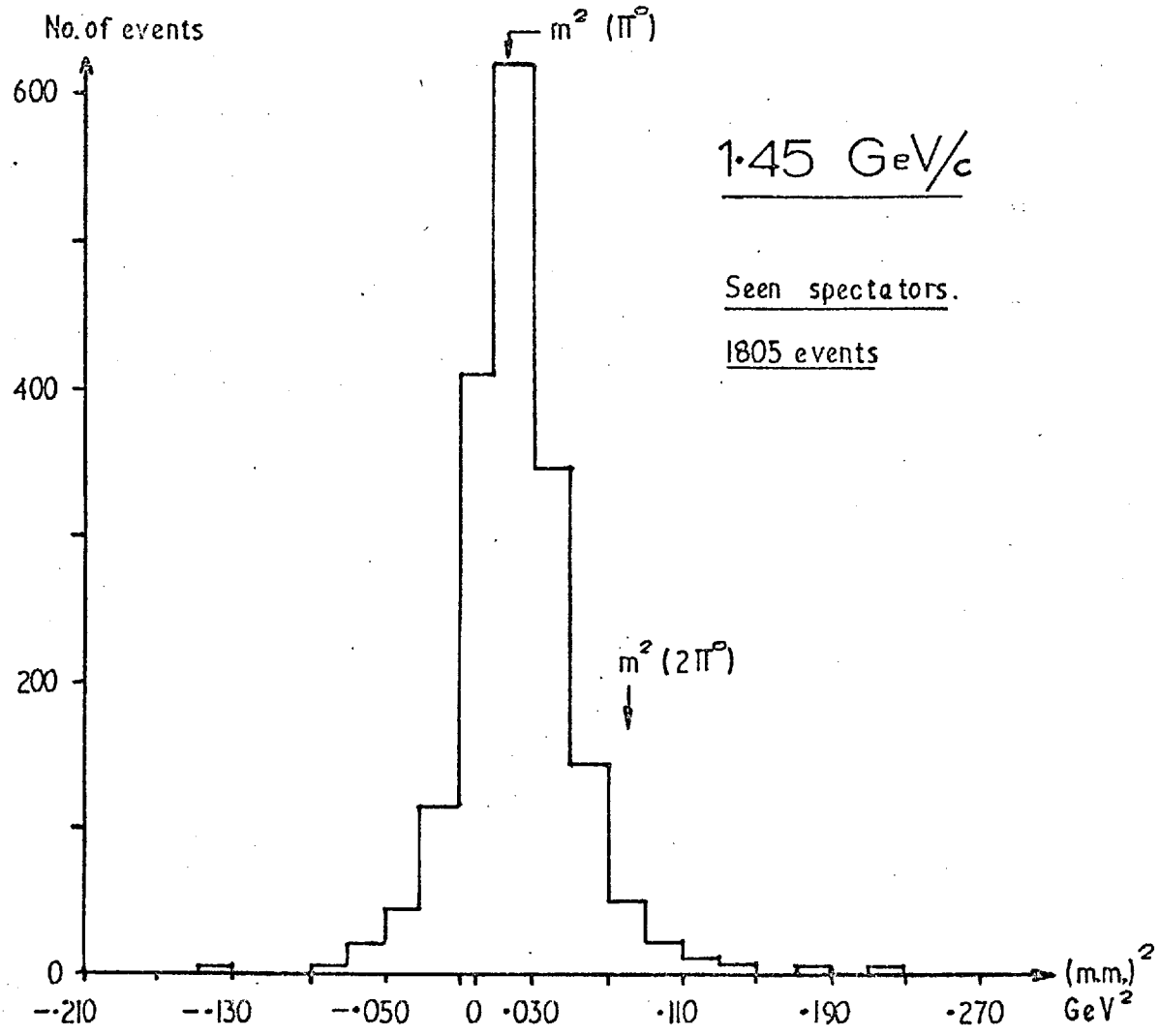


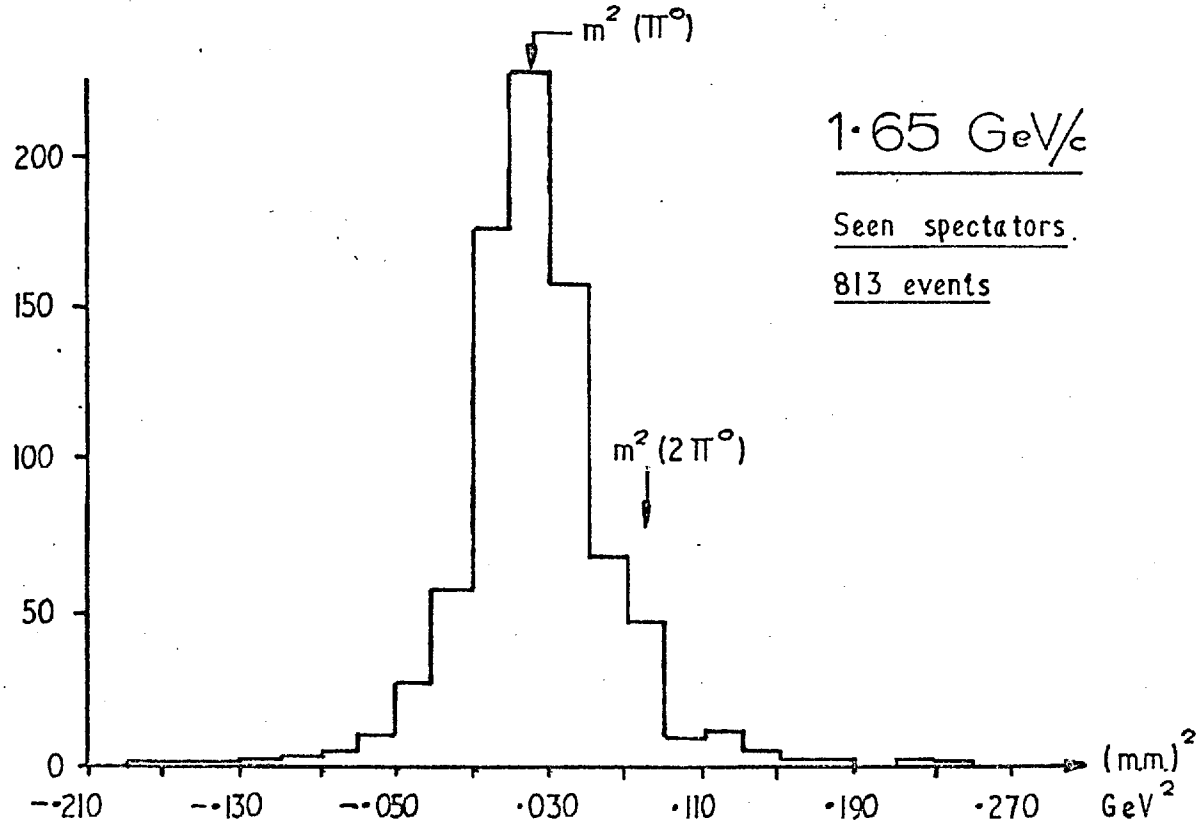


FIGURE 5.3 $(M.M.)^2$ FOR $\Lambda^\circ \pi^- \pi^\circ$

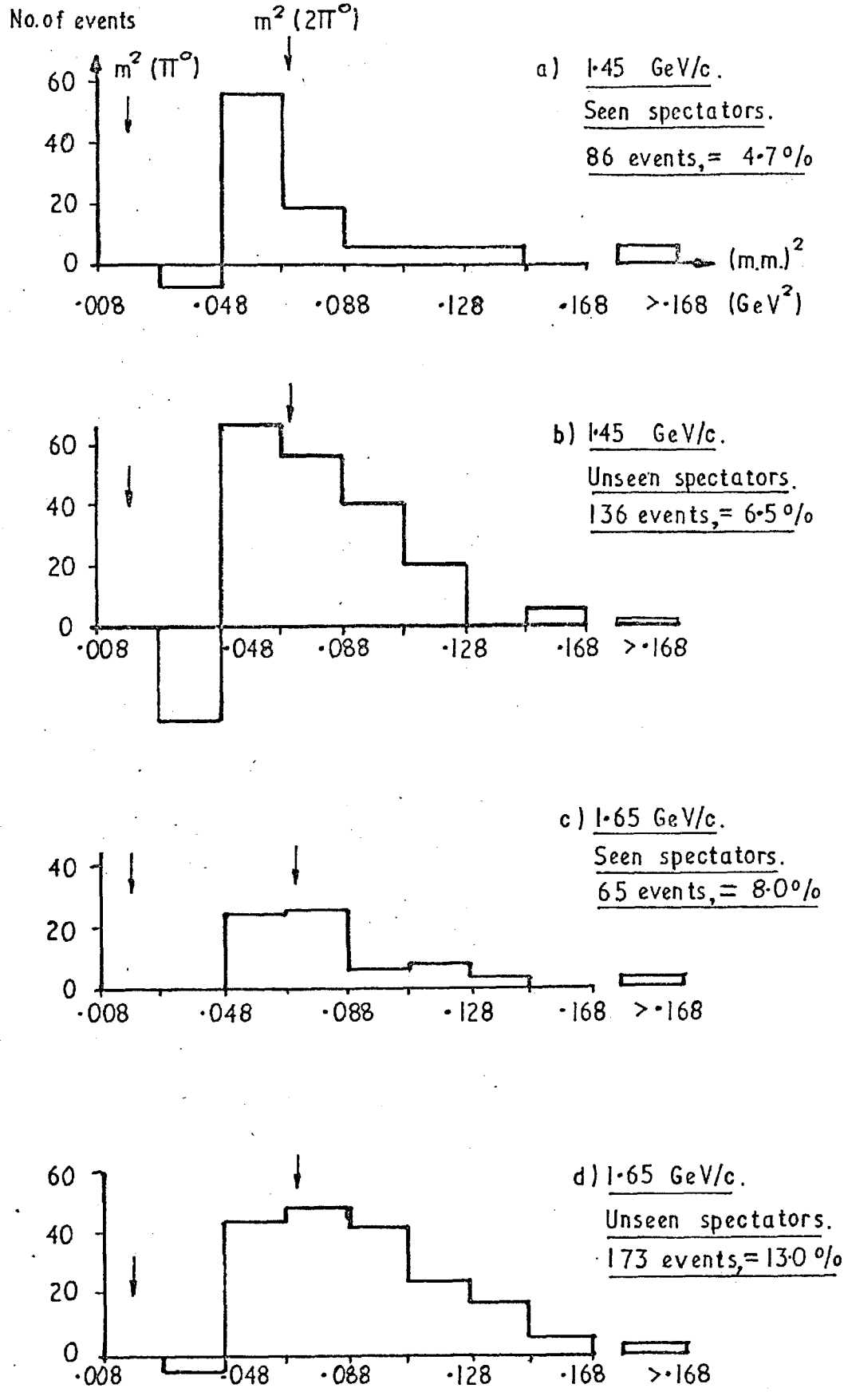


FIGURE 5.4 EXCESS EVENTS ON R.H.S. OF $(M.M.)^2$ FOR $\Lambda^0\pi^-\pi^0$.

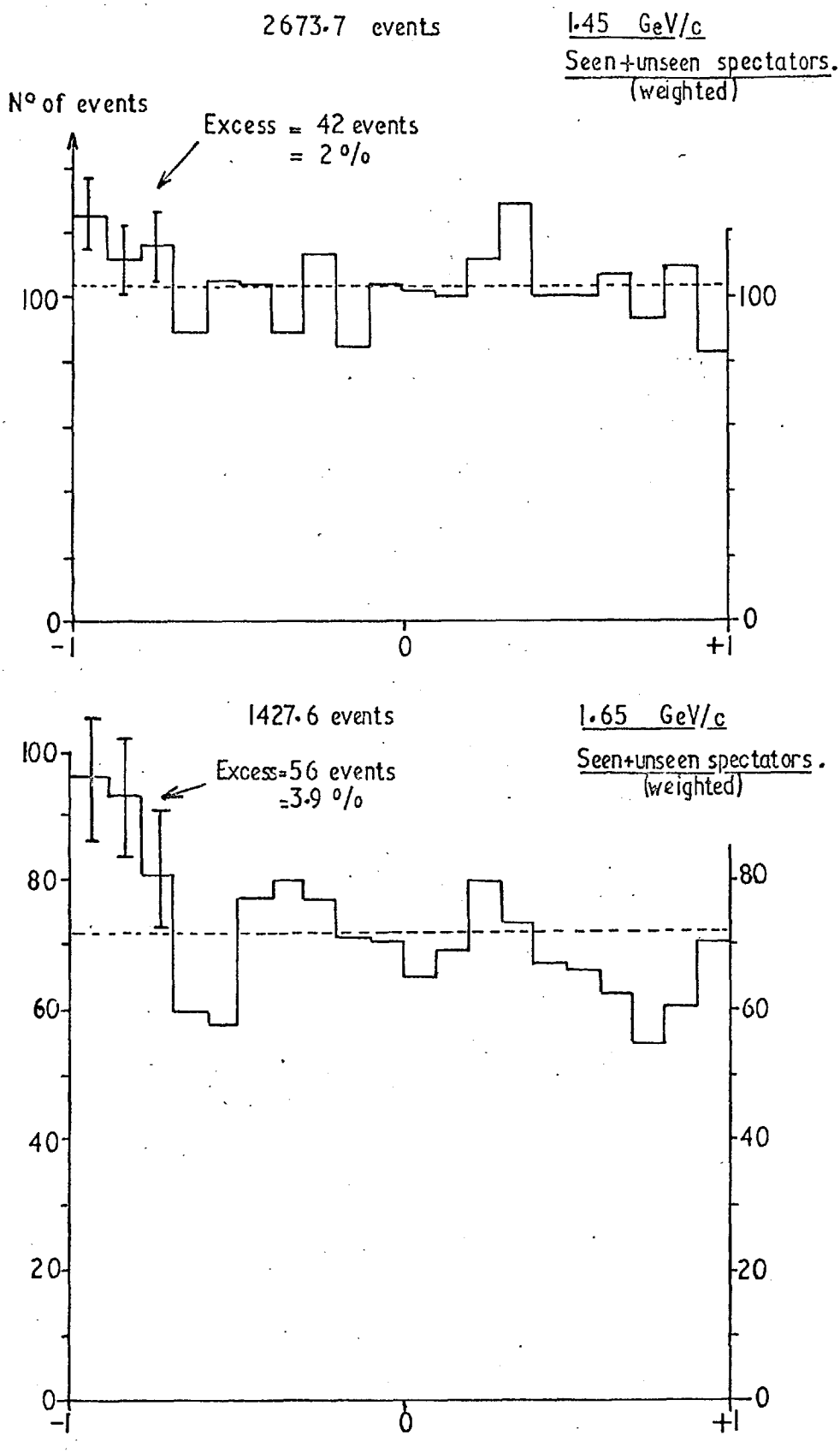


FIGURE 5.5 COS $\Theta_d(\pi^-)$ FOR $K^0_S$ DECAY, IN CHANNEL $n\bar{K}^0\pi^-$

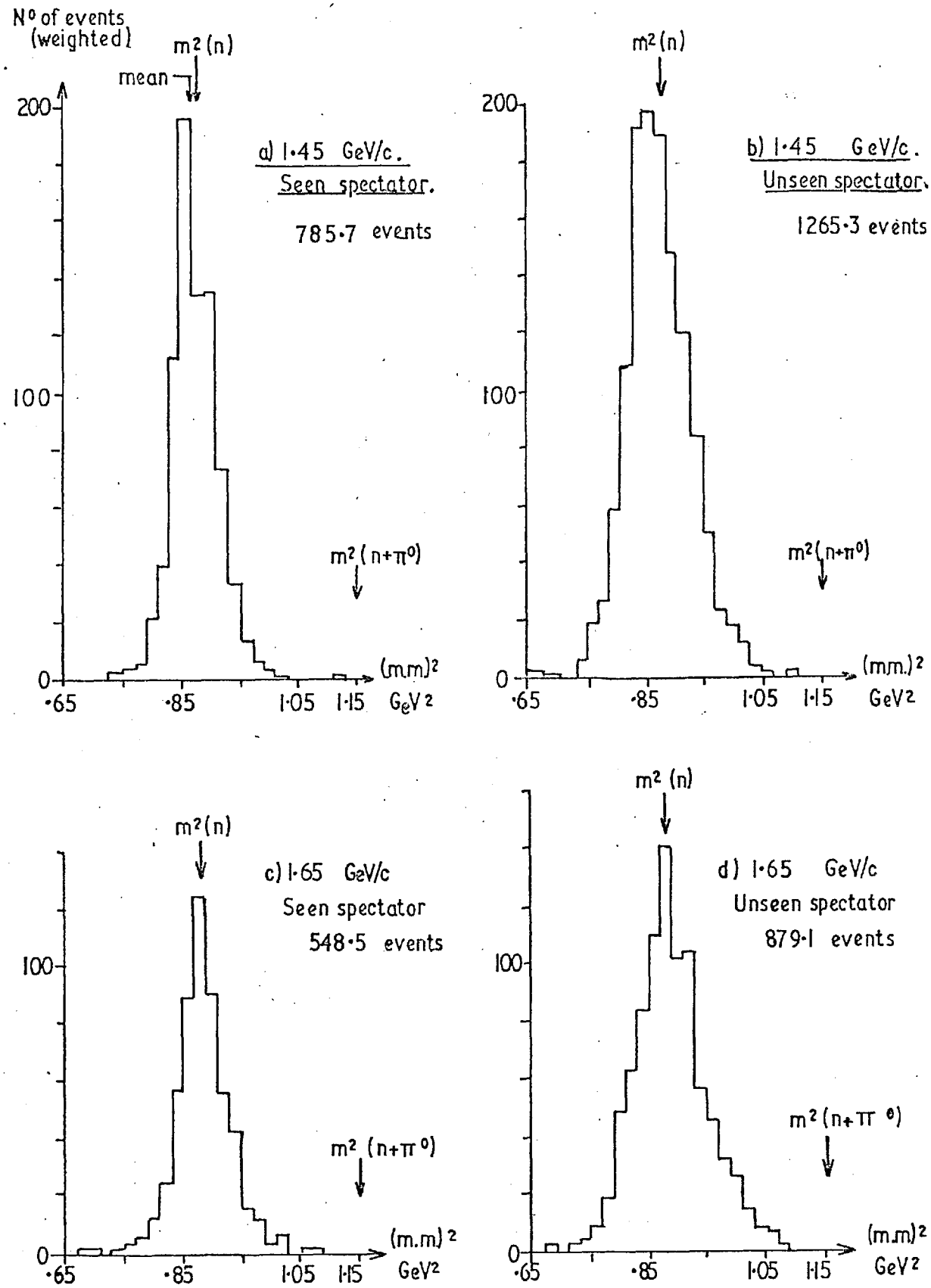


FIGURE 5.6 (M.M)² FOR $n\bar{K}^{\circ}\pi^{-}$.

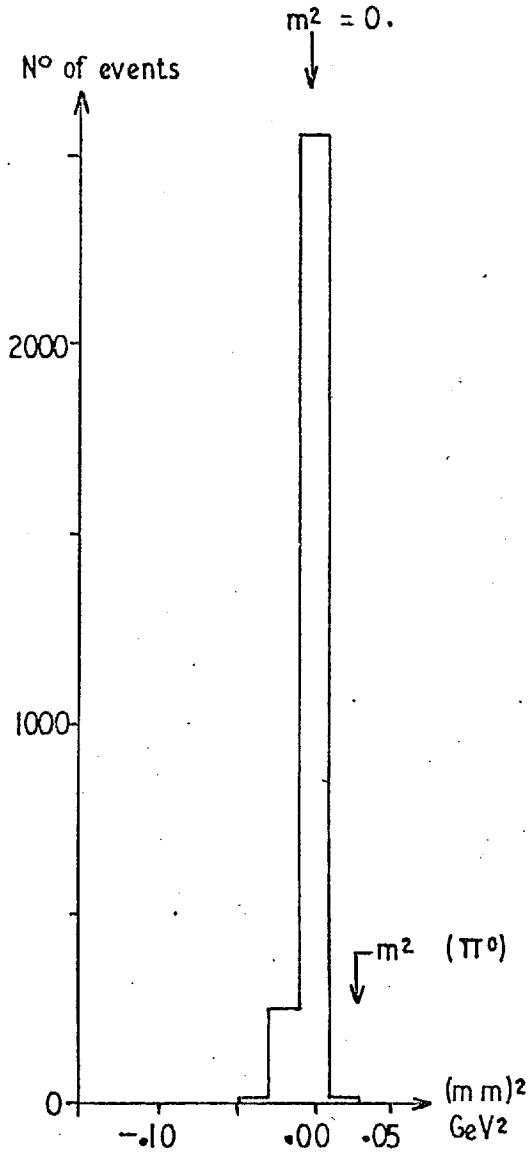


a) 1·45 GeV/c. 2828 events.

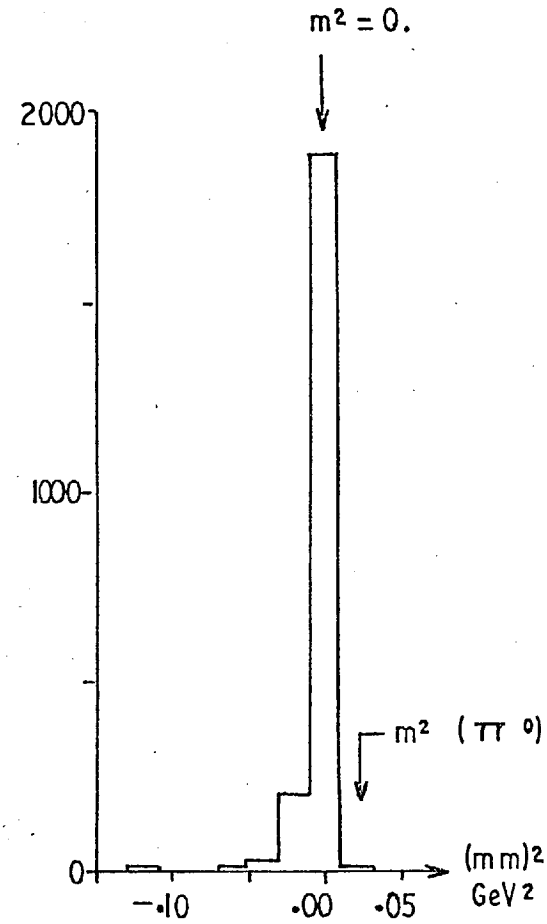


b) 1·65 GeV/c. 2136 events.

FIGURE 5.7 (M.M.)² FOR $pK^-\pi^-$ (ALL 4-CONSTRAINT FITS).

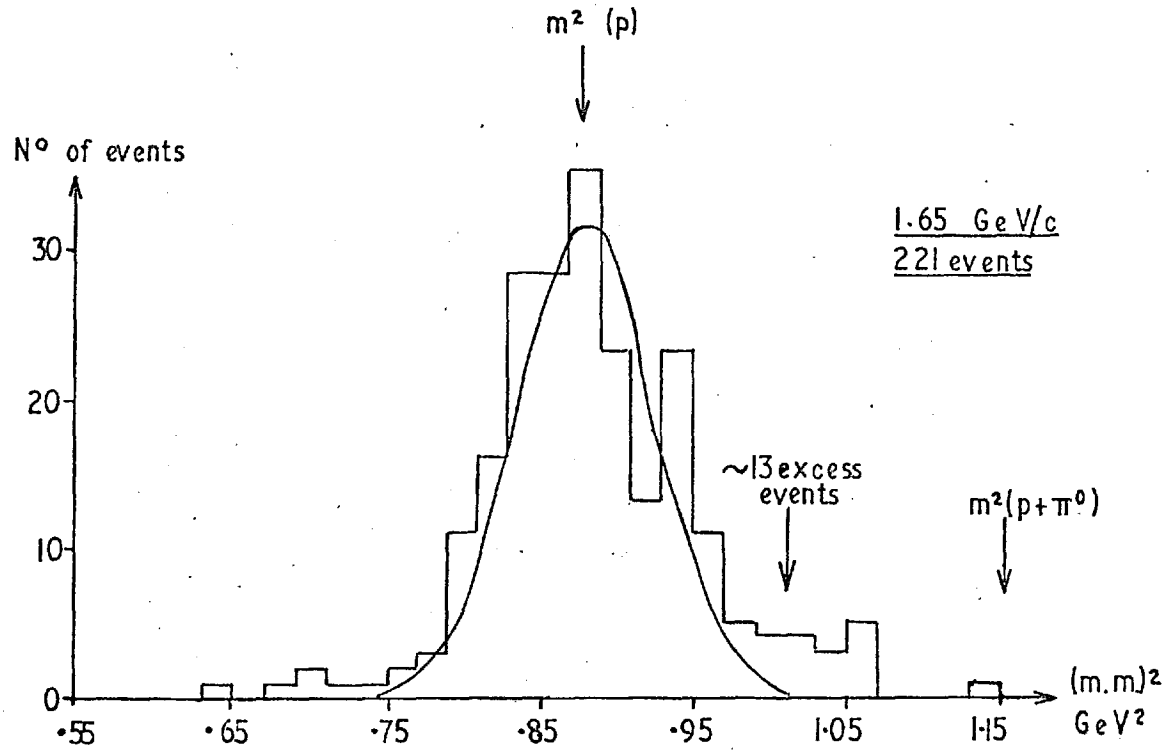


FIGURE 5·8 $(MM)^2$ FOR $pK^-\pi^-$ ONE-CONSTRAINT FITS. (UNSEEN SPECTATOR EVENTS ONLY).

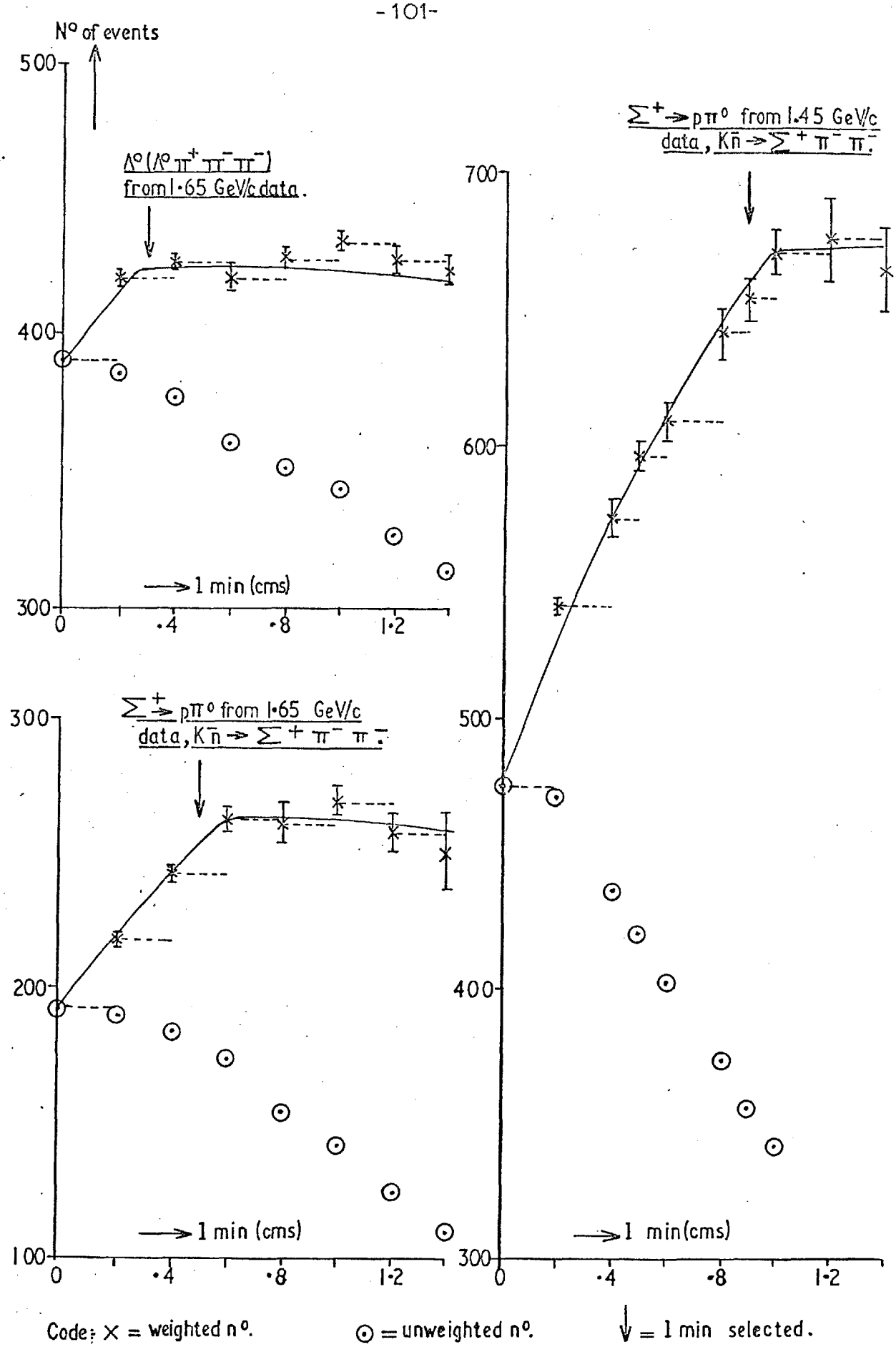


FIGURE 5·9 WEIGHTED NUMBERS OF EVENTS VERSUS MINIMUM LENGTH CUT.

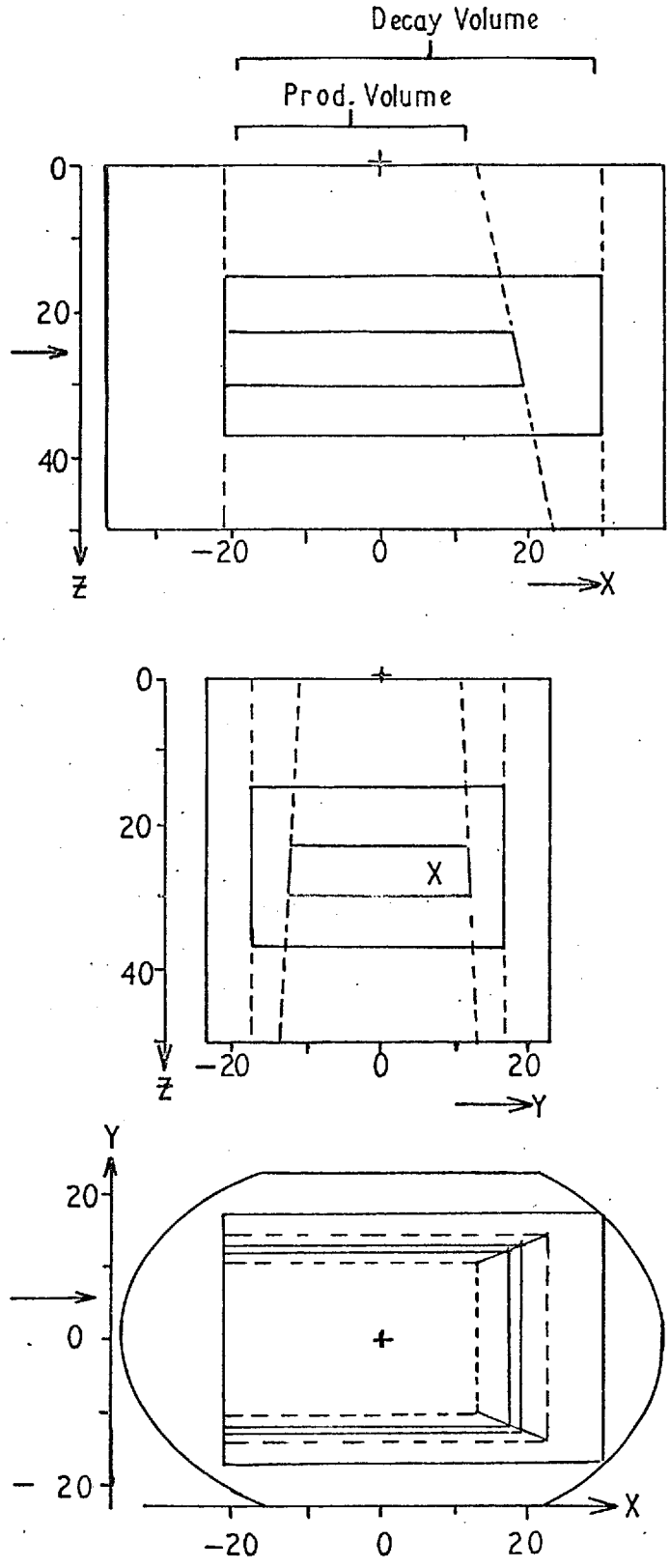


FIGURE 5.10 PRODUCTION & DECAY FIDUCIAL VOLUMES.

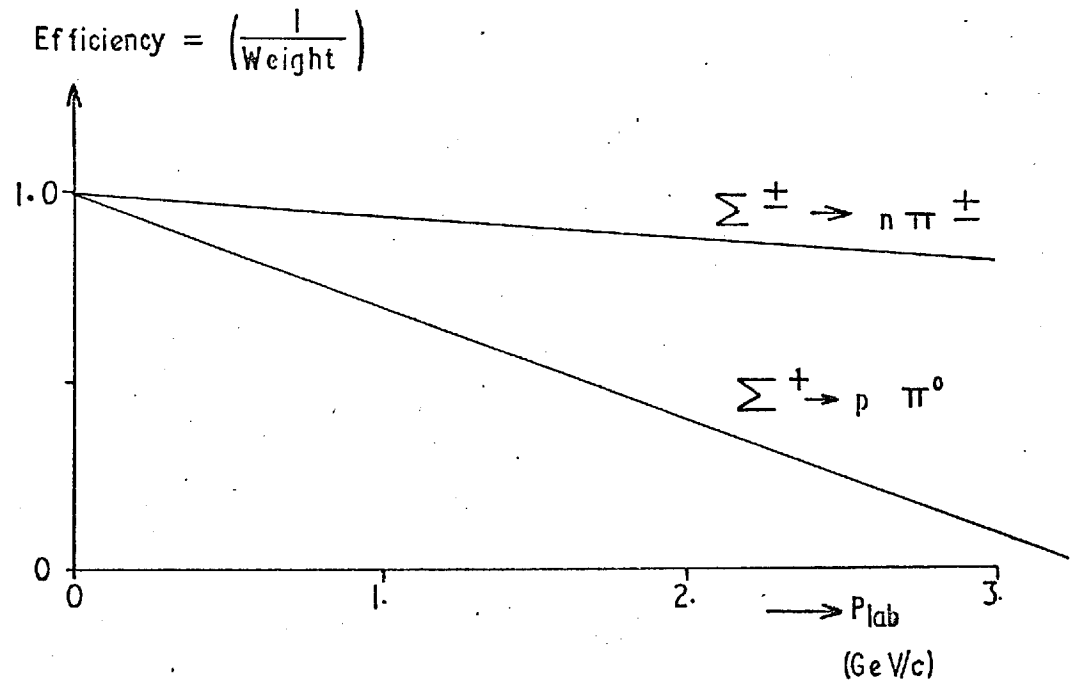


FIGURE 5.11 CORRECTION FOR LOSS OF SMALL ANGLE $\Sigma^{\pm}$ DECAYS.

# CHAPTER 6 Cross-section calculations for all fittable reactions.

## 6.1 Introduction.

### 6.1.1 Calculation method.

The cross-section for any reaction, "a", is given by

$$\sigma_a = \frac{\text{(No. of interactions of type a) x (Correction factors)}}{\text{(No. of targets/unit volume) x (Total beam track length)}} \qquad (6.1$$

The correction factors correct for ambiguous fits, differences in scanning and processing efficiency for different topologies, unseen charged or neutral Vee decays etc. and are discussed in sections 6.2, 6.3 and 6.4.

The total beam-track length, for $K^-$ particles has been calculated from the observed number of tau decays. Beam-track counting could not be used, since the $\mu^-$ contamination of the beam was not accurately known.

To obtain the total track length from the tau count, we note the probability of a $K^-$ decay per unit time in the laboratory system is

$$\frac{1}{T_1} = \frac{1}{\gamma T_o} \qquad (6.2$$

where $T_1$ = mean laboratory lifetime

$T_o$ = mean proper lifetime.

Hence, the probability of decay in length dx is given by:

$$\frac{dx}{c\beta\gamma T_o} = \frac{m'dx}{p'T_o} \qquad (6.3$$

where p' = laboratory momentum of $K^-$ particle.

m' = rest mass of $K^-$ particle

If $N_T$ tau decays are seen, for which the branching ratio is R, it then follows that:

$$\text{total } K^- \text{ track length} = \frac{N_T p' T_o}{Rm'}$$

$$= \frac{N_T pcT_o}{Rm} \qquad (6.4$$

(if p is in MeV/c and m in MeV).

Then $$\sigma_a = \frac{N_a \times (\text{Correction factors})}{d(A/W)\, N_T\, pc\, T_o/(Rm)} \qquad (6.5$$

The density of deuterium (d), was taken as = .107± .002 gms/cc[52].

p = mean momentum of $K^-$ particles at collision.

= 1.643± .001 GeV/c for nominal 1.65 GeV/c runs.

and 1.445± .001 GeV/c for nominal 1.45 GeV/c runs.

(these values are obtained from momentum histograms for tau decays).

This expression reduces to:

$$\sigma_a = \frac{N_a}{N_T} \times (\text{Correction factors}) \times F \qquad (6.6$$

where F = 1.31 ± .03 mb for 1.65 GeV/c runs. (6.7

= 1.49 ± .03 mb for 1.45 GeV/c runs.

The largest contributions to the error in F are the errors in d (2%) and in R (1%).

## 6.1.2 Explanation of cross-section tables.

Values of $N_a$, the correction factors, and cross-sections for the Imperial College events from the first two runs of 1.65 GeV/c film are given in table 6.1, and the results for all the Imperial College 1.45 GeV/c film are given in table 6.2. All fittable reactions from $K^-n$ collisions that contain events are considered, except for elastic scattering and the $\Xi K$ channels, which are discussed elsewhere (references 85 and 84 respectively.)

The topology codes are given for each reaction; they are odd for tau decays and when the spectator proton is not seen, and even when the spectator proton is seen. In this chapter two topologies differing only in

Table 6.1. Cross-sections for Imperial College data from runs 1 and 2 at 1.65 GeV/c.

| Reaction | Topology | Spectator | Unique events | Ambiguous events | Assigned ambigs. | No. of taus | Corr. for unseen decays. |
|---|---|---|---|---|---|---|---|
| $\Lambda\pi^-$ | 201 | s | 41 | 28 | +26 | 243 | 1.53 |
| $\hookrightarrow p\pi^-$ | 101 | u | 89 | 0 | -7 | 273 | 1.53 |
| $\Sigma^0\pi^-$ | 201 | s | 16 | 31 | 5 | 273 | 1.53 |
| $\hookrightarrow\gamma\Lambda\rightarrow p\pi^-$ | | | | | | | |
| $\Sigma^-\pi^0$ | 210 | s | 10 | 1 | 1 | 273 | 1.0 |
| $\hookrightarrow n\pi^-$ | | | | | | | |
| $pK^-\pi^-$ | 400 | s | 83 | 0 | 0 | 235 | - |
| | 300 | u | 196 | 0 | 0 | 265 | - |
| $n\bar{K}^0\pi^-$ | 201 | s | 53 | 0 | 0 | 273 | 2.92 |
| $\hookrightarrow\pi^+\pi^-$ | | | | | | | |
| $\Lambda\pi^-\pi^0$ | 201 | s | 90 | 3 | 0 | 273 | 1.53 |
| $\hookrightarrow p\pi^-$ | | | | | | | |
| $\Sigma^-\pi^+\pi^-$ | 410 | s | 31 | 0 | 0 | 243 | 1.0 |
| $\hookrightarrow n\pi^-$ | 310 | u | 44 | 0 | 0 | 273 | 1.0 |
| $\Sigma^+\pi^-\pi^-$ | 410 | s | 12 | 0 | 0 | 243 | 1.89 |
| $\hookrightarrow p\pi^0$ | 310 | u | 21 | 0 | 0 | 273 | 1.89 |
| $\Sigma^+\pi^-\pi^-$ | 410 | s | 17 | 0 | 0 | 243 | 2.12 |
| $\hookrightarrow n\pi^+$ | 310 | u | 27 | 0 | 0 | 273 | 2.12 |
| $pK^-\pi^-\pi^0$ | 400 | s | 5 | 0 | 0 | 265 | - |
| $p\bar{K}^0\pi^-\pi^-$ | 400 | s | 2 | 0 | 0 | 265 | 1.52 |
| $nK^-\pi^+\pi^-$ | 400 | s | 19 | 9 | 4.3 | 265 | - |

| Reaction | Spectator | Decay weight | Other corrections | Corrected no. of events | Cross-section (mb) |
|---|---|---|---|---|---|
| $\Lambda\pi^-$ | s | 1.18 | 1.43 | 173 | 1.91 ± .24 |
| | u | 1.18 | 1.38 | 204 | |
| $\Sigma^0\pi^-$ | s | 1.18 | 4.52 | 172 | 0.83 ± .22 |
| $\Sigma^-\pi^0$ | s | 1.23 | 5.03 | 68.1 | 0.33 ± .10 |
| $pK^-\pi^-$ | s | - | 1.23 | 102. | 1.68 ± .16 |
| | u | - | 1.15 | 224. | |
| $n\bar{K}^0\pi^-$ | s | 1.13 | 4.42 | 773 | 3.70 ± .62 |
| $\Lambda\pi^-\pi^0$ | s | 1.15 | 4.07 | 643 | 3.08 ± .46 |
| $\Sigma^-\pi^+\pi^-$ | s | 1.22 | 1.43 | 55.7 | 0.65 ± .09 |
| | u | 1.22 | 1.31 | 72.7 | |
| $\Sigma^+\pi^-\pi^-$ | s | 1.71 | 1.43 | 60.6 | 0.79 ± .17 |
| $\hookrightarrow p\pi^0$ | u | 1.71 | 1.31 | 97.2 | |
| $\Sigma^+\pi^-\pi^-$ | s | 1.40 | 1.43 | 74.3 | 0.92 ± .16 |
| $\hookrightarrow n\pi^+$ | u | 1.40 | 1.31 | 108. | |
| $pK^-\pi^-\pi^0$ | s | - | 3.90 | 19.5 | 96 ± 44μb |
| $(p\bar{K}^0\pi^-\pi^-$ | s | - | 3.90 | 11.9 | 58 ± 41μb ) |
| $nK^-\pi^+\pi^-$ | s | - | 3.90 | 91.5 | 0.45 ± .12 |

| Reaction | Topology | Spectator | Unique events | Ambiguous events | Assigned ambigs. | No. of taus | Corr. for unseen decays |
|---|---|---|---|---|---|---|---|
| $(\Lambda\pi^+\pi^-\pi^-$ | 400 | s | 17 | 13 | 6.3 | 265 | 2.88 ) |
| $(\Sigma^0\pi^+\pi^-\pi^-$ | 400 | s | 9 | 5 | 2.3 | 265 | 2.88 ) |
| $\Lambda\pi^+\pi^-\pi^-$ | 401 | s | 12 | 1 | 1 | 243 | 1.53 |
| $\hookrightarrow p\pi^-$ | 301 | u | 42 | 0 | -8 | 273 | 1.53 |
| $\Lambda\pi^+\pi^-\pi^-\pi^0$ $\hookrightarrow p\pi^-$ | 401 | s | 1 | 0 | 0 | 273 | 1.53 |
| $\Sigma^0\pi^+\pi^-\pi^-$ | 401 | s | 2 | 1 | 0 | 273 | 1.53 |
| $\hookrightarrow\gamma\Lambda\rightarrow p\pi^-$ | | | | | | | |
| $p\bar{K}^0\pi^-\pi^-$ | 401 | s | 0 | 0 | 0 | 243 | 2.92 |
| $\hookrightarrow\pi^+\pi^-$ | 301 | u | 2 | 0 | 0 | 273 | 2.92 |
| $n\bar{K}^0\pi^+\pi^-\pi^-$ | 401 | s | 0 | 0 | 0 | 273 | 2.92 |
| $\hookrightarrow\pi^+\pi^-$ | | | | | | | |
| $\Sigma^-\pi^+\pi^-\pi^0$ | 410 | s | 7 | 1 | .5 | 273 | 1.0 |
| $\hookrightarrow n\pi^-$ | | | | | | | |
| $\Sigma^+\pi^-\pi^-\pi^0$ | 410 | s | 3 | 0 | 0 | 273 | 1.89 |
| $\hookrightarrow p\pi^0$ | | | | | | | |
| $\Sigma^+\pi^-\pi^-\pi^0$ | 410 | s | 3 | 0 | 0 | 273 | 2.12 |
| $\hookrightarrow n\pi^+$ | | | | | | | |

( ) indicates an unreliable reaction topology. See section 6.6

| Reaction | Spectator | Decay weight | Other corrections | Corrected no. of events | Cross-section (mb) |
|---|---|---|---|---|---|
| ( $\Lambda\pi^+\pi^-\pi^-$ | s | - | 3.90 | 262 | 1.29 ± .36 ) |
| ($\Sigma^0\pi^+\pi^-\pi^-$ | s | - | 3.90 | 127 | 0.63 ± .23 ) |
| $\Lambda\pi^+\pi^-\pi^-$ | s | 1.15 | 1.77 | 40.4 | 0.64 ± .10 |
| | u | 1.15 | 1.47 | 87.9 | |
| $\Lambda\pi^+\pi^-\pi^-\pi^0$ | s | 1.05 | 5.63 | 9.07 | 43 ± 43μb |
| $\Sigma^0\pi^+\pi^-\pi^-$ | s | 1.15 | 5.63 | 19.8 | 95 ± 67μb |
| $p\bar{K}^0\pi^-\pi^-$ | s | 1.15 | 1.77 | 0 | 47 ± 38μb |
| | u | 1.15 | 1.47 | 9.9 | |
| $n\bar{K}^0\pi^+\pi^-\pi^-$ | s | 1.10 | 5.63 | <19.0 | <91μb |
| $\Sigma^-\pi^+\pi^-\pi^0$ | s | 1.28 | 4.51 | 43.4 | 0.21 ± .08 |
| $\Sigma^+\pi^-\pi^-\pi^0$ $\hookrightarrow p\pi^0$ | s | 1.75 | 4.51 | 44.7 | 0.21 ± .12 |
| $\Sigma^+\pi^-\pi^-\pi^0$ $\hookrightarrow n\pi^+$ | s | 1.44 | 4.51 | 41.5 | 0.20 ± .12 |

Table 6.2 Cross-sections for all Imperial College data at 1.45 GeV/c.

| Reaction | Topology | Spectator | Unique events | Ambiguous events | Assigned ambigs. | Corr. for unseen decays |
|---|---|---|---|---|---|---|
| Tau decays | 300 | - | 675 | 0 | 0 | - |
| $\Lambda\pi^-$ | 201 | s | 84 | 90 | 76 | 1.53 |
| $\hookrightarrow p\pi^-$ | 101 | u | 133 | 262 | 228 | 1.53 |
| $\Sigma^0\pi^-$ | 201 | s | 41 | 107 | 24 | 1.53 |
| $\hookrightarrow\gamma\Lambda\rightarrow p\pi^-$ | 101 | u | 34 | 299 | 56 | 1.53 |
| $\Sigma^-\pi^0$ | 210 | s | 68 | 5 | 2 | 1.0 |
| $\hookrightarrow n\pi^-$ | 110 | u | - 110 topology not measured - | | | |
| $pK^-\pi^-$ | 400 | s | 133 | 12 | 6 | - |
| | 300 | u | 361 | 24 | 12 | - |
| $n\bar{K}^0\pi^-$ | 201 | s | 94 | 1 | 1 | 2.92 |
| $\hookrightarrow\pi^+\pi^-$ | 101 | u | 250 | 7 | 3 | 2.92 |
| $\Lambda\pi^-\pi^0$ | 201 | s | 249 | 17 | 7 | 1.53 |
| $\hookrightarrow p\pi^-$ | 101 | u | 488 | 37 | 16 | 1.53 |
| $\Sigma^-\pi^+\pi^-$ | 410 | s | 55 | 0 | 0 | 1.0 |
| $\hookrightarrow n\pi^-$ | 310 | u | 149 | 2 | 2 | 1.0 |
| $\Sigma^+\pi^-\pi^-$ | 410 | s | 10 | 0 | 0 | 1.89 |
| $\hookrightarrow p\pi^0$ | 310 | u | 41 | 0 | 0 | 1.89 |
| $\Sigma^+\pi^-\pi^-$ | 410 | s | 22 | 0 | 0 | 2.12 |
| $\hookrightarrow n\pi^+$ | 310 | u | 58 | 1 | 1 | 2.12 |
| $pK^-\pi^-\pi^0$ | 400 | s | 13 | 3 | 1 | - |
| | 300 | u | 44 | 3 | 1 | - |

| Reaction | Spectator | Decay weight | Other corrections | Corrected no. of events | Cross-section (mb) |
|---|---|---|---|---|---|
| Tau decays | - | - | 1.06 | 715 | - |
| $\Lambda\pi^-$ | s | 1.19 | 1.19 | 348 | 2.30 ± .25 |
| | u | 1.18 | 1.17 | 764 | |
| $\Sigma^0\pi^-$ | s | 1.19 | 1.20 | 143 | 0.70 ± .09 |
| | u | 1.19 | 1.19 | 195 | |
| $\Sigma^-\pi^0$ | s | 1.24 | 4.57 | 397 | 0.83 ± .13 |
| | u | - Not measured - | | | |
| $pK^-\pi^-$ | s | - | 1.16 | 161 | 1.19 ± .09 |
| | u | - | 1.10 | 408 | |
| $n\bar{K}^0\pi^-$ | s | 1.13 | 1.18 | 371 | 2.78 ± .23 |
| | u | 1.16 | 1.13 | 968 | |
| $\Lambda\pi^-\pi^0$ | s | 1.12 | 1.19 | 522 | 3.34 ± .25 |
| | u | 1.15 | 1.22 | 1085 | |
| $\Sigma^-\pi^+\pi^-$ | s | 1.26 | 1.26 | 87.5 | 0.65 ± .06 |
| | u | 1.25 | 1.18 | 223 | |
| $\Sigma^+\pi^-\pi^-$ | s | 2.64 | 1.26 | 63.6 | 0.63 ± .12 |
| $\hookrightarrow p\pi^0$ | u | 2.60 | 1.18 | 239.5 | |
| $\Sigma^+\pi^-\pi^-$ | s | 1.37 | 1.26 | 81.0 | 0.58 ± .08 |
| $\hookrightarrow n\pi^+$ | u | 1.34 | 1.18 | 198.0 | |
| $pK^-\pi^-\pi^0$ | s | - | 1.22 | 17.1 | 0.14 ± .02 |
| | u | - | 1.16 | 52.1 | |

| Reaction | Topology | Spectator | Unique events | Ambiguous events | Assigned ambigs. | Corr. for unseen decays |
|---|---|---|---|---|---|---|
| $(p\bar{K}^{o}\pi^{-}\pi^{-}$ | 400 | s | 3 | 2 | 1 | 1.52 ) |
| ( | 300 | u | 13 | 1 | 1 | 1.52 ) |
| $nK^{-}\pi^{+}\pi^{-}$ | 400 | s | 13 | 10 | 4.5 | - |
| | 300 | u | 26 | 21 | 9 | - |
| $(\Lambda\pi^{+}\pi^{-}\pi^{-}$ | 400 | s | 22 | 23 | 11 | 2.88 ) |
| ( | 300 | u | 44 | 62 | 29.5 | 2.88 ) |
| $(\Sigma^{o}\pi^{+}\pi^{-}\pi^{-}$ | 400 | s | 7 | 18 | 7.5 | 2.88 ) |
| ( | 300 | u | 9 | 50 | 23.5 | 2.88 ) |
| $\Lambda\pi^{+}\pi^{-}\pi^{-}$ | 401 | s | 40 | 12 | 10 | 1.53 |
| $\hookrightarrow p\pi^{-}$ | 301 | u | 57 | 47 | 25 | 1.53 |
| $\Lambda\,\pi^{+}\pi^{-}\pi^{-}\pi^{o}$ | 401 | s | 2 | 0 | 0 | 1.53 |
| $\hookrightarrow p\pi^{-}$ | 301 | u | 3 | 2 | 1 | 1.53 |
| $\Sigma^{o}\pi^{+}\pi^{-}\pi^{-}$ | 401 | s | 3 | 12 | 2 | 1.53 |
| $\hookrightarrow\gamma\Lambda\rightarrow p\pi^{-}$ | 301 | u | 2 | 48 | 23 | 1.53 |
| $p\bar{K}^{o}\pi^{-}\pi^{-}$ | 401 | s | 1 | 0 | 0 | 2.92 |
| $\hookrightarrow\pi^{+}\pi^{-}$ | 301 | u | 1 | 0 | 0 | 2.92 |
| $n\bar{K}^{o}\pi^{+}\pi^{-}\pi^{-}$ | 401 | s | 0 | 0 | 0 | 2.92 |
| $\hookrightarrow\pi^{+}\pi^{-}$ | 301 | u | 0 | 0 | 0 | 2.92 |
| $\Sigma^{-}\pi^{+}\pi^{-}\pi^{o}$ | 410 | s | 20 | 2 | 2 | 1.0 |
| $\hookrightarrow n\,\pi^{-}$ | 310 | u | 44 | 2 | 2 | 1.0 |
| $\Sigma^{+}\pi^{-}\pi^{-}\pi^{o}$ | 410 | s | 4 | 0 | 0 | 1.89 |
| $\hookrightarrow p\pi^{o}$ | 310 | u | 15 | 0 | 0 | 1.89 |
| $\Sigma^{+}\pi^{-}\pi^{-}\pi^{o}$ | 410 | s | 3 | 0 | 0 | 2.12 |
| $\hookrightarrow n\pi^{+}$ | 310 | u | 9 | 2 | 2 | 2.12 |

( ) indicates an unreliable reaction topology. See section 6.6.

| Reaction | Spectator | Decay weight | Other corrections | Corrected no. of events | Cross-section (mb) |
|---|---|---|---|---|---|
| $(p\bar{K}^{o}\pi^{-}\pi^{-}$ | s | - | 1.22 | 7.4 | $67 \pm 17\mu b$ ) |
| ( | u | - | 1.16 | 24.7 | ) |
| $nK^{-}\pi^{+}\pi^{-}$ | s | - | 1.22 | 21.4 | $0.13 \pm .02$ |
| | u | - | 1.16 | 40.6 | |
| $(\Lambda\pi^{+}\pi^{-}\pi^{-}$ | s | - | 1.22 | 116. | $0.75 \pm .11$ ) |
| ( | u | - | 1.16 | 245. | ) |
| $(\Sigma^{o}\pi^{+}\pi^{-}\pi^{-}$ | s | - | 1.22 | 51. | $0.33 \pm .06$ ) |
| ( | u | - | 1.16 | 108. | ) |
| $\Lambda\pi^{+}\pi^{-}\pi^{-}$ | s | 1.135 | 1.18 | 97.4 | $0.55 \pm .07$ |
| | u | 1.135 | 1.16 | 166. | |
| $\Lambda\pi^{+}\pi^{-}\pi^{-}\pi^{o}$ | s | 1.08 | 1.14 | 3.8 | $25 \pm 10\mu b$ |
| | u | 1.16 | 1.18 | 8.4 | |
| $\Sigma^{o}\pi^{+}\pi^{-}\pi^{-}$ | s | 1.11 | 1.14 | 9.7 | $0.125 \pm .025$ |
| | u | 1.11 | 1.18 | 50.3 | |
| $p\bar{K}^{o}\pi^{-}\pi^{-}$ | s | 1.09 | 1.12 | 3.6 | $17 \pm 12\mu b$ |
| | u | 1.27 | 1.16 | 4.3 | |
| $n\bar{K}^{o}\pi^{+}\pi^{-}\pi^{-}$ | s | 1.1 | 1.14 | $\lesssim 3.7$ | $\lesssim 16\mu b$ |
| | u | 1.1 | 1.18 | $\lesssim 3.8$ | |
| $\Sigma^{-}\pi^{+}\pi^{-}\pi^{o}$ | s | 1.27 | 1.29 | 36.1 | $0.21 \pm .03$ |
| | u | 1.20 | 1.21 | 67. | |
| $\Sigma^{+}\pi^{-}\pi^{-}\pi^{o}$ | s | 2.43 | 1.29 | 23.8 | $0.22 \pm .06$ |
| $\hookrightarrow p\pi^{o}$ | u | 2.37 | 1.21 | 81.3 | |
| $\Sigma^{+}\pi^{-}\pi^{-}\pi^{o}$ | s | 1.33 | 1.29 | 10.9 | $0.10 \pm .03$ |
| $\hookrightarrow n\pi^{+}$ | u | 1.34 | 1.21 | 37.9 | |

the visibility of the proton (e.g. 101 and 201) are referred to collectively by the odd topology code; when necessary the spectator proton is specified to be unseen or seen.

The table also specifies whether the spectator is seen (s) or unseen (u). These two classes are treated separately for each reaction, as they need different correction factors.

The value used for $N_a$ in equation 6.6, is the number of unique events plus the numher of ambiguous events assigned to that reaction ("assigned ambigs."). Both numbers are those obtained after the application of the decay length cuts, and after requiring that the momentum of the spectator proton is less than 300 MeV/c (or 280 MeV/c for 1.45 GeV/c data). The cross-section per event, before corrections, is given by $(F/N_T)$ and is 5.4 μbarns per event for Imperial College 1.65 GeV/c data, and 2.2 μbarns per event for 1.45 GeV/c data (about 1.0 μbarns per event at 1.65 GeV/c and 0.37 μbarns per event at 1.45 GeV/c, for the whole collaboration).

The correction factors listed in the tables are those for unseen decays, the decay weights and all others combined. This last consists of:-

(Scanning loss) x (Processing loss) x (Contamination)
x (Probability cut) x (Unseen spectators loss) x (Glauber corrections)
x (Fast spectators correction) (6.7

The values for each of these correction factors can be found in this chapter; the first two in table 6.4, the third in tables 6.5 and 6.6, and the fourth in section 6.2.7. The last three corrections are the same for all reactions at a given beam momentum, and their values are given in sections 6.2.8, 6.3 and 6.4 respectively.

The error on the cross-section given includes the statistical error on the number of events seen, and the errors on all other factors in the calculation; this is discussed in section 6.5.

## 6.2 Correction factors.

### 6.2.1 Introduction.

The assignment of ambiguous events, and the various correction factors are discussed below in more detail. The Glauber correction and the correction for fast spectator events are rather different problems, and are examined in sections 6.3 and 6.4 respectively.

### 6.2.2 Ambiguous fits.

For the reactions with 101 and 301 topologies that involve a seen $\Lambda$ decay, many events gave fits ambiguous between $\Lambda\pi^-$, $\Sigma^0\pi^-$ and $\Lambda\pi^-\pi^0$ (for the 101 topology), and between $\Lambda\pi^+\pi^-\pi^-$ and similar reactions (for the 301 topology). The events were divided between the reactions on the basis of histograms of $\cos\vartheta_d$ ($\Lambda$); this is discussed in section 5.2, and figures 5.1 and 5.2 show the plots for $\Lambda\pi^-\pi^0$ / $\Sigma^0\pi^-$ and for $\Lambda\pi^-$ / $\Sigma^0\pi^-$ ambiguous events for the 1.65 GeV/c runs. The distributions should be flat for true $\Sigma^0$ events. The $\Lambda^0/\Sigma^0$ ambiguous events show a peak at $\cos\vartheta_d \simeq 1$; this is produced by true $\Lambda$ events where a slow backward gamma can be added with only a small effect on energy and momentum conservation, thus simulating a $\Sigma^0$. For $\Lambda\pi^0/\Sigma^0$ ambiguous events, a broad shoulder for $\cos\vartheta_d$ negative corresponds to true $\Lambda\pi^0$ events (see section 5.2.3). Studies of the $\cos\vartheta_d$ plots indicate that, for the 101 topology, about 90% of the $\Lambda$ /$\Sigma^0$ ambiguous events were really $\Lambda$ events, and about 40% of the $\Lambda\pi^0/\Sigma^0$ events were really $\Lambda\pi^0$ events; for the 301 topology, the "true $\Lambda$ " peak at $\cos\vartheta_d \simeq 1$ was less sharp, and generally more of the ambiguities were $\Sigma^0$ events. Table 6.3 shows a tabulation of these results.

Many ambiguous fits were also obtained between the 1-constraint reactions $nK^-\pi^+\pi^-$, $\Lambda\pi^+\pi^-\pi^-$ and $\Sigma^0\pi^+\pi^-\pi^-$ (with no neutral decays seen) because of the weakness of constraint and absence of a decay signature.

Table 6.3 Assignment of $\Lambda/\Sigma^{\circ}/\Lambda\pi^{\circ}$ ambiguous events.

For each group of data, the first line gives the raw numbers of unique and ambiguous events, while on the second line the assignment of the ambiguous events and the consequent reaction totals are shown.

| | Spectator | $\Lambda$ | $\Lambda/\Sigma^{\circ}$ | $\Sigma^{\circ}$ | $\Sigma^{\circ}/\Lambda\pi^{\circ}$ | $\Lambda\pi^{\circ}$ |
|---|---|---|---|---|---|---|
| 101 topology | | | | | | |
| 1.65 GeV/c | seen | 41 | 28 | 17 | 3 | 90 |
| | | 67 | 26/2 | 22 | 3/0 | 90 |
| | unseen | 89 | —— | Not fittable | —— | |
| | | 82 | -7 | - | - | - |
| 1.45 GeV/c | seen | 84 | 90 | 41 | 17 | 249 |
| | | 160 | 76/14 | 65 | 10/7 | 256 |
| | unseen | 133 | 262 | 34 | 37 | 488 |
| | | 361 | 228/34 | 89 | 21/16 | 504 |
| 301 topology | | | | | | |
| 1.65 GeV/c | seen | 12 | 1 | 2 | 0 | 1 |
| | | 13 | 1/0 | 2 | 0/0 | 1 |
| | unseen | 42 | —— | Not fittable | —— | |
| | | 34 | -8 | - | - | - |
| 1.45 GeV/c | seen | 40 | 12 | 3 | 0 | 2 |
| | | 50 | 10/2 | 5 | 0/0 | 2 |
| | unseen | 57 | 47 | 2 | 2 | 3 |
| | | 82 | 25/22 | 25 | 1/1 | 4 |

The last two reactions are probably also contaminated by mis-assigned events (see section 6.6).

The $nK^-\pi^+\pi^-$ ambiguous events were nearly all ambiguous with $\Lambda\pi^+\pi^-\pi^-$. Missing mass plots gave no indication as to how to assign these events; therefore they were shared equally between the channels.

No other reaction showed an appreciable number of ambiguous fits.

### 6.2.3 Unseen decay modes and decay losses.

Reactions involving a seen neutral or charged particle decay must be corrected for particle decays leading to other topologies, or to unfittable events. Also a few reactions involving a neutral particle that is not seen to decay, must be corrected for the seen decay modes. All branching ratios and errors are taken from reference 24; the errors range from 0.2% for $\Sigma^- \to n\pi^-$, to 3.0% for $\Sigma^+ \longrightarrow n\pi^+$.

The numbers of events in tables 6.1 and 6.2 are obtained after the application of the minimum and maximum decay length cuts, and are then weighted for unseen decay losses as discussed in section 5.3.

### 6.2.4 Scanning losses.

The scanning efficiency was calculated separately for each topology by comparing the first and second scans.

If $N_1$ = no. of events found in first scan,

$N_2$ = no. of events found in second scan,

and $N_{12}$ = no. of events found in both scans.

Then

$$\left.\begin{aligned} N_1 &= e_1 N_T \\ N_2 &= e_2 N_T \\ N_{12} &= e_1 e_2 N_T \end{aligned}\right\} \quad (6.9$$

where $N_T$ = total no. of events actually present

$e_1, e_2$ = efficiencies for first and second scans respectively.

Therefore $N_T = \frac{N_1 \cdot N_2}{N_{12}}$

and the overall efficiency = $e_o = \frac{(N_1+N_2-N_{12})}{N_T}$

$$= \frac{(N_1+N_2-N_{12}) \cdot N_{12}}{N_1 \cdot N_2} \qquad (6.10$$

Equation 6.9 assumes that losses are purely random. For the reactions discussed in this thesis, the events with track configurations of poor visibility were eliminated by minimum and maximum decay length cuts; therefore the assumption is reasonable. It is also reasonable to assume that different reactions with the same topology have approximately the same scanning efficiency.

Further corrections were made for extra events found during the check scan, and for the part of the 1.65 GeV/c film for which only a single scan was made.

The correction factor used is a ratio of efficiencies:

$$\frac{e_o(300 \text{ topology})}{e_o(\text{current topology})} \qquad (6.11$$

Table 6.4 gives this factor for all topologies except 200 for all runs. Only a part of the Imperial College film was used to calculate these values, but the errors are still only about 1 - 2%, small compared with other errors.

### 6.2.5 Processing losses.

Unmeasureable events, events giving zero-constraint fits, and events without good measurements, cannot give fits, and must be allowed for. The processing efficiency was found by counting the number of events in these categories, and comparing with the total number of scanned events. The correction factors were then calculated as for the scanning losses, according to equation 6.11, and are given in table 6.4.

Table 6.4 Correction factors for scanning losses and processing losses.

(Relative to the 300 topology)

| Topology | Scanning losses | | Processing losses | |
|---|---|---|---|---|
| | 1.65 GeV/c run | 1.45 GeV/c run | 1.65 GeV/c run | 1.45 GeV/c run |
| 101 | 1.05 | 1.01 | 1.04 | 1.00 |
| 1 prong rare | 1.39 | 0.98 | 1.12 | 1.00 |
| 201 | 1.09 | 1.00 | 1.10 | 1.02 |
| 210 | 1.20 | 1.22 | 1.10 | 1.05 |
| 2 prong rare | 1.20 | 1.02 | 1.26 | 1.32 |
| 300 | 1.00 | 1.00 | 1.00 | 1.00 |
| 301 | 1.01 | 0.98 | 1.16 | 1.02 |
| 310 | 0.99 | 0.97 | 1.06 | 1.05 |
| 3 prong rare | 1.18 | 1.52 | 1.15 | 1.14 |
| 400 | 1.02 | 1.01 | 1.07 | 1.03 |
| 401 | 1.10 | 0.97 | 1.35 | 1.00 |
| 410 | 1.07 | 0.97 | 1.12 | 1.13 |
| 4 prong rare | 1.25 | 1.11 | 1.40 | 1.45 |
| $>4$ prongs | 1.00 | 1.70 | - | 1.06 |
| Absolute value for 300 | 0.95 | 0.995 | 0.94 | 0.91 |

The processing losses, like the scanning losses, are assumed to be the same for different reactions with the same topology. All of the Imperial College events for the first two runs at 1.65 GeV/c, and for the run at 1.45 GeV/c were used to calculate the factors in table 6.4, which are subject to errors of about 1%.

### 6.2.6 Contamination.

Contamination of three-body channels has been discussed in chapter 5. The percentage contamination of various channels is shown for Imperial College events in tables 6.5 and 6.6. These differ slightly from the values given for the whole collaboration in chapter 5, since the $p_x$, $p_y$, $p_z$ fitting method was not used for Imperial College events at 1.65 GeV/c. A beam entry cut has been applied to all 1.65 GeV/c events of 300 topology, to reduce $\pi^-$ -induced contamination.

Corrections have not been made for $K^-$-induced contamination of the non three-body reactions. The contamination of the $\Lambda\pi^-$ and $\Sigma^0\pi^-$ reactions depends mainly on the accuracy of the assignment of the ambiguous events. The $\Sigma^-\pi^0$ reaction is contaminated mainly by events from the $\Sigma^-\pi^0\pi^0$ reaction, and it can be estimated from the study of $\Lambda\pi^-\pi^0$ contamination in section 5.2.3, that this will be less than 5% for all runs.

The contamination of the four- and five-body reactions should be very much less than their statistical errors, except for some of the 300 topology fits, which yield unreliable results (see section 6.6).

### 6.2.7 Fit probability.

In choosing kinematic hypotheses, it was required that the probability ($\chi^2$) should not be less than 1% for four-constraint fits, and 5% for one-constraint fits. The distribution of probability ($\chi^2$) would be expected to be flat, in which case corrections for the different cuts would be simple. In fact only one-constraint events at 1.45 GeV/c gave a flat

Table 6.5 Percentage contamination by $\pi^-$-induced reactions.

| Spectators → | 1.45 GeV/c run | | First two 1.65 GeV/c runs. | |
|---|---|---|---|---|
| Reaction ↓ | Seen | Unseen | Seen | Unseen |
| $pK^-\pi^-$ | 0 | 1 | 1 | 5 |
| All other 300 topology fits | 1 | 1.5 | 5 | 6 |

Table 6.6 Percentage contamination by $K^-$-induced reactions.

| Spectators → | 1.45 GeV/c run | | First two 1.65 GeV/c runs | |
|---|---|---|---|---|
| Reaction ↓ | Seen | Unseen | Seen | Unseen |
| $\Lambda\pi^-\pi^0$ <br> $\hookrightarrow p\pi^-$ | 1.6 * | -2.3 * | 12.0 | 19.5 |
| $n\bar{K}^0\pi^-$ <br> $\hookrightarrow \pi^+\pi^-$ | 0 | 3 | 4 | 6.5 |

* Missing mass required to be less than 265 MeV/$c^2$.

distribution (figure 3.9); at 1.65 GeV/c four-constraint collision fits and tau decay fits showed similar distributions, with a shoulder at low probabilities (figures 3.8a and b). At 1.45 GeV/c the tau decay fits alone showed a similar effect, but also all types of events gave an excess of events with high fit probabilities (figures 6.1 and 6.2). The latter bias was presumably caused by a slight overestimation of the measurement errors used for the GRIND kinematics program. The bias for four-constraint fits was probably caused by small inaccuracies in the reconstruction of points in space by the geometry program.

A careful study of the Imperial College film for the first two 1.65 GeV/c runs discovered 30 events that were very probably taus, from their track ionizations and missing mass, but had not previously given good fits to any hypothesis; for the same film 243 normal tau decay fits had been obtained. Thus 11% of tau decays did not fit with a probability more than 1%.

Table 6.7 shows the fraction of events of each type estimated to be excluded by the probability cut; at 1.45 GeV/c it was assumed that the excess of high probability events halved these fractions. The table also shows the corrections applied to obtain $N_a/N_T$ in equation 6.6, and the number of tau decay events found.

### 6.2.8 Unseen spectators.

For the 1.65 GeV/c events used in table 6.1, $p_x$, $p_y$, $p_z$ fits were not carried out, and so reactions involving one unseen neutral particle were unfittable when the spectator proton was also unseen. The boundary between seen and unseen spectator protons was estimated to be at a proton momentum of 85 $\pm$ 3 MeV/c (from figures 4.3a to d, and from plots for other reactions). With an upper spectator momentum limit of 300 MeV/c, a correction factor of 3.03 $\pm$ 0.17 is calculated from the Hulthén function, equation 4.2.

Table 6.7 Tau counts, and corrections for fit probability cuts.

| Type of events | Prob. cut. | Fraction excluded | Calculation method for "$N_a/N_T$". |
|---|---|---|---|
| 1.65 GeV/c | | | |
| 1-constraint | 5% | 5% | $N_a \times 1.05 \div N_T$(total) |
| 4-c.(collision) | 1% | 11% | $N_a \div N_T(>1\%)$ |
| 4-c. (tau decay) | 1% | 11% | Total = 273(265)<br>No. with prob. >1% = 243(235) |
| 1.45 GeV/c | | | |
| 1-constraint | 5% | 2.5% | $N_a \times 1.025 \div N_T(>1\%) \times 1.06$ |
| 4-c.(collision) | 1% | 0.5% | $N_a \times 1.005 \div N_T(>1\%) \times 1.06$ |
| 4-c. (tau decay) | 1% | 6% | Estimated total = 715<br>No. with prob. >1% = 675 |

* No. of tau events in brackets are those remaining after application of a beam entry cut.

## 6.3 The Glauber correction.

Glauber has shown[53] that the effective cross-section of a nucleon bound in a deuteron is reduced by a shadowing effect. This can be approximated by:

$$\sigma_d = \sigma_n + \sigma_p - \sigma_G \qquad (6.12$$

where

$$\sigma_G = \frac{1}{4\pi} \left\langle r^{-2} \right\rangle \cdot \sigma_p \cdot \sigma_n \qquad (6.13$$

Each $\sigma$ is a total "true" cross-section, and $\left\langle r^{-2} \right\rangle$ is the average inverse-square separation of the nucleons in the deuteron.

Thus the apparent neutron cross-sections measured in deuterium

must be increased. Equations 6.12 and 6.13 apply exactly for elastic scattering (from which the total cross-section relations are derived by use of the optical theorem, and by assuming purely imaginary amplitudes). For inelastic reactions, the equations are not valid, but the approximation:

$$\sigma_a = \sigma'_a \left( 1 + \frac{\sigma_G}{\sigma_d} \right) \qquad (6.14$$

may be used , where $\sigma'_a$ is the measured inelastic cross-section $\sigma_a$ the corrected value, and $\sigma_d$ is the total cross-section.

Several groups [54) 55) 56)] have used $\pi p$ and $\pi d$ total cross-sections and assumed charge independence to calculate $\langle r^{-2} \rangle$, obtaining values of 0.024, 0.042 and 0.020 $mb.^{-1}$ respectively. Carter et al[56)], found a systematic variation of $\langle r^{-2} \rangle$ with energy, which corresponded to variation in the total cross-section, and suggested a failure of the Glauber theory; but the effect is probably due to their omission of the flux factor in the unfolding of the target nucleon Fermi motion. Fäldt and Ericson[57)] point out other possible systematic errors in reference 56. Therefore $\langle r^{-2} \rangle$ is chosen to be 0.034 $mb.^{-1}$, the value obtained from the deuteron wave function (equation 4.1).

Table 6.8 shows the values of $\sigma_G$ calculated from equation 6.13, using the $\bar{K}N$ cross-section values given by Bugg et al.[58)], which are also given in the table. It should be noticed that those cross-sections do not satisfy equation 6.8, since Bugg et al. used a value of $\langle r^{-2} \rangle = .029 mb^{-1}$ to calculate $\sigma n$. However, since the correction is small, no further adjust-

Table 6.8 Glauber correction, total cross-sections, and correction factor.

| Incident $K^-$ beam momentum (GeV/c) | $\sigma_d$ (mb) | $\sigma_p$ (mb) | $\sigma_n$ (mb) | $\sigma_G$ (mb) | $(1+\frac{\sigma_G}{\sigma_d})$ |
|---|---|---|---|---|---|
| 1.45 | 59.1 | 32.5 | 29.3 | 2.6 | 1.04 |
| 1.65 | 58.0 | 34.0 | 26.0 | 2.4 | 1.04 |

ment is necessary. The probable error in $\sigma_G$ is 15%, and the resulting uncertainty in the correction is 0.6%, which is negligible compared to the other errors.

## 6.4 The assignment of fast spectator events.

Events with a "spectator" proton faster than 300 MeV/c need special study, since the majority involve multiple scattering in the deuteron (section 4.3). Since these multiple scattering processes can be inelastic, they can cause the apparent transfer of events from one reaction to another, and correction must be made for this effect.

Two reactions are considered in detail to illustrate the general principles of the correction. Only two-body secondary interactions producing two outgoing stable particles are included, and $\bar{K}n \rightarrow \Xi$ K interactions are omitted because of their low cross-sections. It will be seen that for this simple type of secondary interaction the $\pi$ -nucleon, nucleon-nucleon, and hyperon-nucleon interactions, even if inelastic, all produce a nucleon in the final state and so can be reversed by similar secondary interactions. The $\bar{K}$ -nucleon interactions however, can produce a hyperon and a $\pi$, and cannot be reversed in this way. Thus in general, reactions producing kaons will suffer a net loss of events from secondary interactions. By similar arguments, it can be shown that reactions producing two identical particles will tend to suffer a net loss of events.

In the reactions below, the spectator is enclosed in brackets in the initial state, and the spectator and the recoil particle that interacts with it are bracketed in the final state.

Firstly, for $K^-n(p) \rightarrow pK^-\pi^-p$, the possible secondary interactions are:

$$K^-n(p) \rightarrow K^-\pi^-(pp) \rightarrow K^-\pi^-pp \qquad (6.15a$$

$$\rightarrow p\pi^-(K^-p) \rightarrow p\pi^-K^-p \qquad (\quad b$$

$$\rightarrow p\pi^-\bar{K}^0n \qquad (\quad c$$

$$\rightarrow p\pi^-\Lambda^0\pi^0 \qquad (\quad d$$

$$\longrightarrow p\pi^- \Sigma^{\pm}\pi^{\mp} \qquad (6.15e, f$$

$$\longrightarrow p\pi^- \Sigma^0\pi^0 \qquad ( \quad g$$

$$\longrightarrow pK^-(\pi^-p) \longrightarrow pK^-\pi^-p \qquad ( \quad h$$

$$\longrightarrow pK^-\pi^0n \qquad ( \quad i$$

Of these, six processes will deplete the initial reaction, while the following two will augment it:

$$K^-p(n) \longrightarrow pK^-(\pi^0n) \longrightarrow pK^-\pi^-p \qquad (6.15j$$

$$K^-p(n) \longrightarrow p\pi^-(\bar{K}^0n) \longrightarrow p\pi^-K^-p \qquad ( \quad k$$

Secondly, consider the reaction $K^-n(p) \longrightarrow \Lambda^0\pi^-\pi^0p$; the possible secondary interactions are:

$$K^-n(p) \rightarrow \pi^-\pi^0 \ (\Lambda^0p) \rightarrow \pi^-\pi^0\Lambda^0p \qquad (6.16a$$

$$\longrightarrow \pi^-\pi^0\Sigma^0p \qquad ( \quad b$$

$$\longrightarrow \pi^-\pi^0\Sigma^+n \qquad ( \quad c$$

$$\rightarrow \Lambda^0\pi^0 \ (\pi^-p) \longrightarrow \Lambda^0\pi^0\pi^-p \qquad ( \quad d$$

$$\longrightarrow \Lambda^0\pi^0\pi^0n \qquad ( \quad e$$

$$\longrightarrow \Lambda^0\pi^- \ (\pi^0p) \rightarrow \Lambda^0\pi^-\pi^0p \qquad ( \quad f$$

$$\longrightarrow \Lambda^0\pi^-\pi^+n \qquad ( \quad g$$

Four of these deplete the initial reaction. Conversely, eight processes augment the initial reaction:

$$K^-n(p) \rightarrow \pi^-\pi^0(\Sigma^0p) \rightarrow \pi^-\pi^0\Lambda^0p \qquad (6.16h$$

$$K^-n(p) \rightarrow \pi^-\pi^0(\Sigma^+n) \rightarrow \pi^-\pi^0\Lambda^0p \qquad ( \quad i$$

$$K^-p(n) \rightarrow \Lambda^0\pi^0(\pi^0n) \longrightarrow \Lambda^0\pi^0\pi^-p \quad (2 \text{ possibilities}) \quad (6.16j, k$$

$$K^-p(n) \rightarrow \Lambda^0\pi^-(\pi^+n) \longrightarrow \Lambda^0\pi^-\pi^0p \qquad (6.16l$$

$$K^-n(p) \rightarrow p\pi^-(K^-p) \longrightarrow p\pi^-\Lambda^0\pi^0 \qquad ( \quad m$$

$$K^-p(n) \rightarrow p\pi^0(K^-n) \longrightarrow p\pi^0\Lambda^0\pi^- \qquad ( \quad n$$

$$K^-p(n) \rightarrow p\pi^-(\bar{K}^0n) \longrightarrow p\pi^-\Lambda^0\pi^0 \qquad ( \quad o$$

The secondary interactions that are not balanced by other interactions are, for reaction 6.15, four $K^-p$ interactions (d, e, f and g) that deplete the channel; and for reaction 6.16, three $\bar{K}N$ interactions (m, n and o) and interaction j/k, that all feed the channel. (The latter is a special

case, where a final state involving two identical pions can suffer a net depletion).

A comparison of the net number of incoming secondary interactions with the fraction of fast "spectator" events for some common reactions is given in table 6.9. There is a correlation, but not an exact one. This is partly because the inelastic secondary interactions have different cross-sections. For the inelastic meson-baryon processes considered, the average cross-section for an incident momentum of 500-1500 MeV/c ranges from 2.5 mb for $\bar{K}^- p \rightarrow \Lambda^0 \pi^0$ to 25 mb for $\pi^- p \rightarrow \pi^0 n$ [59]. The inelastic hyperon-nucleon cross-sections are quite unknown, but this is not important for this problem, because such processes are approximately balanced by the reversed processes. Elastic cross-sections are generally several times larger, ranging from an average of 15 mb for $\pi^- p$ to 40mb for $\pi^+ p$. Also other complications exist: some of cross-sections for meson-baryon secondary interactions are also unknown; each cross-section has to be integrated over the momentum spectrum of the recoil particle involved; allowance has to be made for the different cross-sections for the primary interactions; and

Table 6.9 Secondary interactions.

| Reaction | Net no. of incoming processes | % of events with "spectator" proton faster than 300 MeV/c |
|---|---|---|
| $\Lambda^0 \pi^- p$ | +1 | 19.0 ± 2.5 |
| $\Sigma^0 \pi^- p$ | +1 | 16.3 ± 3.8 |
| $\Sigma^- \pi^0 p$ | +1 | 21.5 ± 4.0 |
| $p K^- \pi^- p$ | -4 | 8.2 ± 1.1 |
| $n \bar{K}^0 \pi^- p$ | -3 | 8.1 ± 1.6 |
| $\Lambda^0 \pi^- \pi^0 p$ | +4 | 20.8 ± 1.5 |
| $\Sigma^- \pi^+ \pi^- p$ | +2 | 23.2 ± 2.8 |
| $\Sigma^+ \pi^- \pi^- p$ | +1 | 14.9 ± 2.8 |

lastly multi-body secondary interactions may occur. Because of these difficulties, a more thorough analysis is not attempted here.

However, from the evidence above, it seems reasonable to assume that the fraction of events that undergo multiple scattering in the deuteron is the same for all reactions, and that variation in the observed fraction of multiply-scattered events is caused by the inelastic multiple-scattering processes. The average fraction of fast "spectator" events has been calculated for all events in common reactions[60], and this value is used to correct cross-sections for all reactions. The results are shown in table 6.10. The statistical error in the total number of fast spectator events, results in an error of about 1% for both correction factors.

## 6.5 Error calculations.

The final cross-section, calculated according to equation 6.6 is a product of various factors, and so the final fractional error is calculated from the fraction errors on the factors according to equation 6.17. Then the final absolute error, given in the last column of tables 6.1 and 6.2, can be calculated.

$$E^2(\text{total}) = \frac{1}{N_a} + \frac{1}{N_T} + E^2(\text{ambiguities}) + E^2(\Sigma^{\pm}\ \text{weights}) + E^2(\text{unseen spectators correction}) + (0.1)^2 + E^2(F) \qquad (6.17$$

Table 6.10 Average fraction of events with fast "spectator" proton.

| | % of total events | | Correction factor |
|---|---|---|---|
| | i) faster than 280 MeV/c | ii) faster than 300 MeV/c | |
| 1.65 GeV/c run | - | 13. | 1.15 |
| 1.45 GeV/c run | 9. | - | 1.10 |

The first two terms are the statistical errors in the numbers of events for reaction a and for tau decays; $(N_a)^{-\frac{1}{2}}$ varies from 3% (900 events) to 100% (1 event) and $(N_T)^{-\frac{1}{2}}$ is 6.2% for 1.65 GeV/c taus and 5% for 1.45 GeV/c taus.

The errors in the correction factors are small except for the three factors specified in equation 6.17. The uncertainty in the assignment of ambiguities is about 7% for all reactions with a large fraction of ambiguities, that is the reactions discussed in section 6.2.2; it is negligible for other reactions. The weighting procedure itself does not add to the final fractional error, except for the weighting for losses of small-angle $\Sigma^{\pm}$ decays, where an uncertainty of 30% in the values of $\alpha$ used in equation 5.24 results in an extra 2% uncertainty for reactions with $\Sigma^{\pm} \rightarrow n\,\pi^{\pm}$ decays, and an extra 10% for reactions with $\Sigma^{+} \rightarrow p\pi^{o}$ decays. The fractional error in the correction factor for unfittable unseen spectator events is 7.5%, as stated in section 6.2.8.

The errors on the other correction factors range from $\frac{1}{2}$ - 2%, and are taken account of by adding $(10\%)^2$ to the squared error total.

The error in the calculation of F is given in section 6.1, and is about 2% for the 1.45 GeV/c and 1.65 GeV/c runs.

## 6.6 Checks on the reliability of the results.

Checks can be made by using known branching ratios for the decays of charged and neutral particles, and from the principle of charge independence.

Reactions involving $\bar{K}^{o}$ or $\Lambda^{o}$ particles can lead to different event topologies, depending on whether the neutral decay is seen or not; for example $p\bar{K}^{o}\pi^{-}\pi^{-}$, $\Lambda^{o}\pi^{+}\pi^{-}\pi^{-}$ and $\Sigma^{o}\pi^{+}\pi^{-}\pi^{-}$ are all fittable in the 300 and 301 topologies. After correction for the relevant branching ratios, the 300 events give up to three times higher cross-sections than do the

301 events. This is because the 300 events give only one-constraint fits, and possess no decay identification signature; they therefore not only suffer from ambiguities, but also from considerable contamination. (The same may be true of the $pK^-\pi^-\pi^0$, and $nK^-\pi^+\pi^-$ channels).

In the channels involving $\Sigma^+$ particles, comparisons of the cross-sections obtained for the $\Sigma^+ \rightarrow p\pi^0$ and $\Sigma^+ \rightarrow n\pi^+$ decays are possible. At both beam momenta, results agree within two standard deviations and show no systematic effects. This confirms the reliability of the decay weighting method, for Imperial College events alone (the results of section 5.3 demonstrate this reliability for the collaboration data).

Since the $K^-n$ system is a pure isospin state, charge independence yields definite ratios for two-body cross-sections; for example, $\sigma(K^-n \rightarrow \Sigma^0\pi^-) = \sigma(K^-n \rightarrow \Sigma^-\pi^0)$. Moreover, $\sigma(K^-n \rightarrow \Lambda^0\pi^-) = 2\,\sigma(K^-p \rightarrow \Lambda^0\pi^0)$, since the reaction is pure isospin one even for a proton target. Table 6.11 shows the results of such comparisons. The agreement is excellent, except for the $\Sigma\pi$ cross-sections at 1.65 GeV/c. The discrepancy here is only two standard deviations, and might reflect wrong assignments of $\Lambda^0/\Sigma^0$ ambiguities.

Table 6.11 Experimental check of charge independence predictions.

| | Cross-sections (mb) | |
|---|---|---|
| | 1.45 GeV/c | 1.65 GeV/c |
| $K^-n \rightarrow \Sigma^0\pi^-$ | $0.70 \pm .19$ | $0.83 \pm .22$ |
| $K^-n \rightarrow \Sigma^-\pi^0$ | $0.83 \pm .13$ | $0.33 \pm .10$ |
| Difference | $0.13 \pm .23$ | $-0.50 \pm .24$ |
| $K^-n \rightarrow \Lambda^0\pi^-$ | $2.30 \pm .25$ | $1.91 \pm .24$ |
| $2x\ (K^-p \rightarrow \Lambda^0\pi^0)$ | $2.34 \pm .12$ | $1.93 \pm .11$ |
| Difference | $0.04 \pm .28$ | $0.02 \pm .26$ |

## 6.7 Cross-sections for three-body reactions, using all available collaboration data.

Cross-section values for most of the reactions in tables 6.1 and 6.2 are available at 1.45 GeV/c from our Birmingham University collaborators,[61] and 1.65 GeV/c from all collaborating groups[62) 63) 64)]. Comparisons are shown in table 6.12, for the combined cross-section of nine common reactions ($\Lambda^0\pi^-$, $\Sigma^0\pi^-$, $pK^-\pi^-$, $n\bar{K}^0\pi^-$, $\Lambda^0\pi^-\pi^0$, $\Sigma^{\mp}\pi^{\pm}\pi^-\pi^0$, and $\Sigma^{\mp}\pi^{\pm}\pi^-$) ; the errors quoted are those from the tau count, which are dominant. The agreement is good, except for the Edinburgh results, which seem definitely high.

The average of the cross-sections for all fittable three-body reactions was then made, using all available data except that from Edinburgh University, and the results are shown in table 6.13. Out of 21 comparisons, four disagreements of more than two standard deviations are seen. Three of these are for the $\Sigma^+\pi^-\pi^-$ reaction and it is possible that uncertainties in the $\Sigma^+$ decay weighting method are responsible; but in previous checks this method was shown to be reliable, and it was therefore assumed that the averages are useful.

## 6.8 Cross-sections for resonance production in three-body reactions.

The contributions of various final state resonances to the three-

---

Table 6.12 Combined cross-sections for 9 common reactions from different groups. (see above).

| | London (I.C.) | Birmingham | Edinburgh | Glasgow |
|---|---|---|---|---|
| 1.45 GeV/c | | | | |
| $\sigma$(mb) | 11.94 ± .45 | 12.21 ± .39 | - | - |
| Difference | - | 0.27 ± .60 | | |
| 1.65 GeV/c | | | | |
| $\sigma$(mb) | 13.05 ± .84 | 13.02 ± .69 | 15.66 ± 1.2 | 11.60 ± .62 |
| Difference | - | -0.03 ± 1.0 | 2.61 ± 1.4 | -1.45 ± 1.0 |

Table 6.13 Cross-sections in millibarns for all fittable three-body reactions.

| Beam momentum = 1.45 GeV/c | Birmingham | London | Average |
|---|---|---|---|
| $pK^-\pi^-$ | 1.50 ± .10 | 1.19 ± .09 | 1.33 ± .07 * |
| $n\bar{K}^0\pi^-$ | 2.86 ± .21 | 2.78 ± .23 | 2.82 ± .16 |
| $\Lambda^0\pi^-\pi^0$ | 3.56 ± .25 | 3.34 ± .25 | 3.45 ± .18 |
| $\Sigma^-\pi^+\pi^-$ | 0.76 ± .06 | 0.65 ± .06 | 0.70 ± .04 |
| $\Sigma^+_p\pi^-\pi^-$ | 1.0 ± .10 | 0.63 ± .12 | 0.85 ± .077 * |
| $\Sigma^+_n\pi^-\pi^-$ | 1.06 ± .10 | 0.58 ± .08 | 0.77 ± .063 * |
| Av. $\Sigma^+\pi^-\pi^-$ | - | - | 0.80 ± .050 |

| Beam momentum = 1.65 GeV/c | Birmingham | Glasgow | London | Average |
|---|---|---|---|---|
| $pK^-\pi^-$ | 2.05 ± .17 | 1.80 ± .15 | 1.68 ± .16 | 1.84 ± .09 |
| $n\bar{K}^0\pi^-$ | 3.16 ± .30 | 3.25 ± .31 | 3.70 ± .62 | 3.26 ± .20 |
| $\Lambda^0\pi^-\pi^0$ | 3.16 ± .27 | 3.00 ± .26 | 3.08 ± .46 | 3.07 ± .17 |
| $\Sigma^-\pi^+\pi^-$ | 0.81 ± .08 | 0.66 ± .07 | 0.65 ± .09 | 0.70 ± .04 |
| $\Sigma^+\pi^-\pi^-$ | 0.70 ± .07 | 0.52 ± .05 | 0.85 ± .10 | 0.62 ± .04 * |

* indicates reactions involving disagreements of more than two standard deviations.

body reactions has been obtained by our Birmingham University collaborators,[62] by fitting to the distribution of events on the Dahlitz plot, using a maximum likelihood method. Table 6.14 shows these results. Non-interfering phase space and resonant amplitudes were assumed, and for the resonances, a Breit-Wigner shape with energy-dependent width was used. Checks on these results were made at Imperial College, by the author, using a similar program; generally the fractions for $\Sigma(1765)$ and $\Lambda(1815)$ were larger, and the $\Sigma(1385) \rightarrow \Lambda^{o}\pi$ fractions were smaller, than those from reference 62, but otherwise no serious discrepancies were found. Also F. Heathcote of Birmingham subsequently refitted the resonance fractions[64a], and obtained significant differences in the resonance fractions for the $\Sigma(1385)\pi \rightarrow \Lambda^{o}\pi\pi$ reaction (which agreed with the Imperial College results), and for $K^{*}(890)n$ and $\rho^{-}\Lambda^{o}$; these fractions have been used in table 6.14.

Figure 6.3 shows the two-body effective mass distributions and fitted curves for combinations that involve Y* resonances (taken from reference 62), and for the $\pi^{-}\pi^{o}$ combination; the latter was obtained at Imperial College, using the resonance fractions of reference 62 for the fitted curve. All resonance masses and widths were fixed at accepted values, or at values fixed in preliminary fits; one exception was the "$\Sigma(1680)$" resonance, which was allowed variable mass and width. For this resonance, the fitted mass and width varied over a range of 50 MeV and 30 MeV respectively, for different reactions; this was acceptable because there are in fact two $\Sigma$ and two $\Lambda$ resonances in this mass region, which may be present in different proportions in different reactions.

Events with both seen and unseen spectator protons slower than 280 MeV/c were used for all plots. This may be a somewhat questionable procedure for the one-constraint reactions $\Lambda^{o}\pi^{-}\pi^{o}$ and $n\bar{K}^{o}\pi^{-}$, where the unseen spectator events are not very reliably fitted. However, it is believed that

| Reaction | Beam momentum (GeV/c) | $K^*(890)$ | $\rho(750)$ | $N^*(1236)$ | $\Sigma^-(1385)$ | $\Sigma^0(1385)$ | $\Lambda(1405)$ | $\Lambda(1520)$ | $\Sigma^-(1680)$ | $\Sigma^0(1680)$ | $\Sigma^-(1770)$ | $\Sigma^0(1770)$ | $\Lambda(1815)$ |
|---|---|---|---|---|---|---|---|---|---|---|---|---|---|
| $\Lambda^0\pi^-\bar{\pi}^0$ | 1.45 | | 24±2* | | 22±1* | 26±1* | | | 4±1 | 0±1 | 0±1 | 0±1 | |
| | 1.65 | | 37±2* | | 12±1* | 15±1* | | | 4±1 | 3±1 | 0±1 | 2±1 | |
| $\Sigma^-\pi^+\pi^-$ | 1.45 | | 18±2 | | | 5±1 | 14±2 | 29±2 | | 23±2 | | | |
| | 1.65 | | 17±2 | | | 2±1 | 12±2 | 33±4 | | 25±4 | | | |
| $\Sigma^+\pi^-\pi^-$ | 1.45 | | | | | 6±1 | 24±2 | 31±2 | | 21±2 | | | |
| | 1.65 | | | | | 13±3 | 15±3 | 32±4 | | 29±4 | | | |
| $\bar{K}^0n\pi^-$ | 1.45 | 40±2* | | 44±2 | | | | 8±1 | | | | | |
| | 1.65 | 39±2* | | 43±3 | | | | 6±2 | | | | | |
| $K^-p\pi^-$ | 1.45 | | | 7±1 | | | | 29±2 | | | | 6±1 | 9±1 |
| | 1.65 | | | 6±1 | | | | 20±2 | | | | 3±1 | 15±2 |

Table 6.14 Fitted resonance percentages. (* indicates results from reference 64a)

the identification of the reaction is reliable (chapter 4), and where the effective masses in question do not involve an unseen neutral particle, they should also be reliable. Thus it is seen from table 6.14 that the $\Sigma(1385)$ fractions in $\Lambda\pi^0$ and $\Lambda\pi^-$ are compatible, as expected from charge independence. Discussion of $\rho^-$ production in $\Lambda\pi^-\pi^0$ is deferred to chapter 7.

However, considerable problems were found in fitting the N*(1236) and $\Lambda(1520)$ production in the $n\pi^-$ and $n\bar{K}^0$ effective mass combinations; both gave large chi-squared values for the best fitted curves (not shown in figure 6.3a). This was mainly caused by a general excess of events at high $\bar{K}^0n$ effective masses, which in turn appeared to be produced by events with unseen spectator protons, especially those with the spectator azimuth approximately vertical[65]. These are precisely the events for which the spectator proton and unseen neutral particle are most inaccurately fitted, according to the discussion of section 4.5. Therefore the results for the $\bar{K}^0n$ and $n\pi^-$ combinations should be used with care.

The results of tables 6.13 and 6.14 have been used to calculate (table 6.15) the cross-sections for all quasi-two body reactions identified, except for the $\Sigma(1680)$ and Y* resonances of higher mass. These values are used in chapter 7 to calculate the variation of cross-section with centre of mass energy. Also in table 6.15 the predictions of the SU(2) Clebsch-Gordan coefficients are compared with the results. The serious disagreements for the $\Lambda(1520)$ decays to $\bar{K}N$ and the less serious disagreements for the N*(1236) decays are probably caused by the use of unseen spectator events for the $n\bar{K}^0\pi^-$ reaction, which is discussed above.

Disagreement is also seen for the $\Lambda(1405)$ decays to $\Sigma^{\pm}\pi^{\mp}$ at 1.45 GeV/c; this could be linked to the disagreement over $\Sigma^+\pi^-\pi^-$ cross-sections at 1.45 GeV/c already seen in table 6.13, and this suggests that the lower

Table 6.15 Cross-sections for some quasi two-body final states.

| Reaction | Final state | Exp'd ratio | 1.45 GeV/c σ (mb) | 1.45 GeV/c Calc. ratio | 1.65 GeV/c σ(mb) | 1.65 GeV/c Calc. ratio |
|---|---|---|---|---|---|---|
| $K^*(890)^-n$ | $(\bar{K}^0\pi^-)n$ | - | 1.13±.08 | - | 1.27±.11 | - |
| $N^*(1236)\bar{K}$ | $(n\pi^-)\bar{K}^0$ | 9.0 | 1.24±.08 | 13.3±2.3 | 1.40±.13 | 12.7±2.5 |
| | $(p\pi^-)K^-$ | | .093±.014 | | .11±.02 | |
| | | | Δ = | +4.3±2.3 | Δ = | +3.7±2.5 |
| $\Lambda(1520)\pi^-$ | $(n\bar{K}^0)\pi^-$ | 1.0 | 0.23±.03 | 0.59±.10 | 0.20±.07 | 0.54±.19 |
| | $(pK^-)\pi^-$ | | 0.39±.03 | | 0.37±.04 | |
| | | | Δ = | -.41±.10* | Δ = | -.46±.19* |
| | $(\Sigma^-\pi^+)\pi^-$ | 1.0 | 0.20 ±.02 | 0.82±.10 | 0.23±.03 | 1.15±.21 |
| | $(\Sigma^+\pi^-)\pi^-$ | | 0.25±.02 | | 0.20±.03 | |
| | | | Δ = | -.18±.10 | Δ = | +.15±.21 |
| $\Sigma(1385)\pi$ | $(\Lambda^0\pi^-)\pi^0$ | 1.0 | 0.76±.05 | 0.85±.04 | 0.37±.04 | 0.80±.10 |
| | $(\Lambda^0\pi^0)\pi^-$ | | 0.90±.06 | | 0.46±.04 | |
| | | | Δ = | -.15±.08 | Δ = | -.20±.10 |
| $\rho^-\Lambda^0$ | $(\pi^-\pi^0)\Lambda^0$ | - | 0.83±.08 | - | 1.14±.09 | - |
| $\Lambda(1405)\pi^-$ | $(\Sigma^-\pi^+)\pi^-$ | 1.0 | 0.10±.015 | 0.52±.11 | .084±.015 | 0.90±.24 |
| | $(\Sigma^+\pi^-)\pi^-$ | | 0.19±.03 | | .093±.020 | |
| | | | Δ = | -.48±.11* | Δ = | -.10±.24 |
| $\rho^0\Sigma^-$ | $(\pi^+\pi^-)\Sigma^-$ | - | 0.13±.02 | - | 0.12±.02 | - |

* marks disagreements larger than two standard deviations.

value, obtained by Imperial College is probably correct. However, for the $\Lambda(1520)$ and $\Lambda(1405)$ calculations in chapter 7, the $\Sigma^+\pi^-\pi^-$ and $\Sigma^-\pi^+\pi^-$ results have both been used.

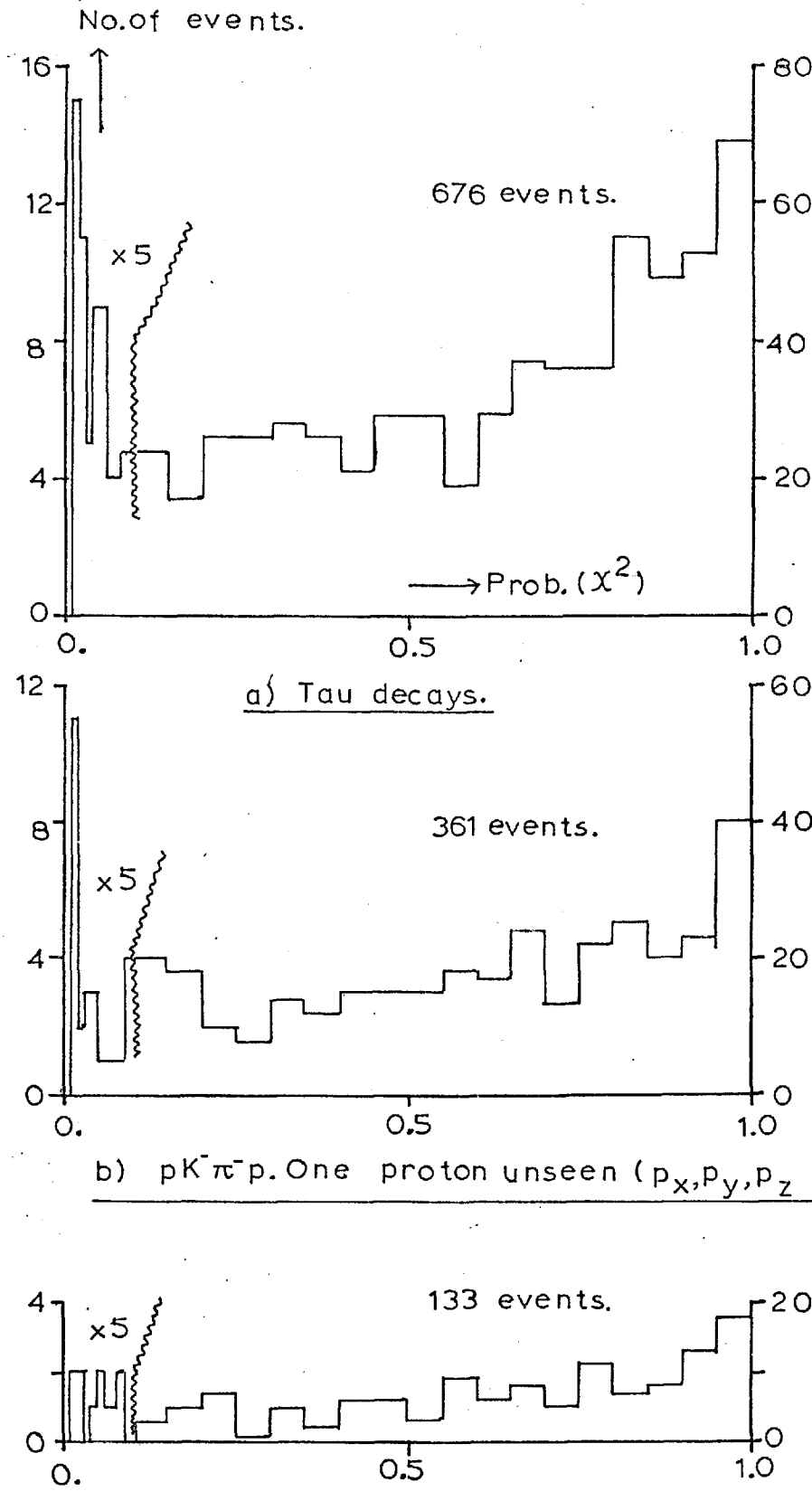


FIGURE 6.1 PROBABILITY DISTRIBUTIONS FOR I.C. 1.45 GEV/C DATA, 4-CONST-RAINT FITS.

Note: these results are for 4-constraint multivertex fits; and are similar to those for the corresponding 1-constraint production vertex fits.

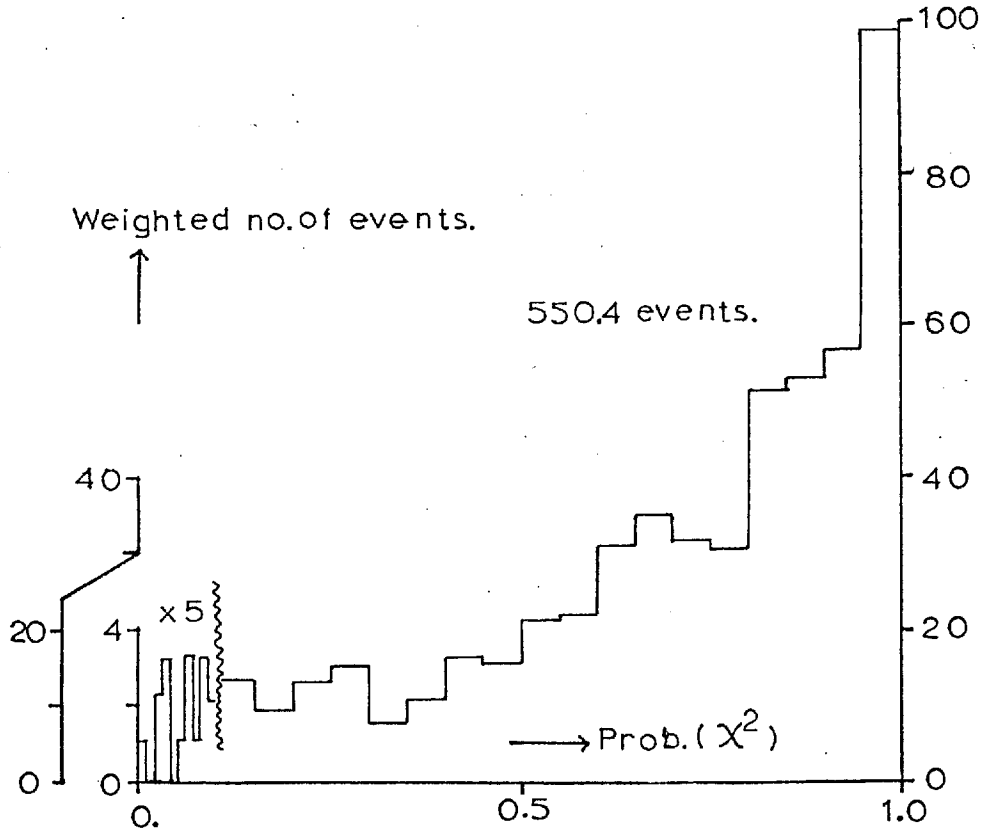


a) $\Lambda^\circ\pi^-\pi^\circ p$. Unseen proton ($p_x, p_y, p_z$ fits).
$\hookrightarrow p\pi^-$

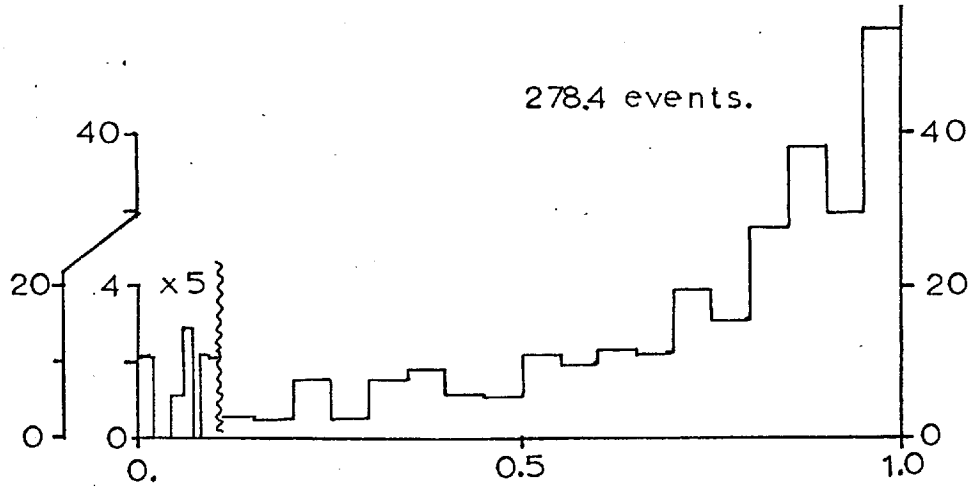


b) $\Lambda^\circ\pi^-\pi^\circ p$. Seen proton, <280 MeV/c.
$\hookrightarrow p\pi^-$

FIGURE 6.2 PROBABILITY DISTRIBUTION FOR I.C. DATA, 1·45 GEV/C, 1-CONSTRAINT FITS.

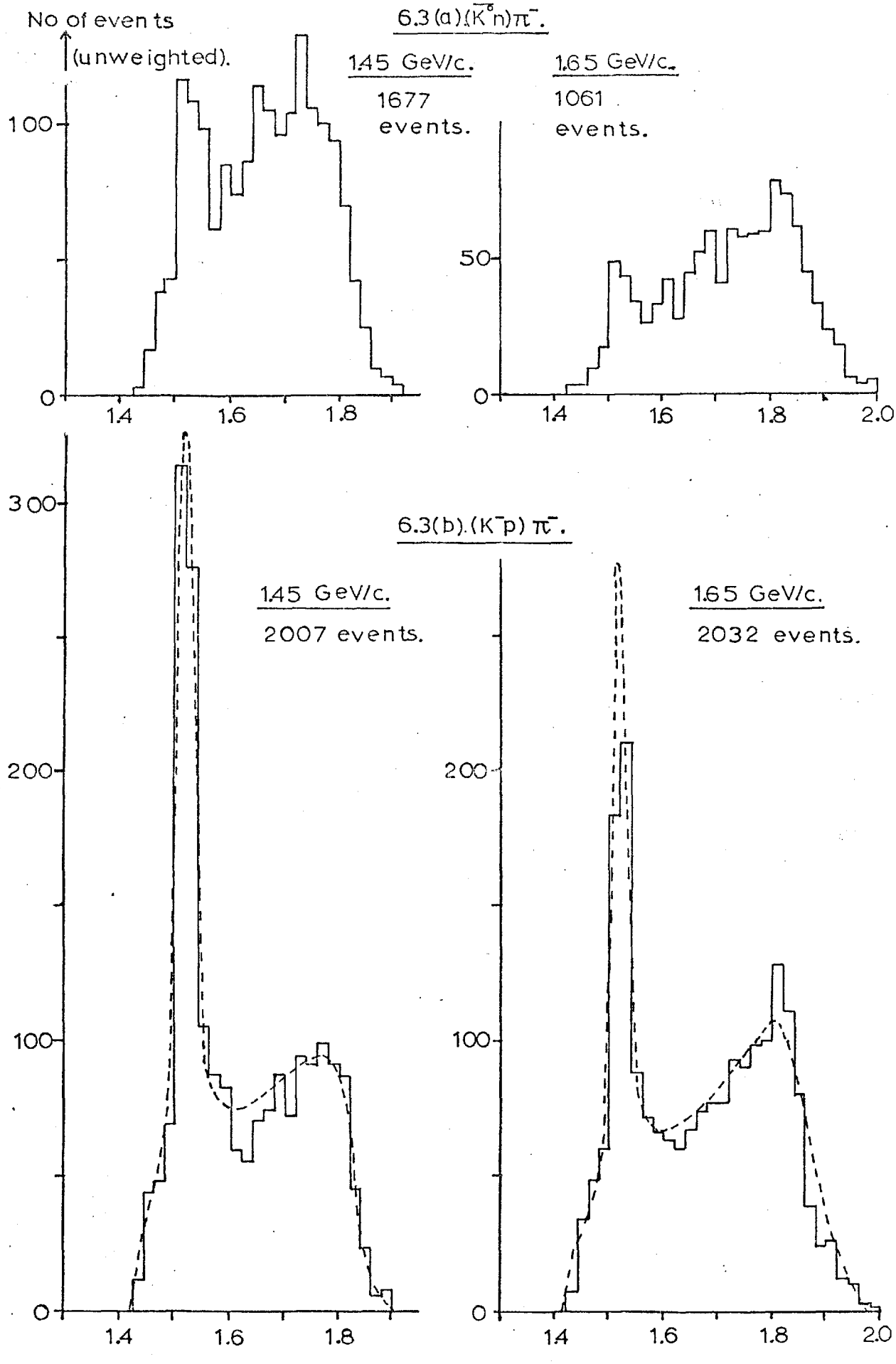


FIGURE 6.3 SOME EFFECTIVE MASSES (IN GEV/C) FOR 3-BODY FINAL STATES.

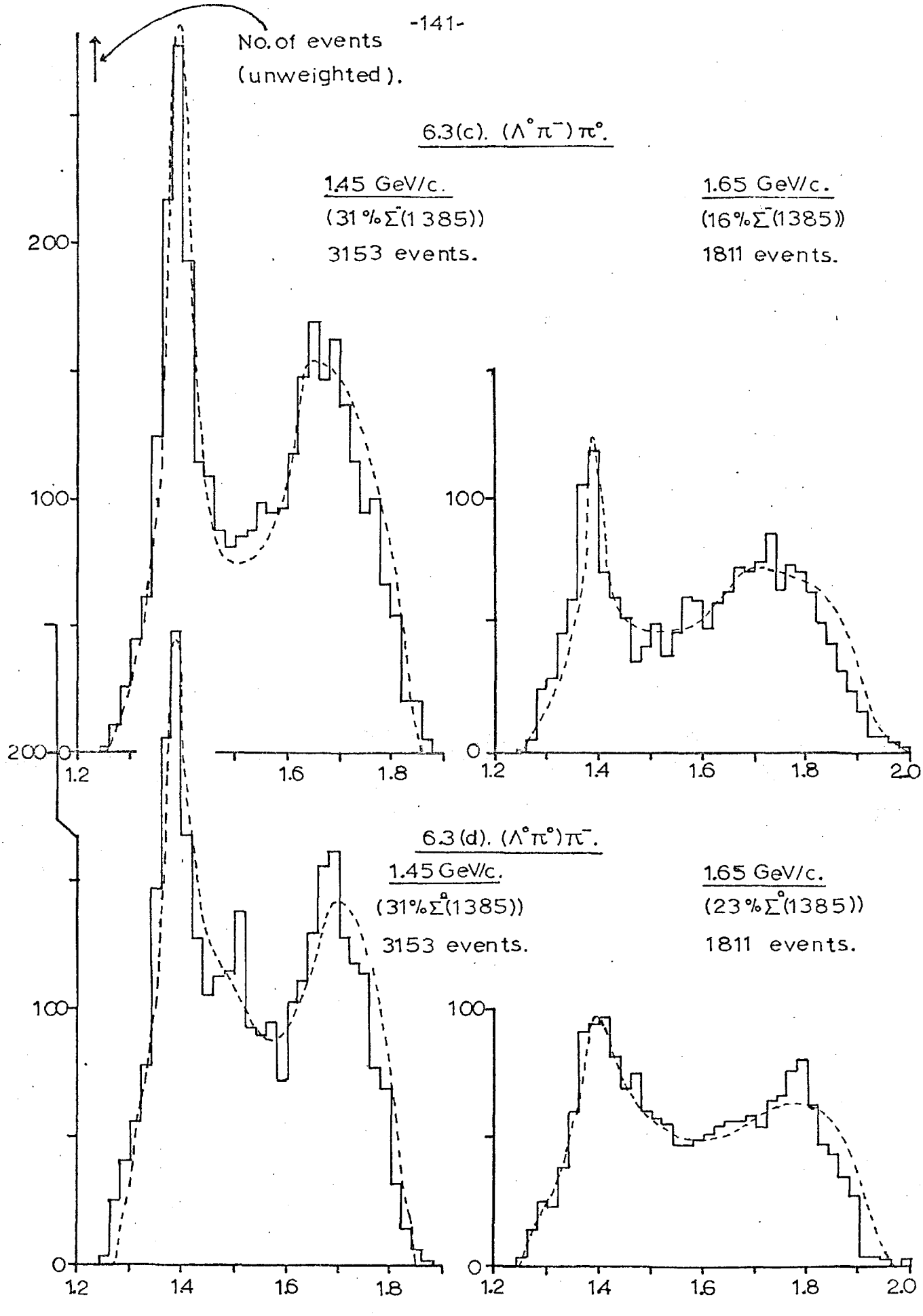


FIGURE 6.3 (c) and (d).

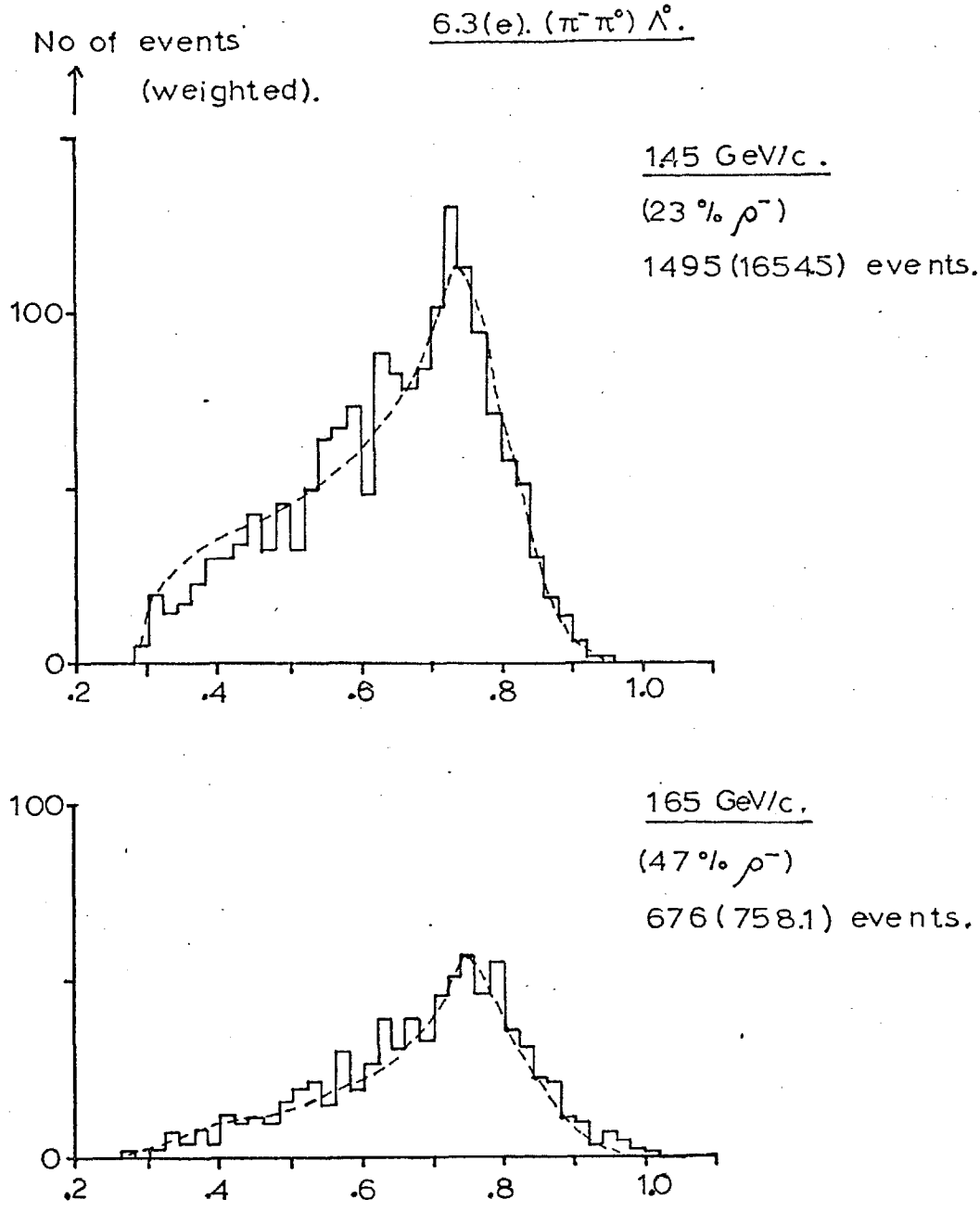
6.3(e). $(\pi^-\pi^0)\Lambda^0$.
No of events
(weighted).
1.45 GeV/c.
(23 % $\rho^-$)
1495 (16545) events.
100
0
.2
.4
.6
.8
1.0
165 GeV/c.
(47 % $\rho^-$)
676 (758.1) events.
100
0
.2
.4
.6
.8
1.0

FIGURE 6.3(e).

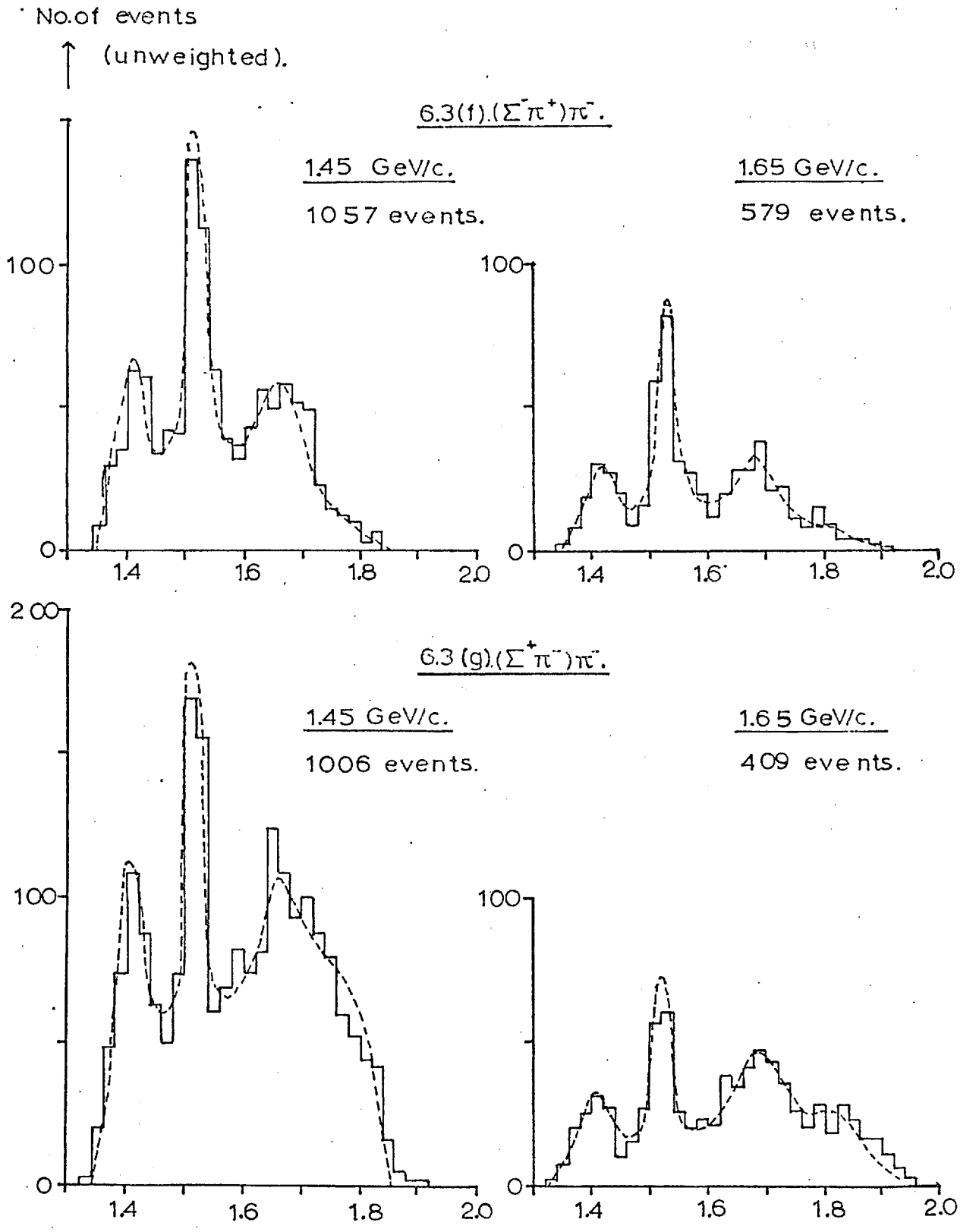


FIGURE 6.3(f) and (g).

## CHAPTER 7 Variation of cross-section with centre of mass energy

### 7.1 Calculation method.

The Fermi motion of the proton and neutron in the deuterium nucleus results in a widening of the range of centre of mass energy observed in collisions on either nucleon. For this experiment, a beam momentum spread of full width 2% (about 30 MeV/c) would lead to an energy spread of about 15 MeV; but with the inclusion of the Fermi motion of the target, the energy spread is about 180 MeV (see figure 7.1). Thus the variation of cross-section with energy can be studied over a wide energy range.

The method used is to calculate, on the assumption of a constant cross-section, the expected number of events in different energy intervals; this is compared with the actual number of events observed, for a selected channel, or group of channels. The relevant program was written at Imperial College by F. Fuchs [66], and takes account of the Fermi motion of the target (equation 4.2), the flux factor (equation 4.12), and the distribution of beam momentum. Figure 7.1 shows the results of this program for the distribution of the expected number of events; results for the two different beam momentum values are plotted separately.

The data is divided into 20 MeV intervals, and the actual number of events is divided by the expected number and a "reduced" cross-section is calculated, which is normalised to have an average value of 1.0 for an energy range of 1980-2080 MeV.

Events from the two beam momentum runs are used separately, and their results are then averaged. From the ratio of the mean reduced cross-sections for each run, the correct scaling factor can be obtained from the actual cross-sections, and also the consistency of the actual cross-sections can be examined; the

calculated ratio and the experimental ratio of cross-sections should be equal.

The values used for the beam momenta were 1445 and 1640 MeV/c. These were less than the values of 1450 and 1650 MeV/c at chamber entry (see section 3.3.7), because the average values at collision were required here and these were about 10 MeV/c less than those at chamber entry, because of energy loss. However, the missing mass studies for three-body channels (see section 5.2) indicated that the momentum value for the lower energy run was about 5 MeV/c too low. This was confirmed by the comparison of the calculated and experimental cross-sections ratios, and therefore the value of 1445 MeV/c was used.

The momentum profile was taken to be Gaussian, with a full width at half height of 38 MeV/c. The effect of the errors in the fitted spectator particle momentum and the direction, and in the fitted beam direction was taken into account in the width of the profile. This width was therefore larger than the width for the fitted beam momentum from tau decays (26 MeV/c).

The systematic errors in the calculations were investigated by changing the values of average beam momenta and beam profile width by about three times the estimated uncertainty in each. An increase in either beam momentum increased the calculated cross-sections below the central energy, and reduced the cross-sections above the central energy. (These central energies were 1997 and 2083 MeV for the 1445 and 1640 MeV/c beam momenta respectively). A change of 5MeV/c in either beam momentum had a 10% effect on cross-sections at 100 MeV above or below the central energy. An increase in the width of the beam profile of 20%, reduced the cross-sections at 100 MeV both above and below the central energy, by about 10%. Therefore the systematic errors due to wrongly estimated beam profile were much

less than 10%, for energies of 1900 to 2180 MeV.

Only events with seen spectator protons of 100 to 280 MeV/c were used for the calculations. Events with an unseen proton occupied a narrow energy range, and their results were therefore very sensitive to any inaccuracies in the beam momentum profile. Events fitted with a one constraint fit gave biased mass plots when the spectator was unseen (Section 6.8); also some computing problems were found for unseen spectator events.

The cross-sections in table 6.13 were calculated using seen and unseen spectator events; since these groups of events may have had slightly different average cross-sections, this could have introduced a small error into the overall normalisations However, this error is certainly less than the statistical errors present. It is shown in the next section that no biases are noticeable when these results are compared with those from other experiments. (Figures 7.2 to 7.13).

## 7.2 Results for the $\Sigma\pi$ channel, and for three-body and quasi two-body channels.

### 7.2.1. Introduction.

The variation of cross-section with centre of mass energy has been calculated for the above channels from the data of the present experiment, and is plotted in figures 7.2 to 7.13. The fittable three-body channels and the important quasi two-body channels contributing to them (table 6.14) have been analysed; however the $\Sigma^- \rho^0$, $\Sigma(1680)\pi$ and $\Lambda(1815)\pi$ channels have been omitted because of the large fraction of background events under their effective mass peaks.

The $\Sigma\pi$ channel is included here because it yields some results relevant to the above channels. The other two-body channels have been discussed elsewhere, but are worth a brief summary here. A partial wave analysis of the $\Lambda\pi^-$ channel[67] finds the $\Sigma(2030)$ resonance to be the dominant feature, and also finds good evidence for decay of the $F_{5/2}$ (1905) and of a $P_{3/2}$ $\Sigma$ resonance, mass about 2080 MeV, width about 80 MeV. The $\Xi K$ channel included rather few events, but a partial wave analysis showed evidence for decay of the $\Sigma(2030)$[68]. The $K^-n$ channel proved very difficult to separate from other two prong-events, but was analysed to obtain cross-sections and angular distributions[69].

Each figure includes all available data in this energy region from other $K^-n$ experiments, and from $K^-p$ experiments producing pure isospin 1 channels (e.g. $\Lambda\rho^-$ and $\Lambda(1520)\pi^-$ the $K^-p$ values are multiplied by two, to obtain equivalent $K^-n$ cross-sections. The lines drawn through the data are only guide-lines, except for two fitted curves given by other experiments. In addition to the statistical errors shown, each set of results is subject to an overall error, which is shown on the figures thus: ⊣⊢. This is the error on the factor calculated from the

experimental cross-sections, which is used to scale up the "reduced" cross-section values. Data points are only plotted when the statistical errors are less than 30% (except near threshold, for the $K^*(890)n$ and $\Lambda\rho^-$ channels).

For each quasi two-body channel, the effective mass selections used for the resonances are given in table 7.1. This table also shows the fraction of the events selected that were in fact non-resonant background. The effect of these background events was corrected for only in the $\Lambda(1520)\pi^-$ channel. This was because the $\Sigma(1385)\pi$ channel (27% background) gave a very similar cross-section variation with background subtraction (reference 70, figure 6), and without subtraction (figure 7.8); both individual points and the general variation were in good agreement. Thus a correction is unnecessary when the fraction of background is small. However the results for the $\Lambda\rho^-$ reaction (50% background) do appear to suffer from lack of background subtraction (see section 7.2.9).

For every three-body final state, the contributions of the important quasi two-body channels are shown. These are calculated by scaling the guide-lines from the relevant plots, using accepted values for branching ratios [24] and the relevant Clebsch-Gordan factors.

The results for each channel are discussed individually below.

7.2.2. $\Sigma\pi$ (Figure 7.2)

The results obtained by this experiment are taken from $\Sigma^-\pi^0$ events, and were given at the 1968 Vienna Conference [70]. These had an average cross-section in good agreement with the latest I.C. values in tables 6.1 and 6.2 and so have not been rescaled. $\Sigma^0\pi^-$ data was not used because of its possibly larger contamination, so the $\Sigma^-\pi^0$ cross-section was doubled to obtain this total $\Sigma^0\pi^0$ cross-section.

TABLE 7.1 Effective Mass selections for quasi two-body reactions, for figures 7.2 to 7.13, with fraction of background events in range selected.

| Reaction | Final states used. | Mass limits (MeV), | Fraction of background events (average for both beam momenta). (%). |
|---|---|---|---|
| $K^*(890)^- n$ | $(K^0 \pi^-) n$ | 860-920 | 20 |
| $N^*(1236)\bar{K}$ | $(n\pi^-)\bar{K}^0$<br>$(p\pi^-)K^-$ | 1160-1280 | 40<br>40 |
| $\Sigma(1385)\pi$ | $(\Lambda\pi^-)\pi^0$<br>$(\Lambda\pi^0)\pi^-$ | 1350-1420 | 27 |
| $\rho^- \Lambda$ | $(\pi^-\pi^0)\Lambda$ | 650-810 | 50 |
| $\Lambda(1405)\pi^-$ | $(\Sigma^\pm\pi^\mp)\pi^-$ | 1370-1440 | 45 |
| $\Lambda(1520)\pi^-$ | $(\Sigma^\pm\pi^\mp)\pi^-$<br>$(K^- p)\pi^-$ | 1490-1550 | 25 |

The data of R. Armenteros et al.[71] shows a clear peak at 1660 MeV, and a less clear peak at 1800 MeV, both of which correspond to known $\Sigma$ resonances; the data from this experiment show a broad peak at about 2000 MeV, corresponding to the known decay mode of the $\Sigma(2030)$ [24]. There is also a possible narrower peak at about 1970 MeV.

7.2.3. $n\bar{K}^0\pi^-$ (figure 7.3)

The total cross-section rises steadily with energy. This is unusual, and is mainly caused by the steep rise in the cross-section for $K^*(890)n$, decaying to $(\bar{K}^0\pi^-)n$. The low cross-section reported at 2330 MeV [72] suggests that there is a rapid fall in cross-section somewhere between 2170 and 2330 MeV. The small shoulders in the cross-section at about 1940 and 2070 MeV are caused by the peaks seen in the $K^*n$ and $N^*K$ distributions respectively. Studies made of this channel at Imperial College indicate that about 15% of the channel is produced from $\Sigma(1660)\pi$ and $\Lambda(1815)\pi$; the opening of these channels probably also contributes to the rise in cross-section .

7.2.4. $K^*(890)^-n$. (figure 7.4)

The results for the $(K^0\pi^-)n$ channel are plotted; there is only one other result available for this channel in this energy range, from K.F. Galloway et al. [72].

The cross-section rises from threshold, shows a peak at about 1940 MeV, of width about 50 MeV, then rises until 2170 MeV. The existence of a peak between 2170 and 2330 MeV is suggested by the low cross-section at 2330 MeV from K.F. Galloway et al..

7.2.5. $N^*(1236)\bar{K}$ . (figure 7.5)

Events from $(n\pi^-)\bar{K}^0$ and $(p\pi^-)K^-$ were used for these results. Because of the difficulties with the $(n\pi^-)\bar{K}^0$ cross-

sections (section 6.8), the ( $p\pi^-$ )$K^-$ cross sections are used to scale the reduced cross-section values and are multiplied by 12 to correct for the ( $p\pi^-$ )$K^-$ and ( $n\pi^\circ$ )$\overline{K^\circ}$ events. This means that the overall error is rather large, which is preferable to using the ( $n\pi^-$ )$\overline{K^0}$ cross-sections, which are possibly biased by unseen spectator misfitting.

A cross-section from a $K\bar{n}$ experiment [72] is plotted. The reaction $K\bar{p} \rightarrow N^*(1236)\overline{K}$ is pure isospin 1, (if isospin 2 amplitudes can be neglected), but only one cross-section is available at these energies [73]. The results of the present experiment are compatible with both these cross-sections.

The cross-section shows an initial fall, which could be connected with a $\Sigma(1765)$ decay to this channel, and then rises slowly. There is a possible shoulder at 2090 MeV. However the mass selection for this N* resonance includes about 40% background, which would tend to smooth out any structure.

7.2.6. $p K^-\pi^-$ (figure 7.6)

There is excellent agreement between the cross-sections for the present experiment, and the results quoted by A. Barbaro-Galtieri et al.[74] (for which no error was quoted).

The initial fall in cross-section is caused by the "tail" of the $\Sigma(1765)$ resonance in the s channel, for which the reaction is: $K^-n \rightarrow \Sigma(1765) \rightarrow \Lambda(1520)\pi^- \rightarrow pK^-\pi^-$ (7.1

(the $\Lambda(1520)\pi^-$ cross-section curve plotted is scaled from the results of figure 7.13).

The rise in cross-section at higher energies is probably caused by the opening of the higher $Y^*\pi$ channels; similar behaviour is seen for the $n\overline{K^\circ}\pi^-$ channel (section 7.2.3). The two shoulders seen in the $pK^-\pi^-$ cross-section at about 1980 and 2000 MeV probably correspond to the peaks seen in the $\Lambda(1520)\pi$ cross-section .

The cross-section for this channel is generally lower than that for $n\overline{K}^{\circ}\pi^{-}$, because the $K^{*}(890)$ cannot be produced in this channel.

7.2.7. $\Lambda\pi^{-}\pi^{\circ}$ (Figure 7.7)

The cross-sections for this channel from the present experiment, and from J.H. Bartley et al. are plotted [75]. A letter by W.H. Sims et al.[76] is by the same authors and presents a partial wave analysis of the same data, which is found to be produced entirely via $\Sigma(1385)\pi$ for the relevant energy range (details of this analysis are given in the next section). Reference 75 gave no fitted curve, so the fitted curve from reference 76 is used. Although the cross-sections given in both references show the same structure, those from reference 75 are slightly higher between 1665 and 1725 MeV, which causes a slight disagreement between thedata points and the curve shown in figure 7.7.

The results from the present experiment show small peaks at 1970 and 2030 MeV, which correspond to peaks in the $\Sigma(1385)\pi$ cross-sections; also the cross-section begins to rise at about 2150 MeV. The divergence between the $\Sigma(1385)\pi$ and the total $\Lambda\pi^{-}\pi^{\circ}$ cross sections increases with energy, because of the rise in the $\Lambda\rho^{-}$ cross sections from the $\Lambda\rho^{-}$ threshold at 1880 MeV.

7.2.8. $\Sigma(1385)\pi$ (Figure 7.8)

The $\Sigma^{\circ}(1385)\pi^{-}$ and $\Sigma^{-}(1385)\pi^{\circ}$ channels are equivalent and so are added together. The results of references 75 and 76 given in figure 7.7 are replotted in figure 7.8. The partial wave analysis of W.H. Sims et al.[76] shows that in the s channel, there is strong production of the $\Sigma(1765)$ resonance, and also less strong production of the $\Sigma(1660)$ and $\Sigma(1700)$ resonances. At 1765 MeV, 83% of the cross-section is attributable to the $\Sigma(1765)$. This cross-section is plotted, together with two

results for the same process obtained from $K^-p$ experiments [77,78] (corrected for isotopic spin differences) and another result obtained from the Particle Data Group's fitted $x_e.x_r$ for this $\Sigma(1765)$ decay [24].

The four cross-section values for pure s channel $\Sigma(1765)$ at 1765 MeV all agree, although the large errors seen make this not very meaningful. The total $\Sigma(1385)\pi$ cross-sections at about 1850 MeV, from the present experiment, fall below the continuation of the fitted curve from reference 76, but here again, the cross-section errors are rather large.

The cross-section from the present experiment falls as the energy increases and shows small peaks at about 1960 and 2030 MeV. The possible identification of these with resonances in the s channel will be discussed in section 7.3.

7.2.9. $\Lambda\rho^-$ (figure 7.9)

The effective mass plots of figure 6.3e show that about 50% of the events in the mass-regions selected (see table 7.1), are background events, not in fact due to $\rho^-$ production. The effect of these events is corrected for, using the assumption that the background is energy independent. Cross-sections for $K\bar{p}\rightarrow\Lambda\rho^-$ (a pure isospin 1 channel) have been given in a review by M.L. Stevenson [79], and are also shown in the figure.

The results of the present experiment show the cross-section rising from the threshold, levelling off, and then rising again. However, these results are generally higher than those of reference 79, and strongly disagree with the value at 2100 MeV. This is very probably because the contribution of the high-mass $Y^*\pi$ channels is increasing at higher energies, contrary to the assumption made above. Thus the cross-sections above 2150 MeV

from the present experiment are probably overestimated.

The cross-section from the reference 79 show a maximum at 2030 MeV, and strongly suggest the existence of a $\Lambda p$ decay mode of the $\Sigma(2030)$, although this was not remarked on by Stevenson.

7.2.10. $\Sigma^-\pi^+\pi^-$ (figure 7.10)

Cross-sections are plotted for this channel, and for the three main contributing quasi two-body channels separately, and added together. Results from the other $K^-n$ experiments are plotted [80,81,82]. The results of R. Armenteros et al. [80] are for an energy range just below the range of the present experiment, and these cross-sections agree with the present results. However, these results disagree with those of W.C. Delaney et al. [81]; but the latter cross-sections are only preliminary, and so are disregarded here.

The large peak in the cross-sections at 1765 MeV is caused by the $\Sigma(1765)$ resonance in the s channel.

$$K^-n \longrightarrow \Sigma(1765) \longrightarrow \Lambda(1520)\pi^- \longrightarrow (\Sigma^-\pi^+)\pi^- \qquad (7.2$$

It can be see from the curve (a) on figure 7.10, which is scaled from the curves in figures 7.13, that this process accounts for approximately the whole of the $\Sigma^-\pi^+\pi^-$ cross-section at this energy. However, this cannot be quite so, because of the $\Sigma(1385)\pi$ peak seen at the same energy (curve(c)); the discrepancy is approximately equal to the error on curve (a) at this energy.

The data from the present experiment show peaks at 1955 and 2060 MeV. The latter corresponds to the peaks in the $\Lambda(1520)\pi$ and $\Lambda(1405)\pi$ cross-sections (which will be discussed in sections 7.2.12 and 7.2.11 respectively). The peak at 1955 MeV, however, is at a slightly lower energy than the $\Lambda(1520)\pi$ peak at 1980 MeV. This could be caused by structure in the $\Sigma^-\rho^\circ$ or $\Sigma(1680)\pi$ cross-sections, both of which are considerable at these energies.

7.2.11. $\Sigma^+\pi^-\pi^-$ (figure 7.11)

Cross-sections are plotted for this channel, and for the three main contributing quasi-twobody channels separately, and

added together. Events with $\Sigma^+ \to p\pi^\circ$ and $\Sigma^+ \to n\pi^+$ decays were used together for these computations, since the events taken separately gave results in good agreement, in spite of the larger statistical fluctuations seen in the $\Sigma^+ \to p\pi^\circ$ results.

Cross-sections are available for two other $K^-n$ experiment in this energy region [80,83]. The results from R. Armenteros et al. [80] agree fairly well with those from the present experimen considering the large statistical errors on the present data at the region of overlap, which is about 1870 MeV.

The large peak in the cross-section at 1765 MeV is caused by the $\Sigma(1765)$ in the s channel, as in the $\Sigma^+\pi^-\pi^-$ channel;

$$K^-n \longrightarrow \Sigma(1765) \longrightarrow \Lambda(1520)\pi^- \longrightarrow (\Sigma^+\pi^-)\pi^- \qquad (7.3$$

It can be seen from curve (a) on figure 7.11, that this process accounts for about half of the $\Sigma^+\pi^-\pi^-$ cross-section at this energy.

The results of the present experiment show a peak at 1990 MeV, which corresponds to a peak in the $\Lambda(1520)\pi^-$ cross-section: but the $\Lambda(1520)\pi^-$ and $\Lambda(1405)\pi^-$ peaks at higher energies are not detectable in the $\Sigma^+\pi^-\pi^-$ cross-section values, because of the large errors in the latter.

The large differences between the cross-sections for $\Sigma^+\pi^-\pi^-$ and $\Sigma^-\pi^+\pi^-$ are not unexpected, because of the different isotopic spin decomposition of the $\Sigma\pi$ and $\pi\pi$ combinations in the two channels. The contributions of the $\Lambda\pi$ and $\Sigma\pi$ quasi two-body channels should be the same for both channels, if interference can be neglected. The rise in the $\Sigma^-\pi^+\pi^-$ cross-section with energy is mainly caused by the opening of the $\Sigma^-\rho^\circ$ channel, which does not contribute to the $\Sigma^+\pi^-\pi^-$ channel.

7.2.12 $\Lambda(1405)\pi^-$ (Figure 7.12).

Events from the $(\Sigma^+\pi^-)\pi^-$ and $(\Sigma^-\pi^+)\pi^-$ channels were used for these results; the cross-section was then multiplied by 1.5 to correct for the unfittable $(\Sigma^0\pi^0)\pi^-$ reaction and the total $(\Sigma\pi)^0\pi^-$ cross-section plotted.

Results from two other $K^-n$ experiments are shown. The reaction $(\bar{K}N)_1 \longrightarrow (\Sigma\pi)_0\pi$ has been studied by R. Armenteros et. al.[80] (the subscript represents isotopic spin). From the cross-section for this reaction is subtracted the cross-section for $(\bar{K}N)_1 \longrightarrow \Lambda(1520)\pi \longrightarrow (\Sigma\pi)\pi$, and a maximum value for the $(\Lambda(1405)\pi)_1$, cross-section is obtained. By this method the maximum branching ratio for the $\Sigma(1660) \longrightarrow \Lambda(1405)\pi$ decay is calculated to be 0.06, less than that obtained by production experiments[24]. The total amount of available data shown in figure 7.12 is sparse, but all values are compatible. (It should however be noticed that the results of reference 81 may be unreliable - see sections 7.2.10 and 7.2.13).

The results of this experiment suggest a peak at 2050 Me this is unlikely to be caused by $\Sigma(2030)$ in the s channel, since SU(3) forbids a (decuplet) $\longrightarrow$ (singlet) x (octet) decay, althoug a small decay would be allowed if the $\Lambda(1405)$ is mixed with the octet $\Lambda(1670)$.

7.2.13 $\Lambda(1520)\pi$ . (Figure 7.13).

The results for the present experiment were obtained frc $(K^-p)\pi^-$ and $(\Sigma^\pm\pi^\mp)\pi^-$ events, and have previously been given at the 1968 Vienna Conference,[70]. In figure 7.13 these results have been scaled to correct for the improved cross-section values in table 6.15 andto correct for $\Lambda(1520)$ decays to $\bar{K}^0n$ and all other modes. $\bar{K}^0n\pi^-$ events were omitted because they were thought to be misfitted for unseen and seen spectator protons; the seen spectator events are now known to be reliable (section 6.8).

The results of R. Armenteros et.al[84] are shown; this experiment studied; $K^- p \rightarrow \Lambda(1520)\pi^0 \rightarrow (\Sigma^{\pm}\pi^{\mp})\pi^0$ (7.3

This is a pure isospin 1 channel, and its cross-section must be multiplied by $3/_2$, for the $(\Sigma^0\pi^0)\pi^0$ channel, by 2, for relative $K\bar{p}/K\bar{n}$ Clebsch-Gordan coefficients, and by (1/0.45) for other $\Lambda(1520)$ decay modes[24]; i.e. by an overall factor of 6.67, to give the $K\bar{n}$ cross-section. The fitted curve of referenc 84 is plotted; this fit assumed that the reaction preceded entirel via the $\Sigma(1765)$ in the direct channel, and this gave excellent agreement with the cross-section values in the energy range from threshold (1660 MeV) to 1840 MeV. Using the same assumption, the world-average $\Sigma(1765)$ branching ratio to $\Lambda(1520)\pi$[24] has been used to calculate a cross-section at 1765 MeV; this agrees with the results of R. Armenteros et al..

Results from two $K\bar{n}$ experiments[81,82] are also shown; these studied $(\Sigma^-\pi^+)\pi^-$ and are multiplied by (3/0.45) to obtai the total $\Lambda(1520)\pi$ cross-section.

The agreement between the results of this experiment and those of R. Armenteros et al. is excellent. The results of W.C. Delaney et al.[81] disagree with the other results, and are disregarded.

The variation of cross-section shows, as well as the large peak at 1765 MeV, two smaller peaks at 1980 and 2070 MeV; the upturn in cross-section at 2150 MeV from the present experimen and the cross section at 2275 MeV from reference 82 suggest a further peak between 2190 and 2275.

Like the $\Lambda(1405)\pi$ decay, the $\Lambda(1520)\pi$ decay from $\Sigma(2030)$ is forbidden by SU(3), although mixing of the $\Lambda(1520)$ with the octet $\Lambda(1700)$[85] would allow a small decay. There is in fact no indication of a cross section peak at 2030 MeV.

## 7.3 Possible Σ resonances produced in the s channel.

### 7.3.1 Introduction

Table 7.2 summarises the peaks seen in the cross-sections shown in figures 7.2 to 7.13; peaks seen in the data of other experiments are shown in square brackets. The widths are the full widths at half height (corresponding to $\Gamma$), and can only be estimated. Any peaks with a width of less than 40 MeV or more than 120 MeV would be difficult to establish.

It is useful to compare the results from the present experiment with known Σ resonances that may be found in the s channel in this energy region, of 1850 - 2170 MeV.

### 7.3.2 Σ (1905)

Mass = 1905 ± 4 MeV. Width = 59 ± 9 MeV. $J^P = 5/2^+$ ($F_{5/2}$).

This resonance has previously been seen to decay to $\bar{K}N$ (10%) and $\Lambda\pi$ (50%), and is assigned to an SU(3) octet with the N (1688) and Λ(1815) [86]. Some disagreement exists over the degree of certainty of this resonance, but it has been seen strongly in the $\Lambda\pi$ decay mode [87]. The $\Sigma\pi$, $n K^*(890)$ and $\Sigma(1385)\pi$ peaks observed in the present results could be produced by decay of this resonance, and would correspond to branching ratios of 8%, 23% and 6% respectively. A $\bar{p}$ - p production experiment [88] has seen a $\Sigma(1942 \pm 9)$, width $36^{+20}_{-36}$ MeV, decaying to $N\bar{K}\pi$ which could correspond to the $n K^*(890)$ peak seen here. However all these peaks occur at an energy about 40 MeV higher than the accepted mass for the Σ(1905). Possibly another resonance of mass about 1940 MeV produces these peaks. This has also been suggested by a partial wave analysis of the $\Sigma(1385)\pi$ channel, carried out at Imperial College [89], which strongly indicates the existence of a $P_{3/2}$ $\Sigma(1950 \pm 10)$ resonance, width about

TABLE 7.2 Peaks observed in cross-section plots.

| Channel | Mass (MeV). | Width (MeV) | Cross-section. (mb). mb | Comments. |
|---|---|---|---|---|
| $\Sigma\pi$ (total) | [1670 ± 15 | 110 | 2.5 ± .5] | |
| | [1800 ± 15 | 90 | 0.7 ± .3] | |
| | 1960 ± 20 | 30 | 0.3 ± .15 | |
| | 2020 ± 30 | 80 | 0.3 ± .15 | |
| $N\,K^*(890)^-$ $\hookrightarrow \bar{K}^0\pi^-$ | 1940 ± 15 | 60 | 0.6 ± .3 | ×1.5 for total $NK^*$. |
| $N^*(1236)\,\bar{K}^0$ $\hookrightarrow n\pi^-$ | (2090 ± 30 | 50 | 0.2 ± .2) | ×1.33 for total $N^*K$. |
| $\Sigma(1385)^0\bar{\pi}^0$ $\hookrightarrow \Lambda\pi^0$ | [1690 ± 10 | 25 | 0.9 ± .3] | ×1.11 for total $\Sigma(1385)\pi$. |
| | [1765 | 120 | 6.0 ± .5] | |
| | (1950 ± 20 | 50 | 0.2 ± .2) | |
| | 2030 ± 10 | 60 | 0.4 ± .2 | |
| $\Lambda\rho^-$ (total) | [2020 ± 30 | 100 | 0.9 ± 15] | |
| $\Lambda(1405)\pi$ (total) | (2050 ± 25 | 50 | 0.15 ± 15) | |
| $\Lambda(1520)\pi$ (total) | [ 1765 | 120 | 5.5. ± .3] | |
| | 1980 ± 15 | 40 | 0.6 ± .2 | |
| | 2060 ± 20 | 60 | 0.5 ± .2 | |

[ ] indicates peaks seen by other experiments.

( ) indicates peaks only weakly seen in the present experiment.

100 ± 30 MeV, which appears to have a larger amplitude in this channel than does the $F_{5/2}$ $\Sigma(1905)$ resonance. Evidence for this resonance has also been seen by a Rutherford Laboratory - Saclay $K^-p$ formation experiment [87].

Therefore the results of this experiment confirm that there is a resonance with a mass between 1900 and 1950 MeV, although it maybe the $F_{5/2}$ $\Sigma(1905)$, a $P_{3/2}$ $\Sigma(1940)$ or both these resonances.

7.3.3. $\Sigma(2030)$.

Mass = 2027 ± 4 MeV. Width 131 ± 10 MeV. $J^p = 7/2$ $(F_{7/2})$.

This a well established resonance, seen to decay to $N\bar{K}$, $\Lambda\pi$ and $\Sigma\pi$, with a total identified branching ratio of 55%. It is assigned to an SU(3) decuplet, together with the $\Delta(1920)$ [86].

The $\Sigma\pi$ peak at 1920 MeV, in figure 6.4 corresponds to a branching ratio of 7.5 ± 4.0%, compatible with the previous best value of 10% [24]. Peaks in the $N^*(1236)\bar{K}$, $\Sigma(1385)\pi$, $\Lambda\rho$ $\Lambda(1405)\pi$ and $\Lambda(1520)\pi$ cross-sections could also be produced by decay of this resonance. However the last two decay modes involve SU(3) singlets and octets, which cannot be produced from the decay of an SU(3) decuplet, although $\Lambda$ singlet - octet mixing could allow a small decay.

The remaining $N^*(1236)\bar{K}$, $\Sigma(1385)\pi$ and $\Lambda\rho$ peaks correspond to $\Sigma(2030)$ branching ratios of 7 ± 7%, 11 ± 6%, and 23 ± 4% respectively. These branching ratios, if correct, would account for nearly all of the unknown 45% of the $\Sigma(2030)$ decay. However, calculations of SU(3) factors and phase space, similar to those of Tripp et. al. [86] indicate that the $\Sigma\eta^o$, $K^*(890)n$ $K^*(890)n$, and $\Lambda(1670)\pi$ decays should be about strong as the $\Lambda\rho$ decay. Of these channels, only $K^*(890)n$ is investigated here, and the upper limit for $\Sigma(2030)$ decay is 0.3 mb, equivalent to an 11% branching ratio; this is less than the $\Lambda\rho$ branching ratio given

above, i.e. lower than expected.

The existence of a $\Sigma(1385)\pi$ decay mode of the $\Sigma(2030)$ is strongly confirmed by a partial wave analysis carried out at Imperial College [89], which gives a branching ratio of $23 \pm 3\%$, rather higher than that deduced from the cross-section data alone

The peak in the $\Lambda\rho$ cross-section is particularly clear, and is interesting since only a few other (Baryon)→(Baryon + Vector Meson) decays havebeen reported.

7.3.4. Other possible resonances.

The $\Lambda(1520)\pi$ peak at 1980 MeV is at too high an energy to be associated with the $\Sigma(1905)$, but could associated with the $P_{3/2}\Sigma(1950)$ that is suggested in the previous section, which would then have to belong to an SU(3) octet.

The other $\Lambda(1405)\pi$ and $\Lambda(1520)\pi$ peaks at about 2050 MeV are unlikely to come from $\Sigma(2030)$ decay, for reasons discuss above, and therefore suggest the existence of a $\Sigma(2050)$, width about 60 MeV, belonging to an SU(3) octet. The evidence for this is fairly good; the $\Lambda(1520)\pi$ peak is a $2\frac{1}{2}$ standard deviation effect.

## 7.4 Conclusions

The cross-section results presented in this chapter indicate the existence of several previously unreported decays of known $\Sigma$ resonances of masses between 1900 and 2100 MeV, to quasi two-body final states. There is also good evidence for the existence of two new $\Sigma$ resonances, of masses 1950 and 2050 MeV.

The significance of the peaks observed is generally reasonable, and the correlation between peaks in different states is encouraging. However, the identification of these peaks with $\Sigma$ resonances in the s channel cannot be completely justified until the final state angular distributions have been studied, for example, by partial wave analyses. This collaboration is carrying out partial wave analyses for the $\Sigma(1385)\pi$ and $\Lambda(1520)\pi$ channels, and interesting results can be expected.

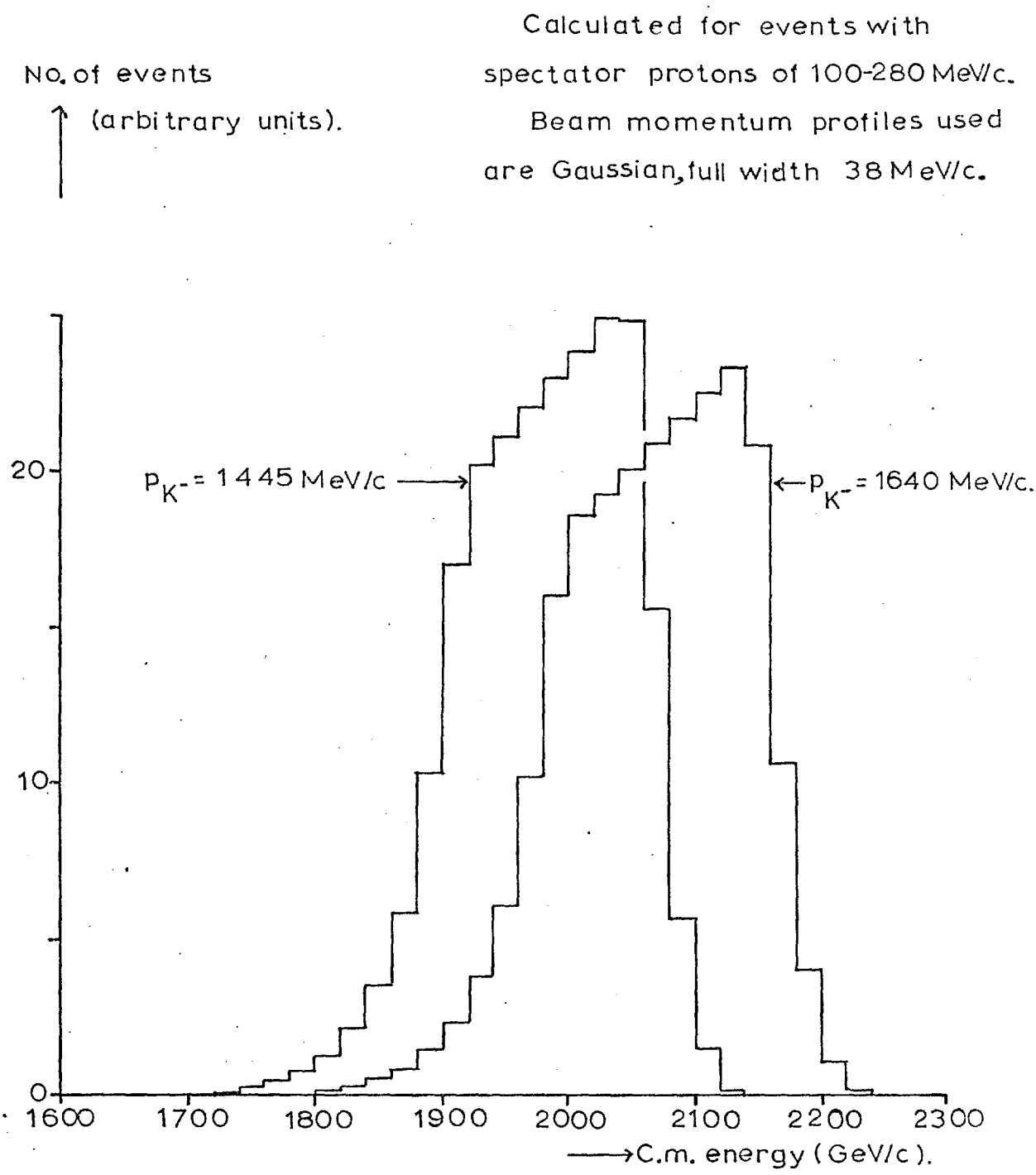


FIGURE 7.1 EXPECTED DISTRIBUTION OF C.M. ENERGY, ON THE ASSUMPTION OF CONSTANT CROSS-SECTION.

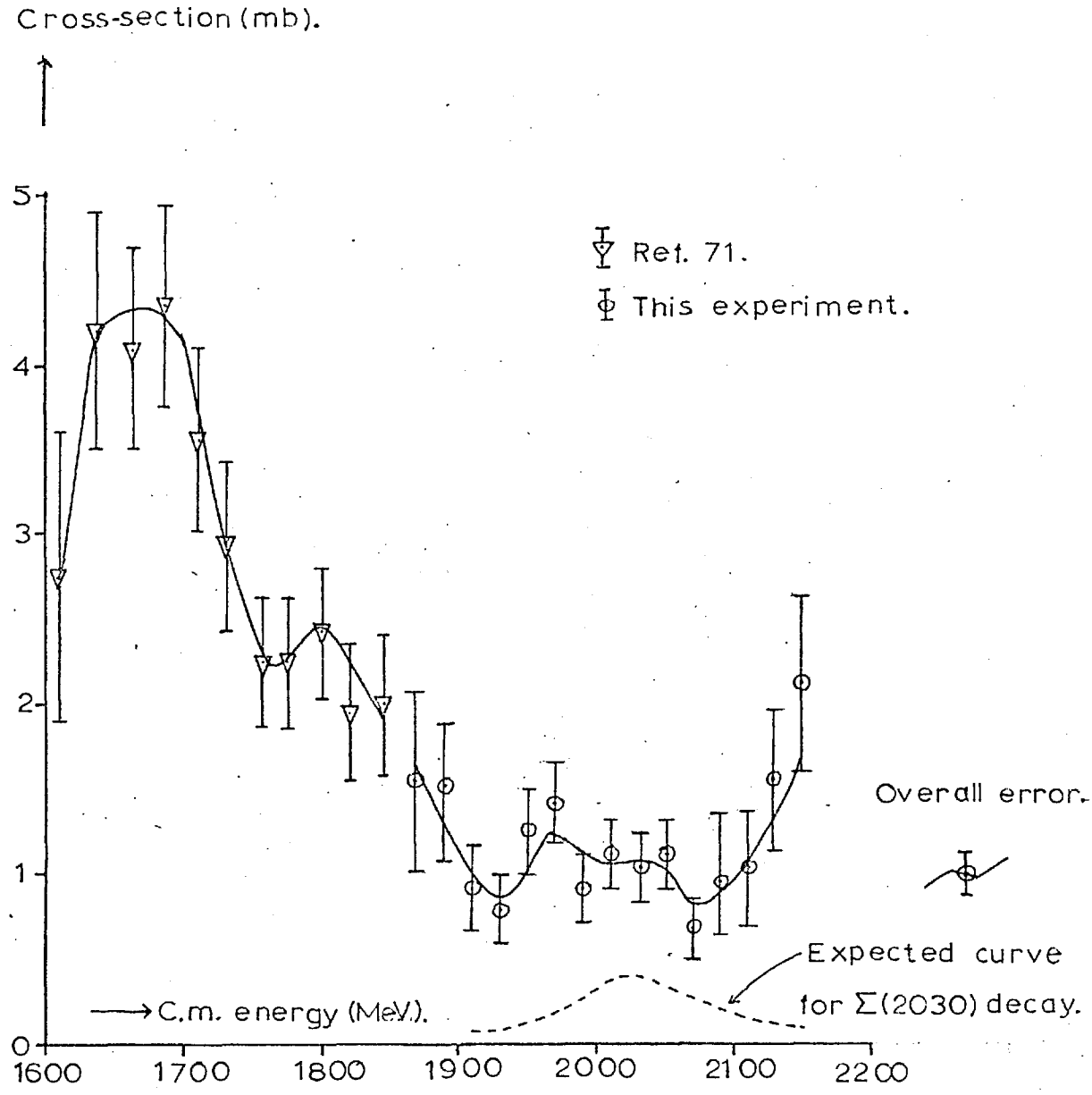


FIGURE 7.2 CROSS-SECTION FOR $K^-n \rightarrow \Sigma^0\pi^-$ PLUS $K^-n \rightarrow \Sigma^-\pi^0$.

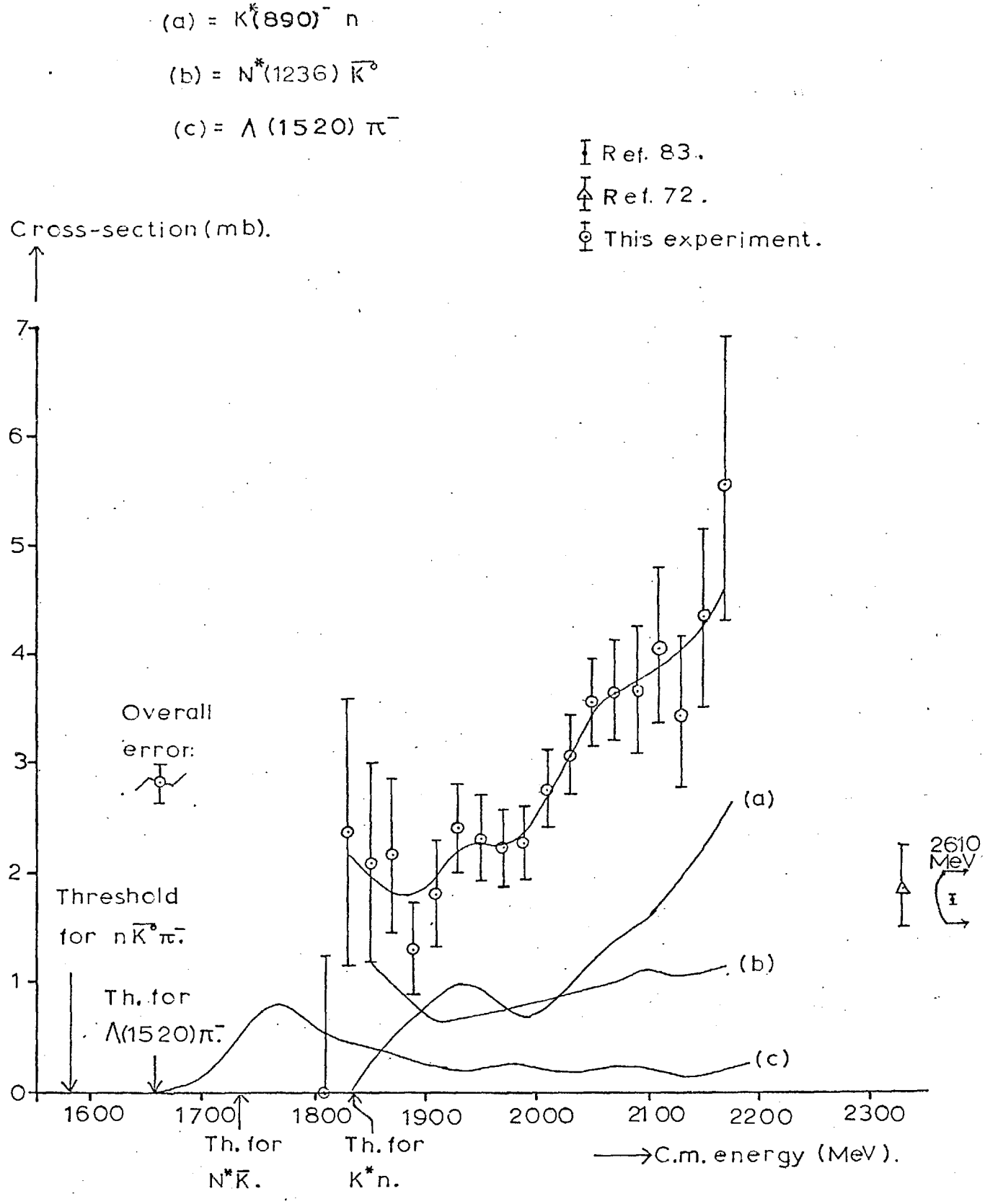


FIGURE 7.3 $K^- n \rightarrow n \bar{K}^0 \pi^-$.

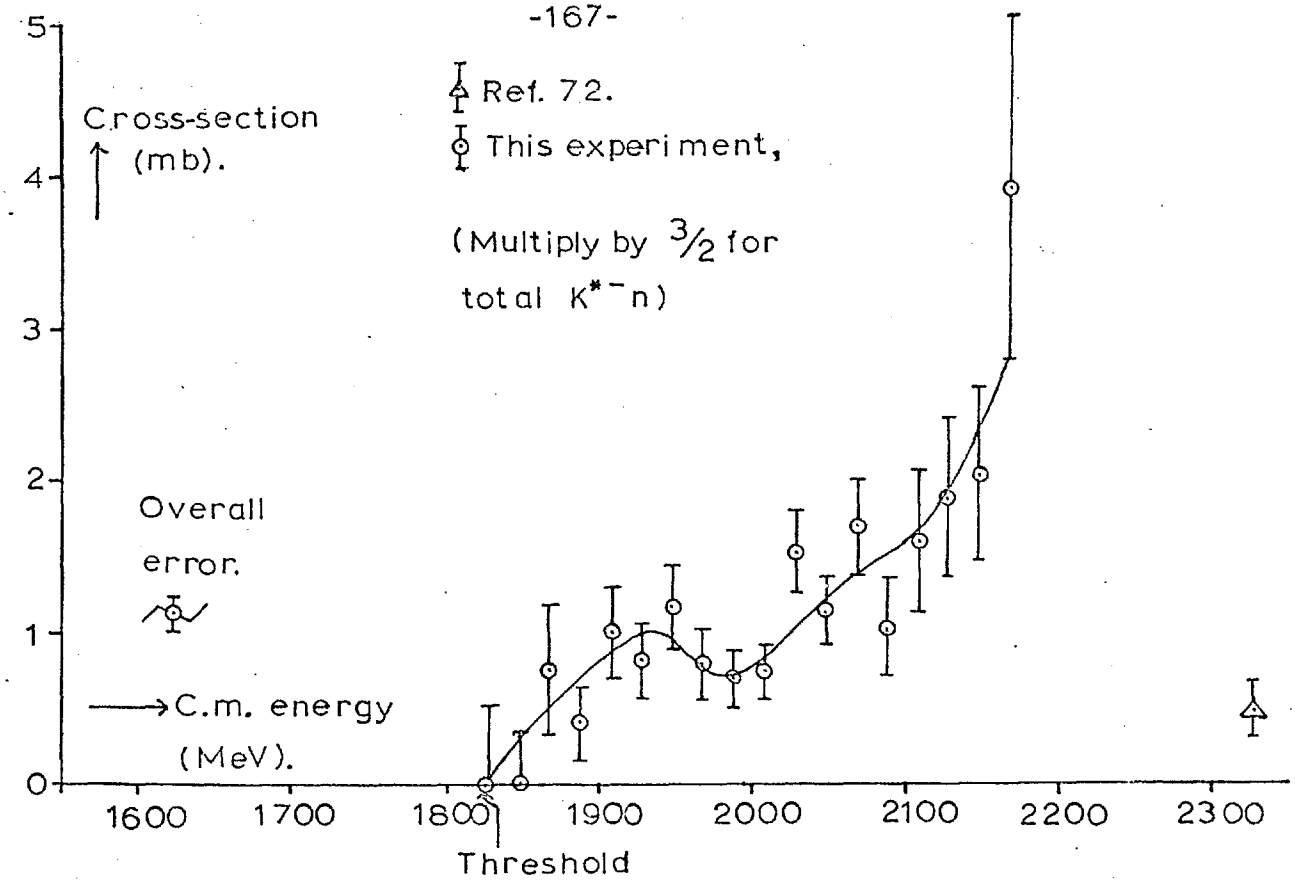


FIGURE 7.4 $K^-n \rightarrow K^{*}(890)^- n \rightarrow (K^0\pi^-)n$.

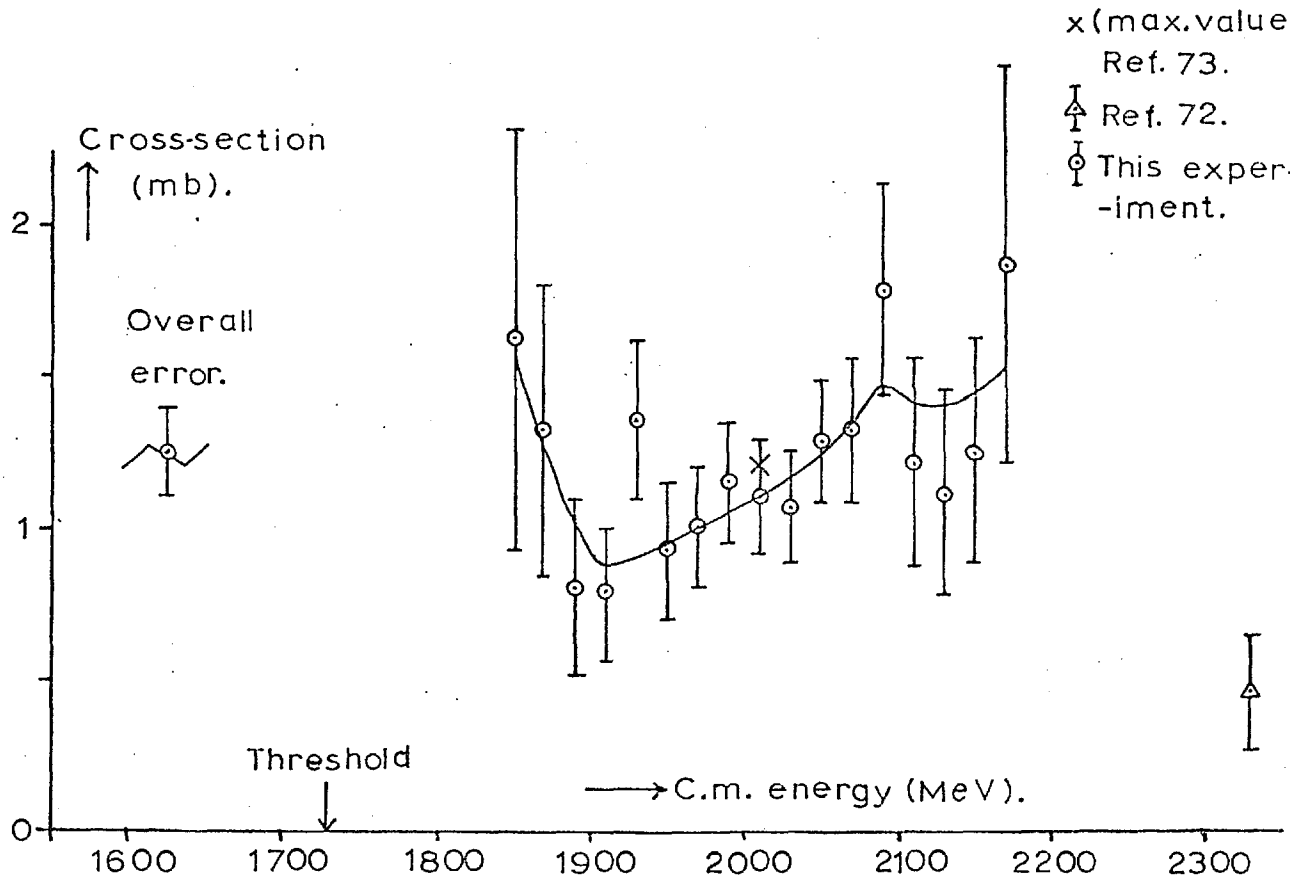


FIGURE 7.5 $K^-n \rightarrow N^{*}(1236)^0 \bar{K}^0$.

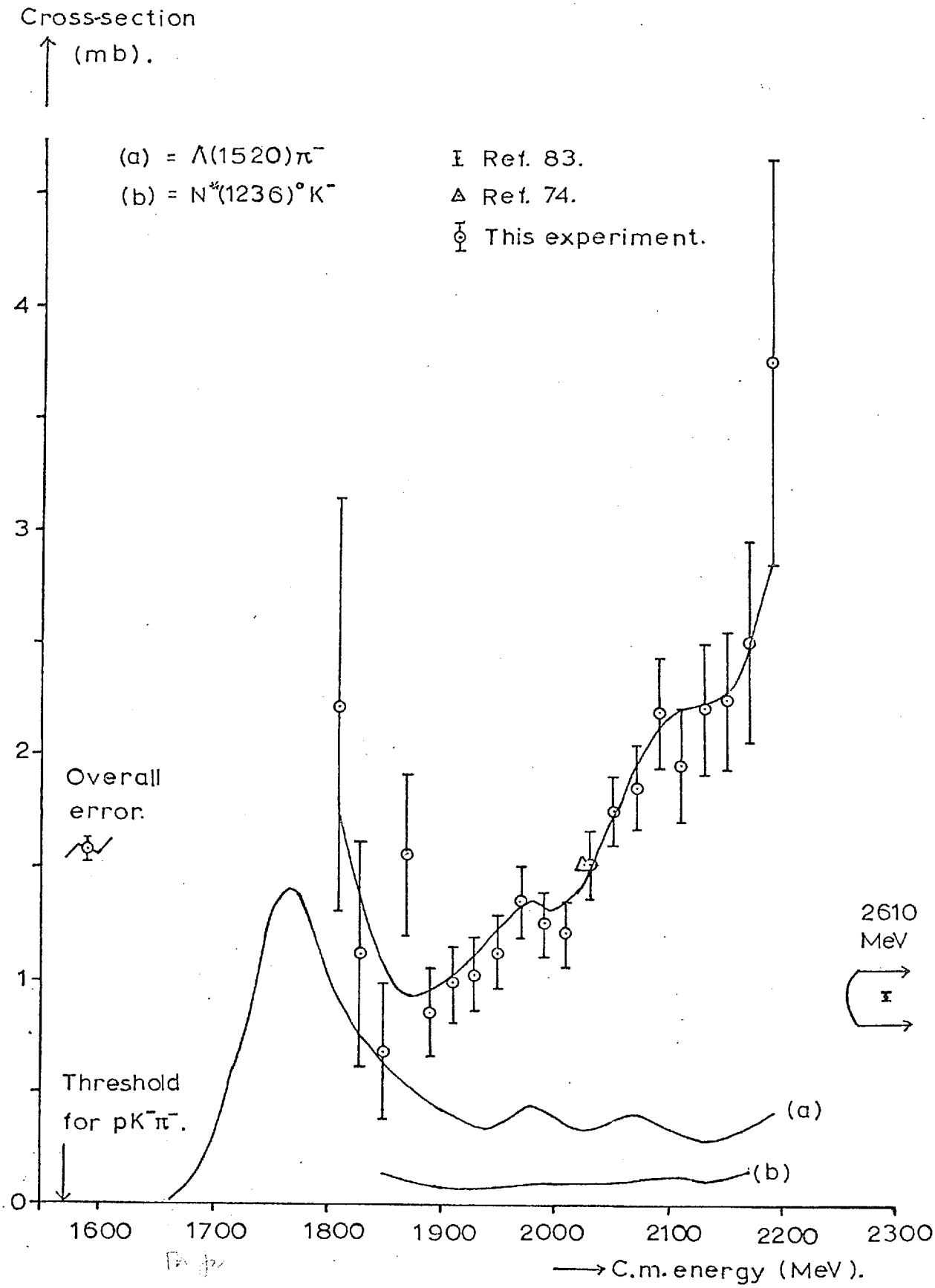


FIGURE 7.6 $K^-n \rightarrow pK^-\pi^-$.

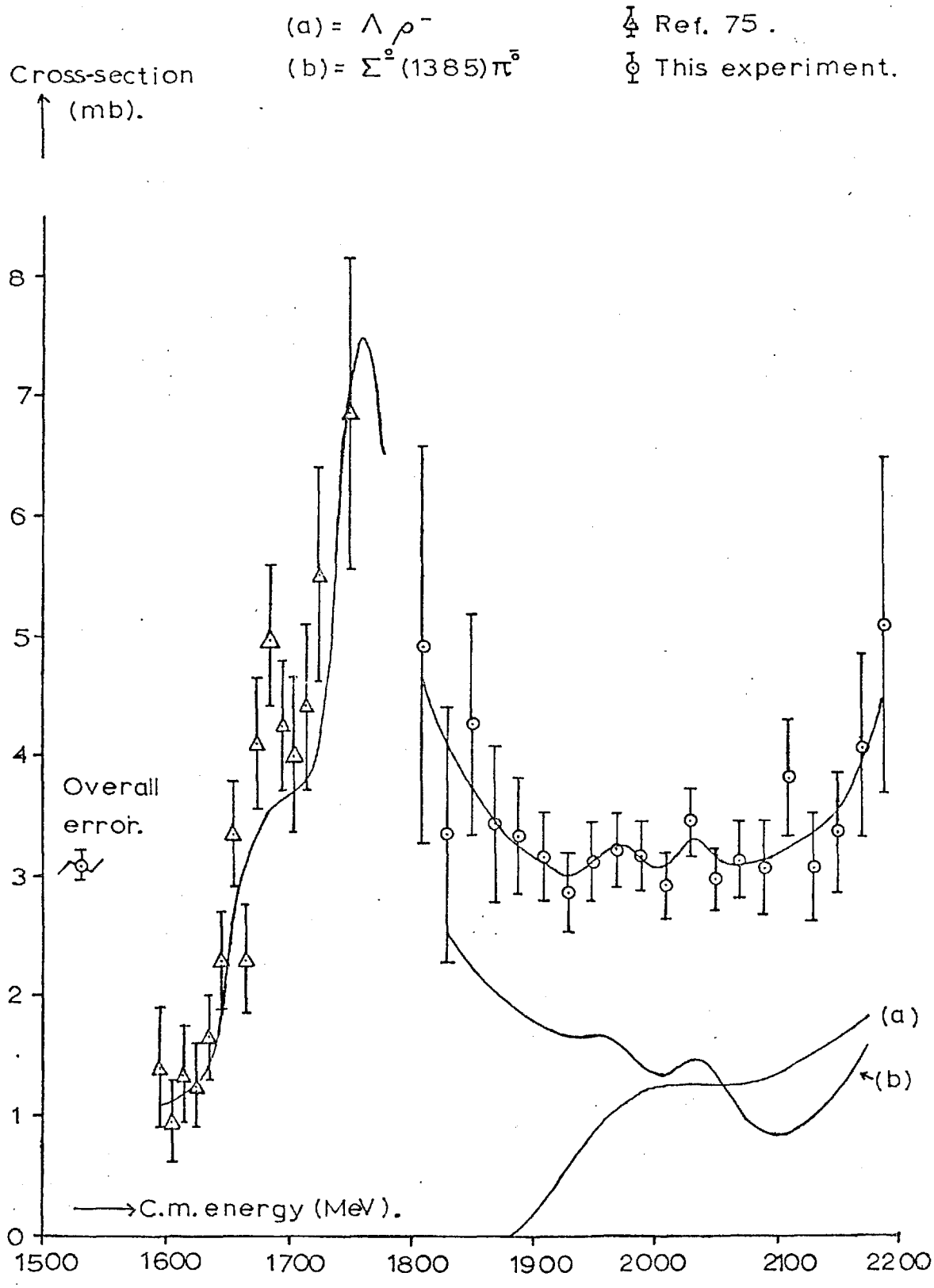


FIGURE 7.7 $K^- n \rightarrow \Lambda \pi^\circ \pi^-$.

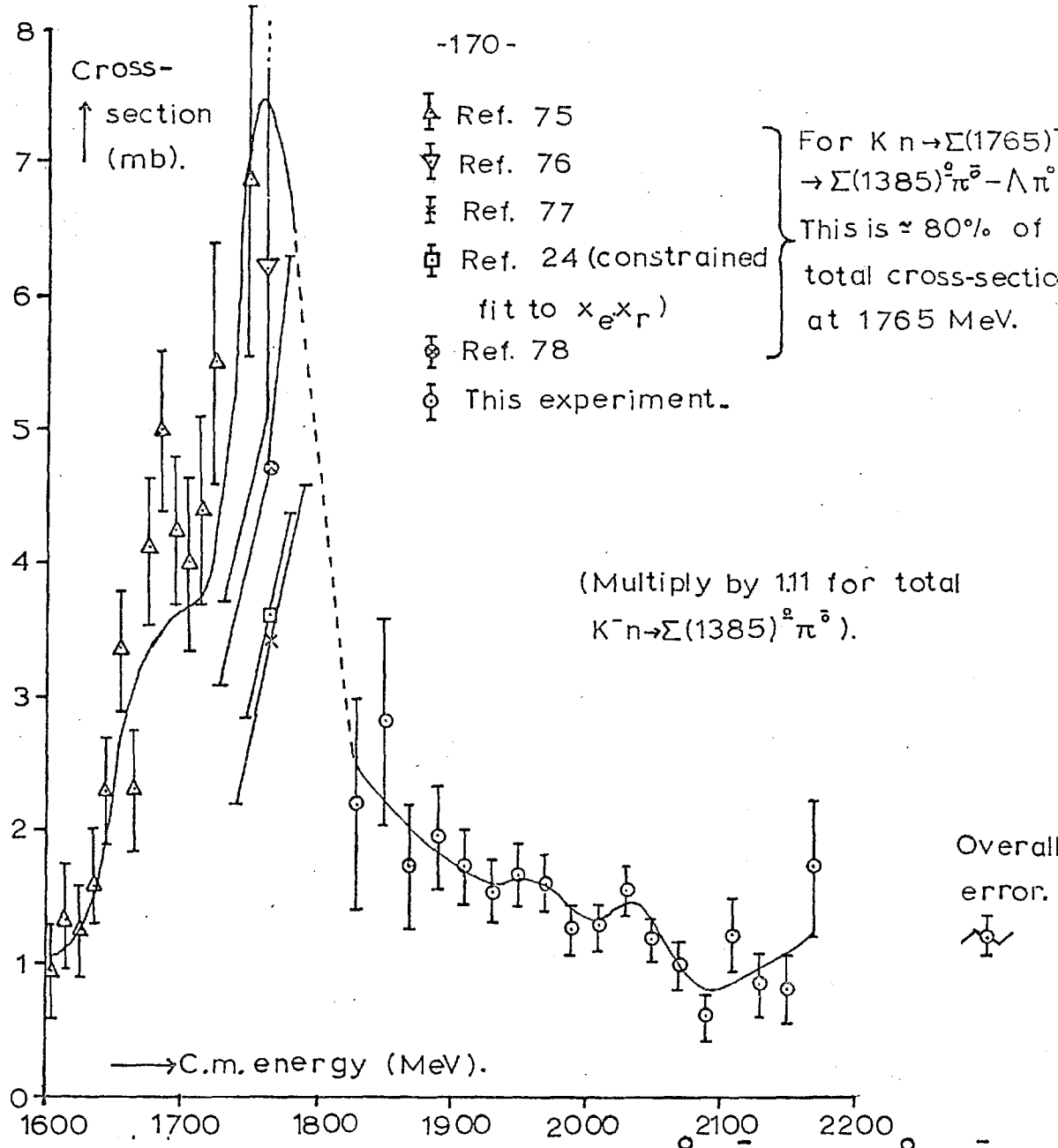


FIGURE 7.8 $K^- n \to \Sigma(1385)^0 \pi^- \to (\Lambda \pi^0) \pi^-$.

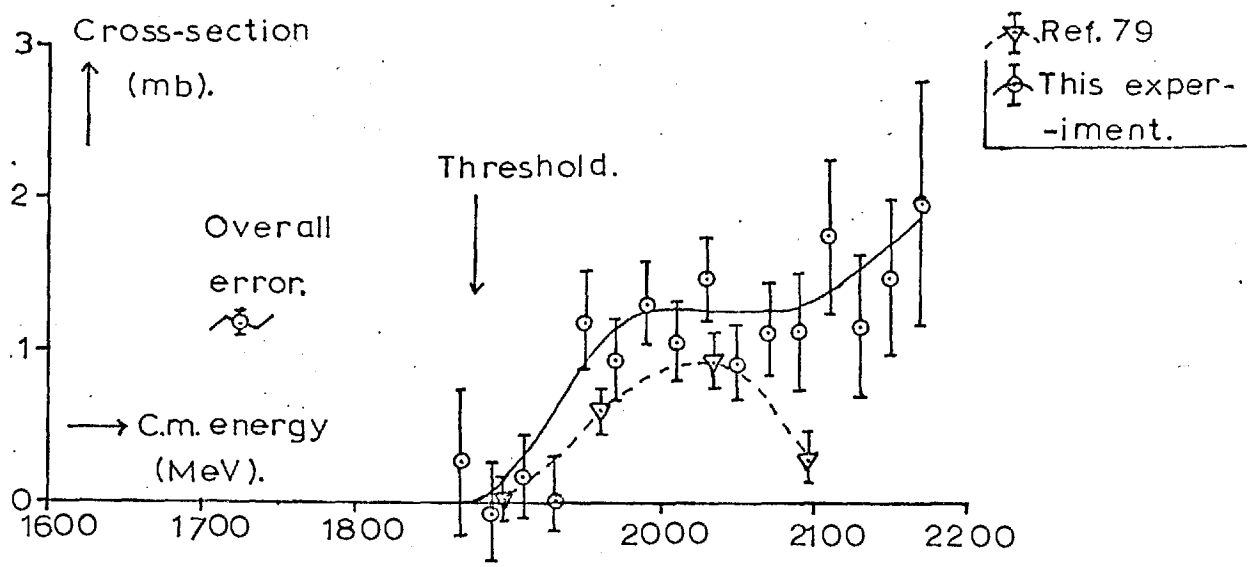


FIGURE 7.9 $K^- n \to \Lambda \rho^- \to \Lambda(\pi^0 \pi^-)$. (=total $\Lambda \rho^-$)

For figures 7.10 and 7.11 :

(a) = $\Lambda(1520)\pi^-$.

(b) = $\Lambda(1405)\pi^-$.

(c) = $\Sigma^0(1385)\pi^-$.

(t) = Sum of (a)+(b)+(c).

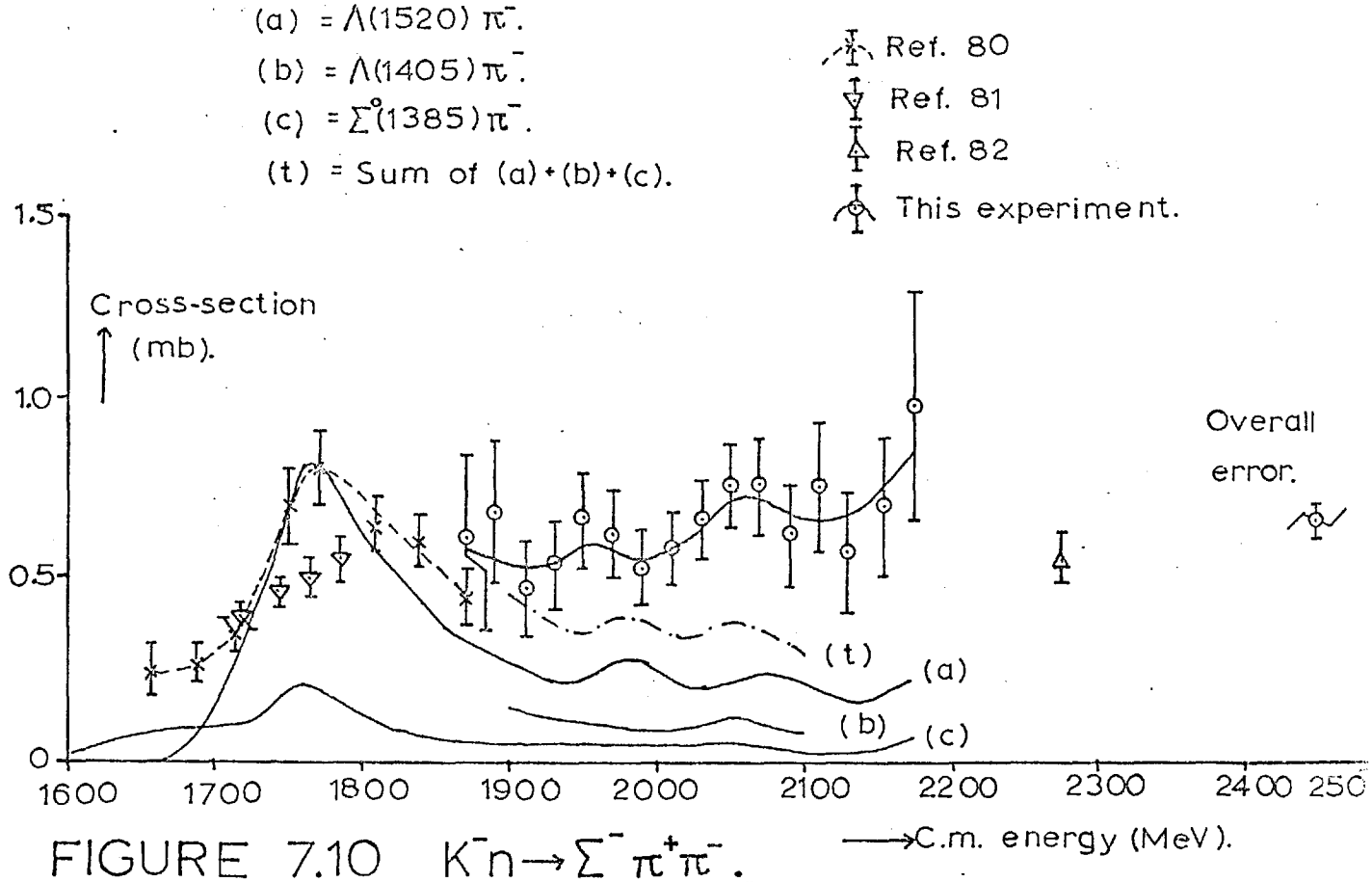


FIGURE 7.10 $K^-n \rightarrow \Sigma^-\pi^+\pi^-$.

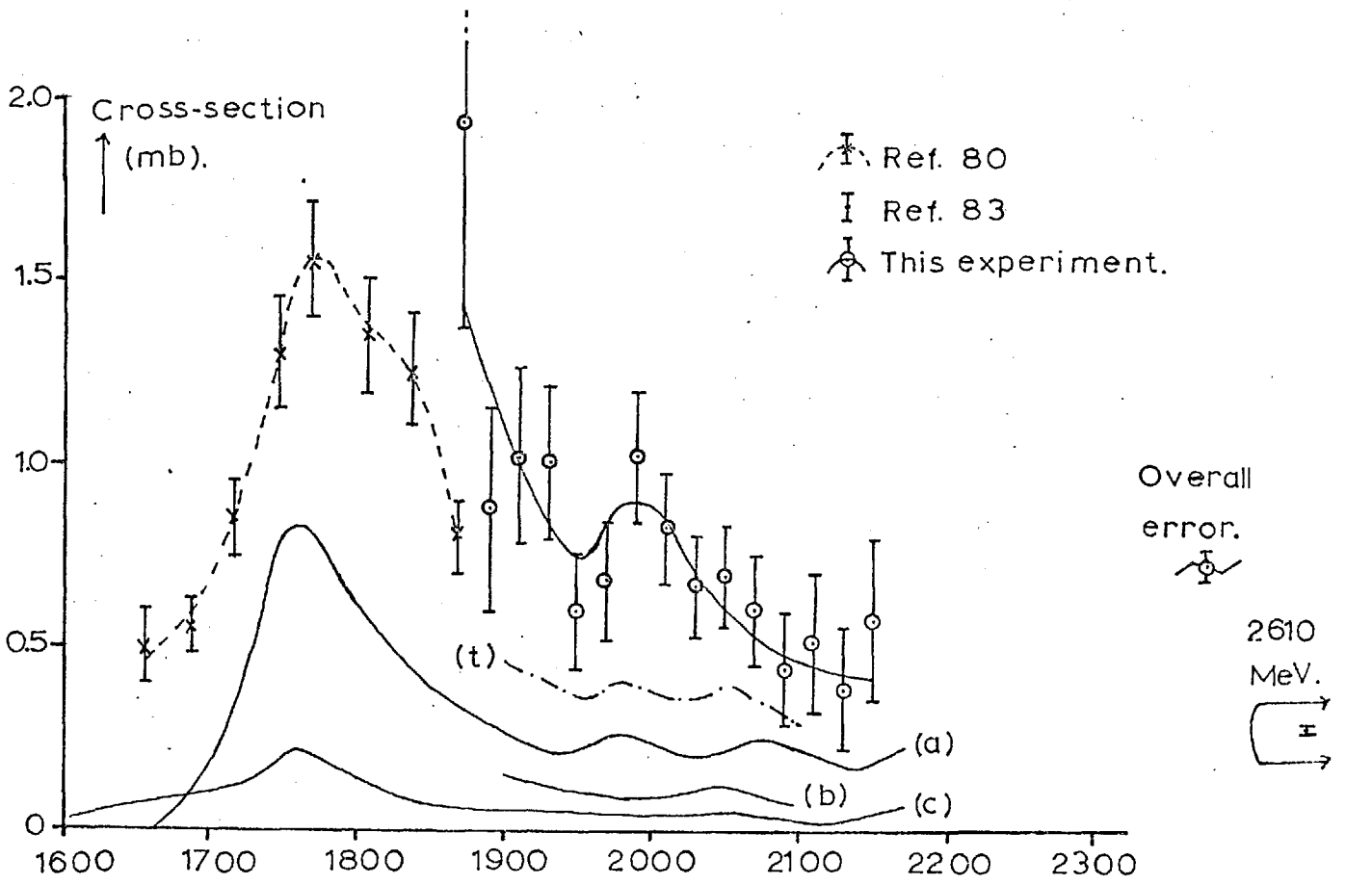


FIGURE 7.11 $K^-n \rightarrow \Sigma^+\pi^-\pi^-$.

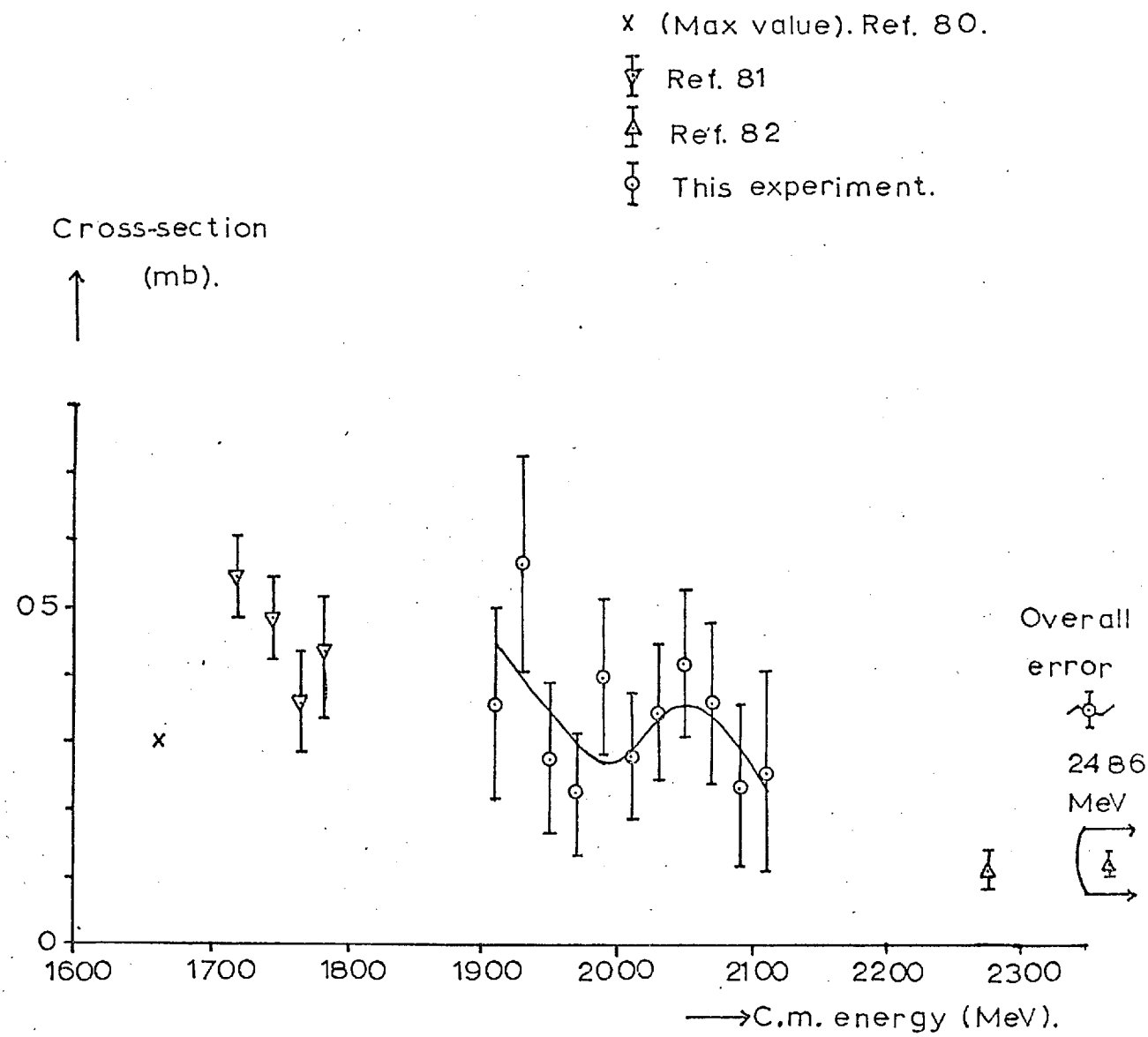


FIGURE 7.12 $K^- n \rightarrow \Lambda(1405)\pi^- \rightarrow (\Sigma\pi)^0\pi^-$.

(= total $\Lambda(1405)\pi^-$)

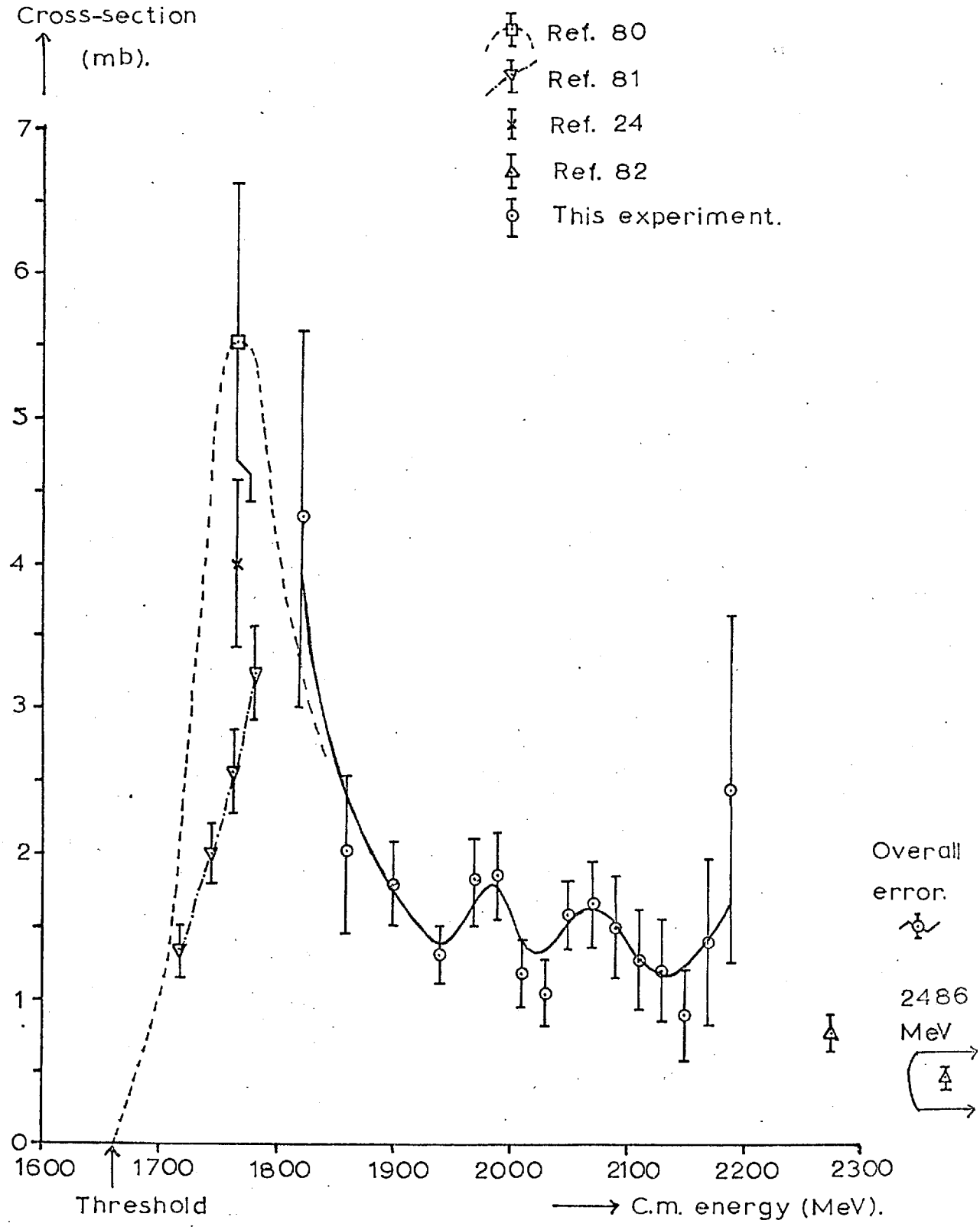


FIGURE 7.13 $K^-n \rightarrow \Lambda(1520)\pi^-$ (ALL $\Lambda(1520)$ DECAY MODES).

References

("K⁻d notes" are internal work notes circulated by the Imperial College K⁻d group. They are referred to when they provide further details of results or discussions relevant to subjects discussed here.

NIRL, RPP and RHEL all specify Rutherford Laboratory reports or preprints.)


1. P.J. Lychfield. PhD thesis, University of Oxford, 1967.
2. D.A. Gray et al. "Targetting techniques at Nimrod". RPP/N4 (1965).
3. J.W. Gardner and D. Whiteside, "Tramp". NIRL/M/21 (1961).
4. Florent et al.. L'Onde Electrique 41, p 1001 (1961).
5. W. Welford. Applied Optics 2, p 981 (1963).
6. E.C. Sedman. "The Jokin System". RHEL/R/111.
7. The Bind program. Written by S.L. Baker (Imperial College). No full description issued (1965).
8. J.W. Burren and J. Sparrow. "The geometrical reconstruction of bubble chamber tracks." NIRL/R/14.
9. J.W. Burren et. al. "The bubble chamber analysis program system, Mark II". Rutherford Laboratory, unpublished. (1965).
10. J.W. Burren and E.C. Sedman. "Modifications to the Geometry program". RHEL/R/150 (1967).
11. D.H. Stork et al.. "Mongoose, a program for determining optical constants" University of Oxford, unpublished, 1965.
12. G.F. Cox (Birmingham University), private communication (1966).
13. D. Pearce. "Rutherford Lab. magnetic field methods." K⁻d note 16. (1966).
14. CERN T.C. program library. Thresh section.
15. CERN T.C. program library. Grind section.
16. CERN T.C. program library. Slice section.

17. A.G. Wilson, "Kinematic fitting program." NIRL/M/38 (1962).

18. A.G. Wilson, "Hypothesis assigning in the testing of bubble chamber events." NIRL/R/42 (1963).

19. M.L. Garetti. "Reprocess of tau decays." K⁻d note 36 (1967).

20. For example, Fickinger et al.. Bull. Am. Phys. Soc. , p587 (1965).

21. S. Ali and D.B. Miller."Kinks" (= charged decays). K⁻d note 39 (1967).

22. D. Pearce and A. Safder. "300 and 400 fitting." K⁻d notes 41 and 45 (1967).

23. S. Ali and D.B. Miller. "$V^0$ fitting". K⁻d notes 35 and 53 (1967).

24. The Particle Data Group. Rev. Mod. Phys. 41, p 109 (1969).

25. C. H. Wilkinson (Oxford University) "Inco". Unpublished (1964).

26. S. Ali. "Slice for Inco D.S.T.". K⁻d note 84 (1968).

27. J.M. Scarr (Rutherford Laboratory). "The Statistics program." Unpublished (1965).

28. M. Haque et alia. "The reaction $K^-p \rightarrow$ Hyperon + meson at 3.5 GeV/c. Phys. Rev. 152, p 1148 (1966).

29. D. Pearce. "$\Sigma^{\pm}$ weighting methods". K⁻d note 97a (1968).

30. CERN T.C. program library.( J. Zoll). Sumx.

31. G.F. Chew. Phys.Rev. 80, p 196 (1950).

32. G.F. Chew and G.C. Wick. Phys.Rev.85, p 636 (1952).

33. J. Ashkin and G.C. Wick. Phys.Rev.85, p 686 (1952).

34. G.F. Chew and M.L. Goldberger. Phys. Rev. 87, p 778 (1952).

35. Hulthén and Sugawara. Handbuch der Physik 39, p 1 (1957).

36. M.J. Moravcsik. Nuclear Physics 7, p 113 (1958).

37. W. Lee. PhD thesis, University of California, UCRL 9691(1961).

38. I. Butterworth et alia. "$K^+n$ charge exchange at 2.3 GeV/c". Phys.Rev. Letters 15, p 734 (1965).

39. A. Forino et alia. "Two pion production in $\pi^+d$ at 4.5 GeV/c". Phys. Letters 19, p 68 (1965).

40. J.I. Rhode et alia. " $K^-d \rightarrow K\pi^+\pi^-p$ at 2.24 GeV/C". Phys. Rev. 178, p 2039 (1969).

41. D. Pearce. "A survey of spectator problems". $K^-d$ note 62 (1967).

42. F. Bigata. PhD thesis, Paris Orsay, 1968.

43. W. M. Smart. Phys. Rev. 169, p 1330 (1968).

44. A Berthon et al.. Paper submitted to the Lund International Conference on Elementary particles, 1969.

45. C.G. Wohl et alia. Phys. Rev. Letters 17, p 107 (1966).

46. Figure 4.6 shows results from Birmingham University (private communication 1969). Results obtained at Imperial College, using a different program (reference 48 and 70 )were very similar.

47. D. Pearce. " $\Lambda/\Sigma^0/\Lambda\pi^0$ ambiguities." $K^-d$ note 86. (1968).

48. F. Fuchs. PhD thesis, University of London, 1970.

49. D. Pearce. "Effect of inserted spectator on effective mass plots." $K^-d$ notes 76 (1968), and 119 (1969).

50. W. Hoogland. PhD thesis, Amsterdam, 1968.

51. J.R. Campbell et alia. "The kinematic fitting of neutron target reactions in a deuterium bubble chamber." Submitted to Nuclear Instr. and Methods (1969).

52. This value was obtained by A. Seagar (Rutherford Laboratory).

53. R.J. Glauber. Phys. Rev. 100, p 242 (1955).

54. Baker et alia. Proceedings of the Sienna International Conference on Elementary particles (1963) Vol.1, p 634.

55. W. Galbraith et alia. Phys. Rev. 138, p B913 (1965).

56. A.A. Carter et alia. Phys. Rev. 168 , p 1457 (1968).

57. G. Fäldt and T.E.O. Ericson, Nuclear Physics. B8, p 1 (1968).

58. D.V. Bugg et alia. Phys Rev. 168, p 1466 (1968).

59. See, for example, G. Källen, "Elementary Particle Physics," chapter 4, (Addison-Wesley, 1964), and M.L. Stevenson,"Review of recent work on $K^-$ meson interactions." UCRL11493, and proceedings of Conference on Particle Physics, University of Colorado,Boulder, 1964.

60. J.R. Fry (Birmingham University), private communications (1968).

61. Private Communications from Birmingham University Group (12th December, 1968).

62. Birmingham - Edinburgh - Glasgow - London (Imperial College) collaboration, (i.e. the B.E.G.L. collaboration). "Y* production in $K^-$ - neutron interactions at 1.45 and 1.65 GeV/c."
Read at XIVth International Conference on High Energy Physics, Vienna, 1968.

63. Private Communication from Edinburgh University (12th June 1968).

64, Private communication from Glasgow University group (March 1968).

64a. F. Heathcote. PhD thesis, University of Birmingham, 1969.

65. D. Pearce. " $\bar{K}^0 n\pi^-p$ problem." $K^-d$ note 119 (1969).

66. F. Fuchs. "E* Distributions." $K^-d$ note 80 (1968).

67. G.F. Cox et. al. (B.E.G.L. collaboration). Submitted to Nuclear Physics (1969).

68. S.S. Ali. PhD thesis, University of London, 1969.

69. A. Safder, MSc thesis, University of London 1968.

70. B.E.G.L. collaboration. "A study of $K^-n$ interactions from 1800 - 2200 MeV."
Read at XIVth Internationl Conference on High Energy Physics, Vienna 1968.

71. R. Armenteros et. al.. CERN PHYS 69.2 (1969).

72. K.F. Galloway et. al.. Phys. Rev. 158 , p 1360 (1967).

73. Cooper et. al. Proceedings of Conference on Particle Physics, CERN (1962), p 298.

74. A. Barbaro - Galtieri et. al. Phys. Letters 6, p 296 (1963).

75. J.H. Bartley et. al. Phys. Rev. Letters 21, p 1111 (1968).

76. W.H. Sims et. al. Phys. Rev. Letters 21, p 1413 (1968).

77. R.P. Uhlig et. al.. Phys. Rev. 155, p 1448 (1967).

78. R. Armenteros et. al. Zeit. Phys. 202, p 486 (1967).

79. M.L. Stevenson. See reference 59.

80. R. Armenteros et al.. Nuclear Physics B8, p 216 (1968).

81. W.C. Delaney et al.. BNL 13562. Submitted to NUOVO CIMENTO (April 1969).

82. A. Barbaro - Galtieri et al.. Phys. Rev. Letters 21, p 573 (1968).

83. S.A.B.R.E. collaboration. " $Y_0^*(1520)$ production and decay". Submitted to Nuclear Physics (1968).

84. R. Armenteros et al.. Phys. Letters 19, p 338 (1965).

85. G.B. Yodh. Phys. Rev. Letters 18, p 810 (1967).

86. R.D. Tripp et al.. Nuclear Physics B3, p 10 (1967).

87. I. Butterworth (Rutherford Laboratory) private communication (1970).

88. R.K. Böck et al . Phys. Letters 17, p 166 (1965).

89. D. Pearce. "A partial wave analysis of $\Sigma(1385)\pi$ ". $\bar{K}$d note 126 (1969).

ACKNOWLEDGEMENTS

I would like to thank Professor C.C. Butler for his hospitality during my stay at Imperial College, and Mr N.C. Barford for his kind supervision during this time. I am also greatly indebted to Dr. I. Butterworth and Dr. D.B. Miller for much guidance and help given throughout the course of this work. Especial thanks are due to my colleagues Dr. S. Ali, Mr. M.J. Counihan, Dr. D. Goyal, Mr. F. Fuchs and Dr. B. Schwarzchild, at Imperial College, and also all colleagues in collaborating groups.

Many people contributed to the analysis of this experiment. The Bubble Chamber was operated by a team from Saclay. The book-keeping and processing was very capably organised by Miss J. Urquhart. Mrs. K.M. Greaves efficiently organised the measuring, much of which was carried out by Mrs. I. Lowe and Mrs. E. Moynihan, who also supported the author with tea during important stages of the work. This thesis has been typed by Miss. S. Hardcastle, whose patience and skill has been very welcome. To all these people I owe considerable thanks.

Lastly I must thank the Science Research Council and Imperial College for their financial support during this time.